Effect of Manganese (Mn) Content and Homogenization Treatment on Hot Deformation of AA3xxx Aluminum Alloys

by

Reza Mir Miri

A thesis
presented to the University of Waterloo
in fulfillment of the
thesis requirement for the degree of
Master of Applied Science

in

Mechanical Engineering

Waterloo, Ontario, Canada, 2016

AUTHOR'S DECLARATION

I hereby declare that I am the sole author of this thesis. This is a true copy of the thesis, including any required final revisions, as accepted by my examiners.

I understand that my thesis may be made electronically available to the public.

Abstract

In the current study the effect of Mn content and homogenization heat treatment on the hot deformation behavior of AA3XXX aluminum alloy was investigated. Three Mn contents of 0.05, 0.29 and 1.04 wt.% were considered. These alloys were subjected to a single-step heat treatment (H1), two two-steps heat treatments (H2 and H3) cycles. Electrical conductivity measurements were applied on as-cast alloys and after three homogenization treatments in order to evaluate the Mn content in the solid solution on the AA3XXX aluminum alloys.

Hot deformation of the alloys was conducted using Gleeble 3500 machine, under plane strain conditions up to a final strain of 0.5. The deformation strain rate was selected as 0.1, 1.0 and 10 s-1, and deformation temperature was ranged between 300-500°C with 100°C temperature steps. Using the flow curves obtained from the Gleeble tests, the constitutive behavior of the materials was developed. Moreover, dislocation density and stored energy after hot deformation of AA3XXX aluminum alloys were calculated.

The deformed materials were characterized using optical microscopy and image analyzing software to measure as-cast area fraction of the constituent particles and the size and aspect ratio of the constituent particles before and after hot deformation. Recovery model is able to capture the softening behavior of the Al-1%Mn alloy that has a close chemical composition to an alloy with 0.05 wt% Mn.

Acknowledgements

Table of Contents

List of Figures

List of Tables

Chapter 1 Introduction

AA3xxx aluminum alloys belong to the non- heat treatable wrought aluminum alloys group. The major alloying element for this group is manganese (Mn). In order to achieve desired mechanical or metallurgical properties, some other alloying element can also be added such as: Fe, Si, Mg, Ca [1, 2]. Good formability, weld-ability, corrosion resistance, high thermal conductivity and medium strength lead to extensive use of AA3xxx aluminum alloy in the packaging and heat exchanger industry as well as for home appliances.

The typical processing route for AA3xxx series allows includes Direct Chill (DC) casting, followed by homogenization, hot and cold rolling and final heat treatment. The presence of Fe, Mn, and Si in this alloy promotes the formation of intermetallic particles during solidification which are called constituent particles [3].These alloying elements can also encourage the formation of dispersoids which are particle during the homogenization process, and reduce the Mn content in solid solution.

Sheet metal production of aluminum in industry starts with formation of aluminum alloy ingot via the DC casting process to produce rolling ingots. In order to homogenize the alloying elements in the as-cast ingot and remove micro segregation, the rolling ingots are homogenized by heating them to the desired temperature and holding them for several hours prior to hot rolling. In aluminum production, hot rolling mills include both break down and tandem mills. Break down mills typically reduce the ingot from 500 mm to 25-30 mm in a number of passes and then hot tandem mills reduce the transfer gauge slab from 25mm to 3-4mm. Tandem mills typically consist of 3-4 stands. After hot rolling, cold rolling and final annealing are the final steps to produce the aluminum sheet. In order to achieve desired properties in the final sheet metal product, the manufacturing sequence, shown in Figure 1, should be optimized with respect to the production of appropriate sheet microstructure and mechanical properties as well as energy usage.
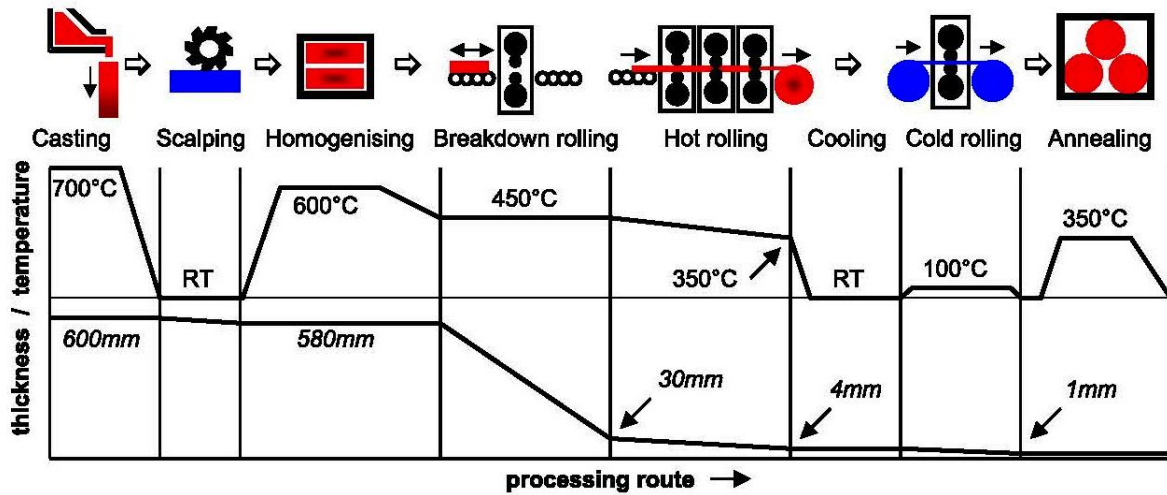
Figure 1: Overview of the different steps during the production of the AA3xxx series sheet alloy containing approximate thickness and temperature of each step.

Through Process Modeling, TPM, of the AA3xxx aluminum alloy is a research interest of the industrial partner in this research program – Novelis. The research program is multi-disciplinary in nature and includes partners from McMaster University as well as the University of Waterloo. The overall objective of this program is to develop a TPM including macroscopic effects such as thermal history as well as microstructure evolution for the entire manufacturing process from DC casting through to final cold rolling and heat treatment for AA3xxx model alloys. More specifically, this includes examining the microstructure evolution during DC casting of three 3xxx aluminum alloys with different manganese contents (0.05, 0.29, 1.04 wt% Mn) at McMaster University in Canada in order to predict the final microstructure after casting. Moreover, homogenization models are being investigated in detail at Manchester University in the UK in order to predict the formation of the dispersoids. This research project is focused on the hot deformation section of the sheet manufacturing process and the objective is to develop and apply a microstructure evolution model for recovery that occurs during hot deformation and identify how they are impacted by the starting microstructure as well as hot deformation processing history. Finally, there is complimentary work occurring at McMaster University trying to predict the microstructure changes during cold rolling and annealing of the aluminum sheet. By merging these sub models, an overall through process model can be obtained and used to understand the effect

2

of the processing history on the microstructure and property evolution in the sheet from a scientific basis versus trial and error.

Chapter 2 Literature review

The development of process models is of significant interest to industrial suppliers and users of aluminum alloys. Historically, these models examined individual metallurgical phenomena and their relationship to a particular process in the production chain. For example, in the early 1990's, Shercliff and Ashby developed a precipitation hardening model and applied this to welding of aluminum alloys [4, 5]. At this time, Ashby published an excellent paper describing a systematic approach to physical modeling of material problems [6]. During this time period, a framework for modeling of these problems, which came to be known generally as the internal state variable approach was formalized (see Richmond [7] and the review by Grong and Shercliff [8].

In the 2000's this approach was advanced to examine through process models where linkages between various processes had to explicitly accounted for, e.g. the effect of segregation during casting and its effect on formability of aluminum sheet alloys. An exemplary example of this work was the models which were developed in Europe to develop through process models for casting, homogenization, thermo-mechanical processing and production of final products [9]. These models were fully integrated so that history effects could be studied but were applicable to a number of generic aluminum alloys (i.e. AA3xxx packaging alloys and can body stock, heat treatable 6xxx alloys).

For aluminum casting of engine blocks and heads, the Ford Motor Company developed a set of coupled models which are known as the Ford Virtual Casting Model. This model included thermal mechanical stress finite element method models which were coupled

to metallurgical models for solidification and precipitation [10]. In this case, computational materials science was applied to aid the model development for important model parameters such as interfacial energies for precipitates in aluminum [11]. The Ford Virtual Casting Model was a founding example of what has become known as Integrated Computational Materials Engineering (ICME) in the USA [11] or through process modeling in other parts of the world. Recently, a study has been conducted to summarize some for the challenges for ICME and provide guidance on best practices in implementation strategies [12].

2.1 Homogenization treatment

2.1.1 Effect of homogenization treatment on constituent particles

Constituent particles forms during solidification and in 3xxx aluminum series these intermetallic phases are mainly $Al_6(Fe,Mn)$ and α-$Al(Fe,Mn)Si$ [13]. These particles remain until the final stage of the production route and have diameters about 1-10 ηm in the final product. During both hot and cold deformation, the constituent particles can play an important role as they can serve as nucleation sites for recrystallization via particle stimulated nucleation, PSN. As a result, these particles can greatly influence the recrystallization and texture in the final sheet [14].
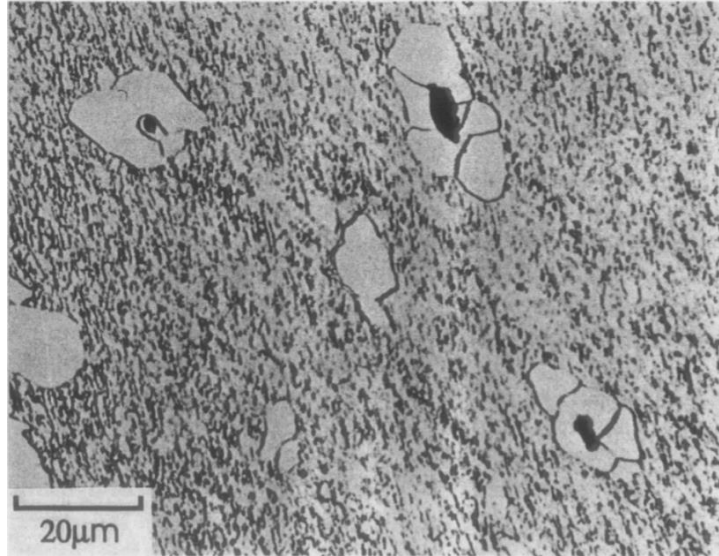
Figure 2: Nucleation of recrystallized grain at oxide particles in 60% rolled iron (2 minutes at 540 ℃) [15].

Constituent particles undergo some changes during the homogenization treatment like Ostwald ripening and spheroidisation and fracture during hot and cold rolling [16]. Alexander et al. investigated the $Al_6(Fe,Mn)$ to α-$Al_{12}(Fe,Mn)_3Si$ solid state eutectoid transformation in a 3xxx aluminum alloy. This transformation requires diffusion of silicon from the matrix to particle [16], as follows:

$$3\ Al_6(Fe,Mn) + Si \rightarrow \quad \alpha\text{-}Al_{12}(Fe,Mn)_3Si + 6\ Al$$
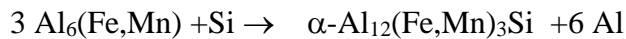
R.G. Hamerton et al. [17] have designed two 3xxx alloys in such a way that in one of them the predominant intermetallic phase is $Al_6(Fe,Mn)$ and in the other one is α phase in order to evaluate the effect of heat treatment and deformation temperature of these constituents separately, involving plain strain compression tests at 360 and 530 ℃. In order to evaluate the effect of heat treatment on the final product, two heat treatments of short (1

hour) and long 5(days) at 600 ℃ have been done before the hot deformation. The number of density of particle for the research is shown in Figure 3.
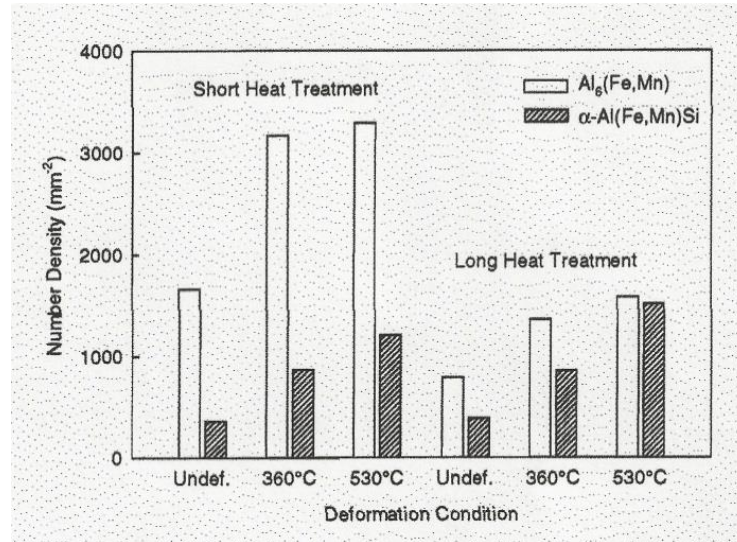
Figure 3: Constituent particle number density in different deformation conditions [17]

By comparison between number densities of constituent particles in un-deformed and deformed samples, Figure 3, it is clear that particle fracture and break-up occurred during deformation. Figure 3 shows that in the alloy containing Al_6(Fe,Mn), the particle number density is more dependent on the type of the heat treatment, than deformation temperature of 360 ℃ or 530 ℃ while the alloy containing α constituent particles does not follow that trend. SEM images of the particle morphologies for alloy 1 and alloy 2 in different stages are shown in Figure 4 and Figure 5. Al_6(Fe,Mn) has an acicular shape in as-cast sample and after long heat treatment, they become coarser. In contrast, α phase has a script-like shape. This blocky branch separates to an equiaxed shape during homogenization to some extent and also during hot deformation.

7

As-cast   Short heat treatment   Long heat treatment   Deformed at 530°C
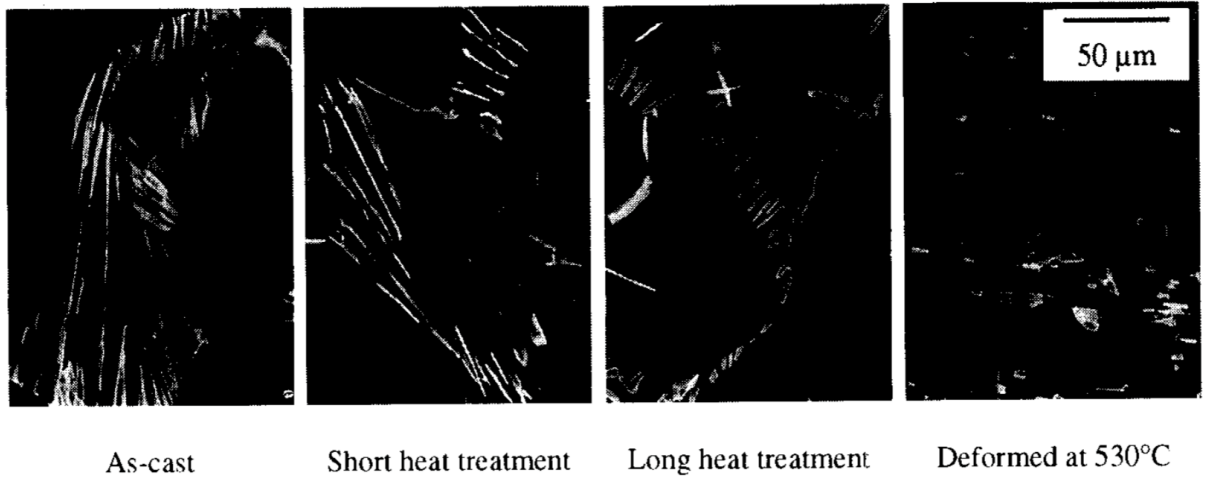
Figure 4: Al_6(Fe,Mn) particle morphology at different stages of the homogenization heat treatment and deformation [17]

As-cast   Short heat treatment   Long heat treatment   Deformed at 530°C
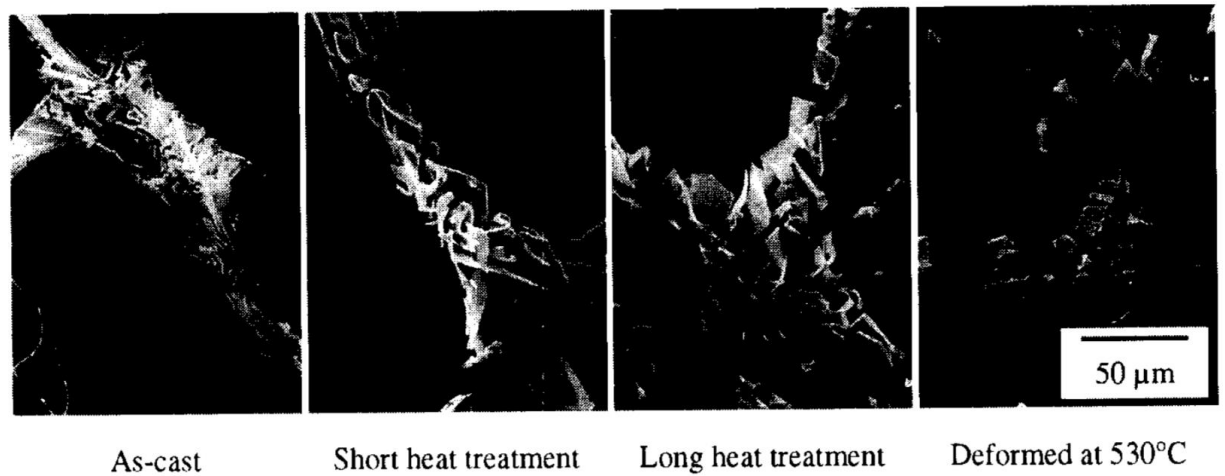
Figure 5: α-Al(Fe,Mn)Si particle morphology at different stages of the homogenization heat treatment and deformation [17].

By considering Figure 3 and the lower incidence of breakup of the constituent particles during long heat treatment times comparing to short heat treatment, Hamerton et al. claims that the initial particle morphology plays a more important role compared to the particle itself. Short heat treatment times do not change the morphology of the Al_6(Fe,Mn)

8

and α-$Al_{12}(Fe,Mn)_3Si$ phase significantly. In contrast, The morphologies of both the $Al_6(Fe,Mn)$ and α-$Al_{12}(Fe,Mn)_3Si$ phases become more similar by holding the two alloys for a long time of 5 days in long heat treatments and Hamerton et al. believe that this similarity in morphologies is the result of the same trend of segmentation of the constituent particles in these two alloys in a long heat treatment.

In industrial AA3XXX aluminum alloys, due to the existence of different alloying elements and trace elements and maybe the existence of a grain refiner and local solidification condition in different parts of the cast ingot, usually a mixture of constituent particles are available. It is obvious the results in this case are different comparing then results which only one phase considered like that of Hamerton's research.

Alexander et al. [18], have done a detailed investigation on particle break up in a aluminum alloy with 0.5 wt% Fe and 1 %Mn and 0.2wt% Si containing both $Al_6(Fe,Mn)$ and α phases during homogenization. It was shown that transformation of the $Al_6(Fe,Mn)$ and α phases can also occur during homogenization treatment on constituent particles too for heat treatments more than 2 hours at 600°C. The aluminum wets the duplex boundary of $\alpha/Al_6(Fe,Mn)$ and gradually penetrates between them and makes a separation of the constituents into two smaller phases, see Figure 6 and Figure 7. Another reason to break up the constituent particles during homogenization is related to different thermal expansion coefficient of the aluminum matrix and these constituents. Higher thermal expansion coefficient for aluminum matrix leads to the occurrence of internal tensile stress during heating on constituent and leads to fragmentation of that due to this mechanical force. This fragmentation happens usually perpendicular to the larger axes of the constituent particles [16].
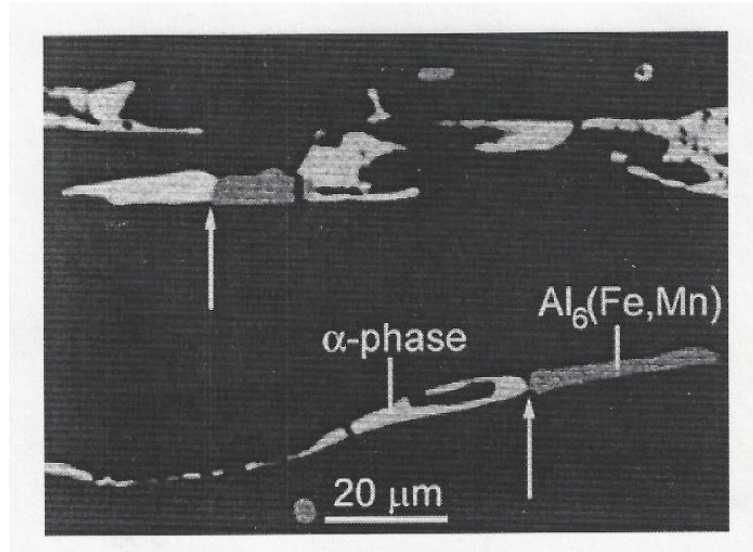
Figure 6: Backscattred electron SEM image of the model 3000 alloy heat treated for 2 hours at 600 ℃ [16].
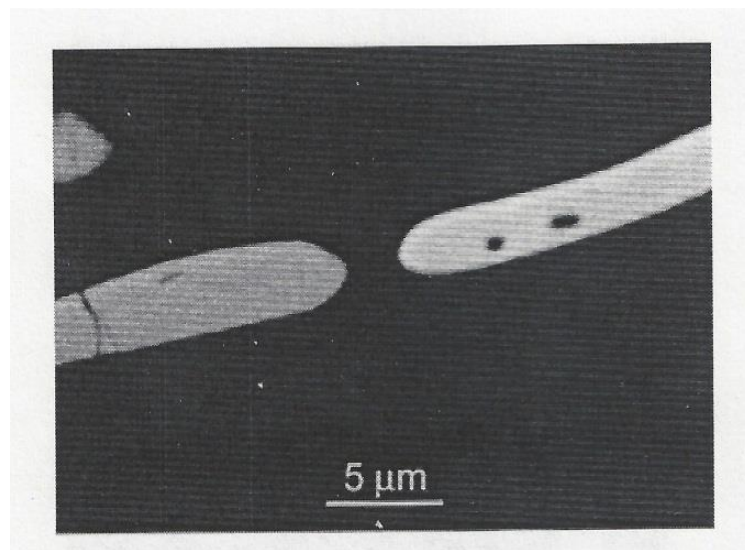
Figure 7: Backscattred electron SEM image of the model 3000 alloy heat treated for 2 days at 600 ℃ [16].

Although particle break up during hot rolling of other aluminum alloy series like AA5182 has been investigated in detail [19] recently, there is still little knowledge on the evolution of the constitute particles during hot rolling of the 3xxx aluminum alloys.

2.1.2 Effect of homogenization treatment on dispersoid particles

Hsin-Wen Huang et al. [20] have studied 8 different homogenization heat treatments, single step and multi steps, and evaluate the dispersoids after different homogenization condition for A3003 aluminum alloy with the 1% Si, 0.5% Fe, 1.09% Mn and 0.12%Cu as alloying elements.
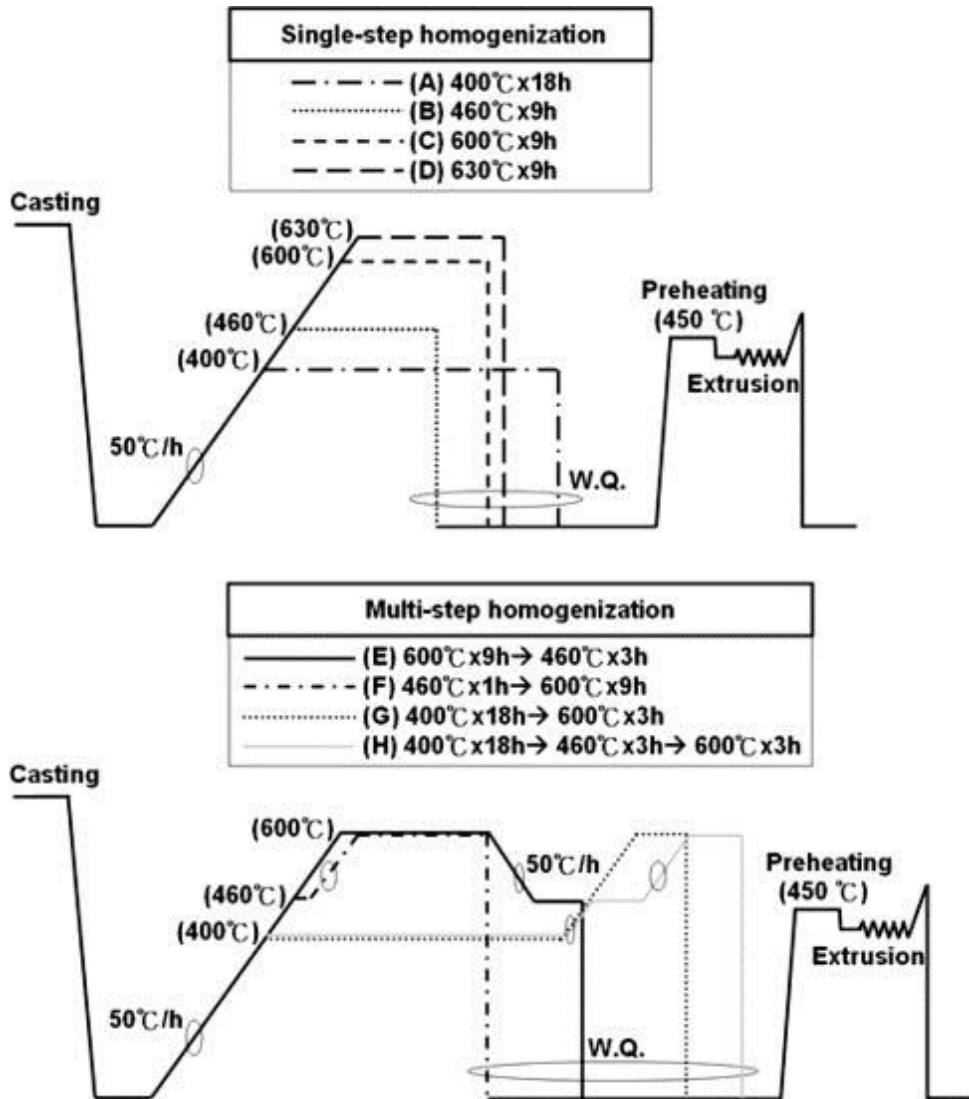
Figure 8: Different homogenization conditions for AA3003 aluminum alloy in Hsin-Wen Huang et al. research [20].

In single step homogenization treatments, the largest quantity of dispersoids and higher electrical conductivity is for case B since the diffusion rate at low temperature of 400 ℃ for case A is not sufficient enough to leave the aluminum matrix and form a dispersoid.

With EDS analysis, it has shown that gray dispersoids which formed mainly at low temperatures is $Al_6(Mn,Fe)$ and this particle can dissolve in aluminum matrix via Ostwald

ripening mechanism at higher temperatures and encourage the formation of black α-$Al_{12}(Mn,Fe)_3Si$ dispersoids.

By considering the TEM image of all 4 samples for single stage heat treatment and also TEM images for samples after each stage of the multi-step homogenization condition, a schematic for dispersoid formation is shown in Figure 9 for single step heat treatments and Figure 10 for two step heat treatments.

In two-step homogenization treatment, the shape of the final dispersoid is affected by the condition of the first stage of the homogenization treatment. According to the schematic and also shown in the TEM images, it is clear that the low temperature heat treatment of 460 ℃ for 1 hour still show its result for formation of some bar shape dispersoids and also low spheroidizing degree even after holding 9 hours at 600 ℃ in heat treatment F compare to heat treatment C which is only single step of holding 9 hours at 600℃.
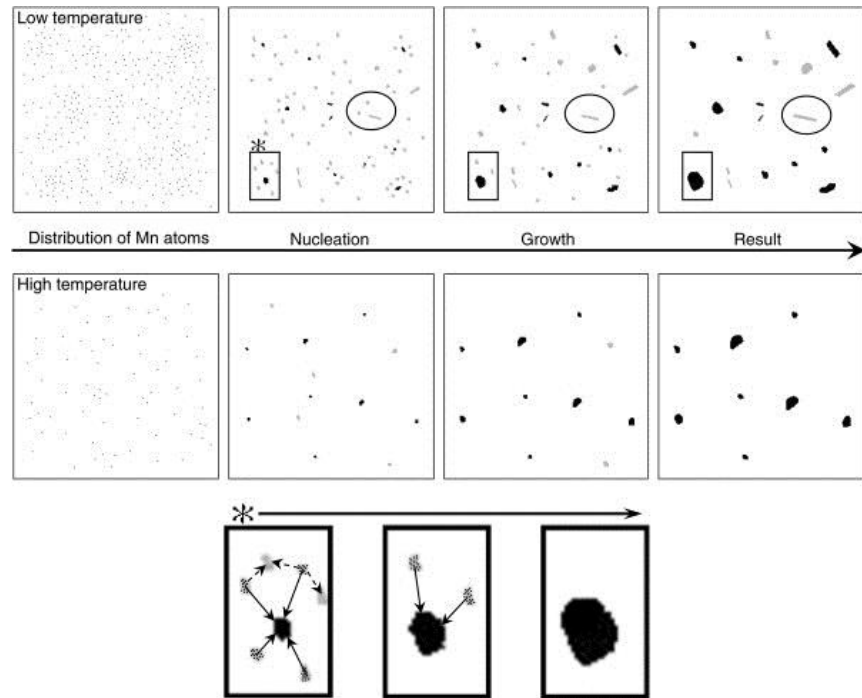
Figure 9: Model for precipitate evolution in single-step heat treatment [20].

It is interesting that for heat treatment E with high temperature treatment in first stage and lower in the second stage, formation of the $Al_6(Mn,Fe)$ dispersoids on the first dispersoids formed at high temperature, $\alpha\text{-}Al_{12}(Mn,Fe)_3Si$, is detected. On the other hand, heterogeneous precipitation forms in this case that leads the depletion of the solid solution from Mn and also low density of precipitation is formed in this condition.

Dispersoid modeling during homogenization treatment of the 3xxx aluminum alloys has been done by Suni et al. [21] by applying the equations for nucleation, growth and coarsening and predicting the dispersoid size, number density and volume fraction of dispersoids.
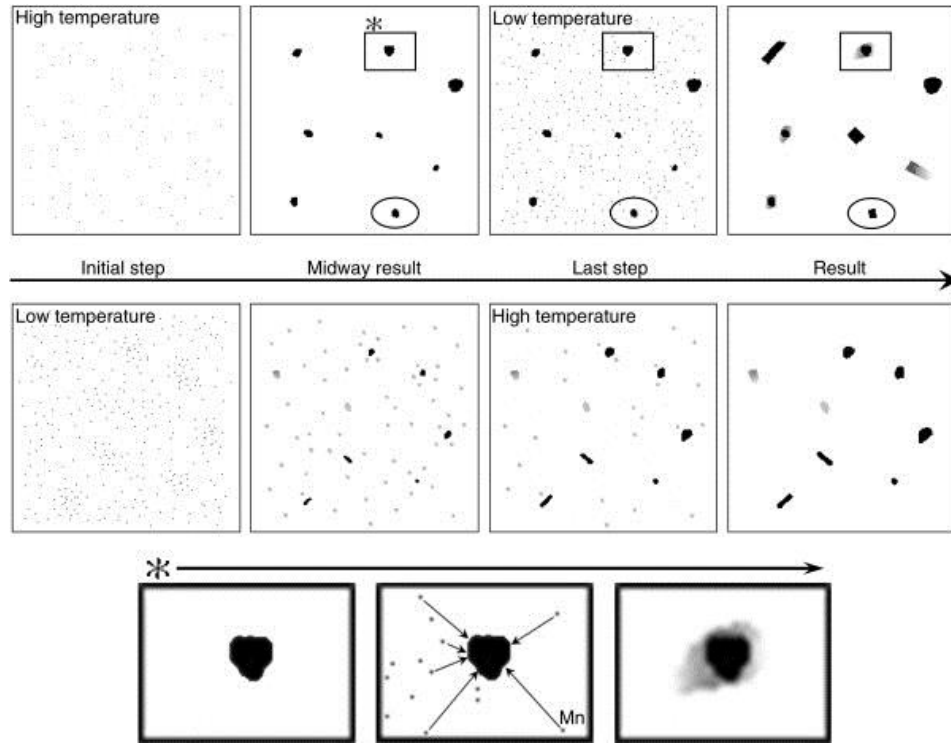
Figure 10: Model for precipitate evolution in multi-step heat treatment [20].

2.2 Hot deformation

2.2.1 Constitutive behavior

Knowledge about the stress-strain behavior of the material at high temperatures and the constitutive behavior of the material at elevated temperatures is crucial to design hot production processes especially when computer simulation is used. Sellars and Tegart proposed a function, Equation 1, and the Zener-Holloman equation can be used in order to predict the constitutive behavior of the AA3xxx aluminum alloy during hot deformation.

$$\dot{\varepsilon} = A\,[sinh(\alpha\sigma)]^n exp(-\frac{Q}{RT}) \qquad \text{Equation 1}$$

$$Z = \dot{\varepsilon} \exp\left(\frac{Q}{RT}\right) = A\left[\sinh(\alpha\sigma)\right]^n \qquad \text{Equation 2}$$

Where n, α and A are constants and Q is activation energy for hot working. For 3003 aluminum alloy, it is recommended that $\alpha = 0.052$ Mpa^{-1}, the stress exponent n=2.53 and activation energy of hot working Q=152KJ/mol [22]. Slight changes in the Mn content results of different values for Q and n. For Mn=0.8, Q= 159KJ/mol and n=6.6 is reported [23] and for Mn=1.06, Q=180kJ/mol and n=3.1 is reported by McQueen et al. [24] suggest that a value of $\alpha = 0.052$ MPa^{-1} holds for AA3xxx aluminum alloys which is widely accepted.

2.2.2 Microstructure evolution

2.2.2.1 Recovery

The re-arrangement of the dislocation of the deformed microstructure, Figure 11 (a), at elevated temperature is called recovery. During recovery, climb of the edge dislocations and cross slip of the screw dislocations lead the annihilation of the deformed dislocations to some extent. The remaining dislocations form a cell wall inside the already existing grains. This process continues until subgrain structure forms inside the grain, Figure 11(b).

(a)   (b)
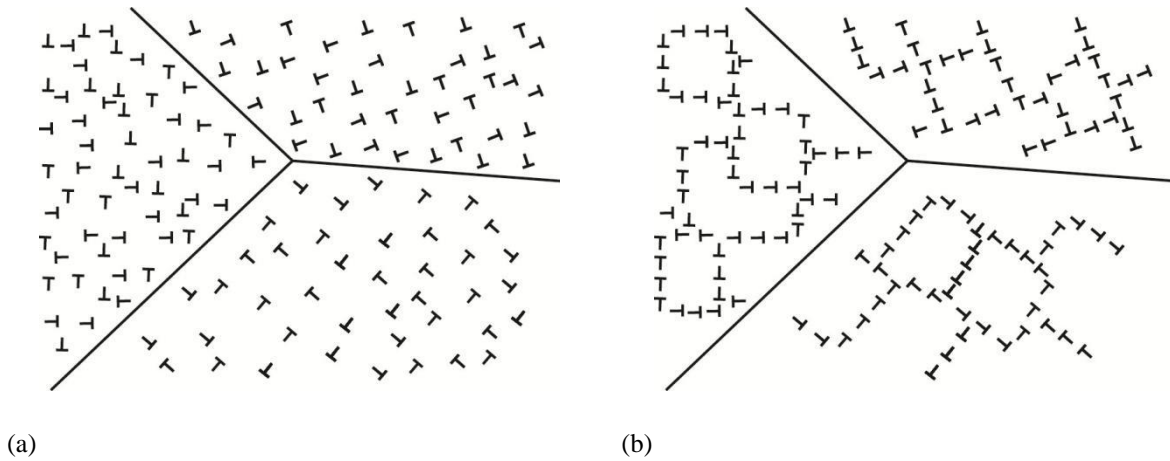
Figure 11: (a) : Dislocation structure in deformed microstructure, (b) : Dislocation structure in recovered microstructure

2.2.2.2 Recrystallization

Nucleation and growth of strain free grains in the deformed matrix is the process of recrystallization. This process contains the formation and growth of the high angle grain boundaries that is swept the deformed grains containing lots of dislocations even after recovery. The driving force for this process is the stored energy. Vatne et al. [25] introduced the concept of different nucleus sites for recrystallized grains: PSN, nucleation from cube bands and nucleation from grain boundary.
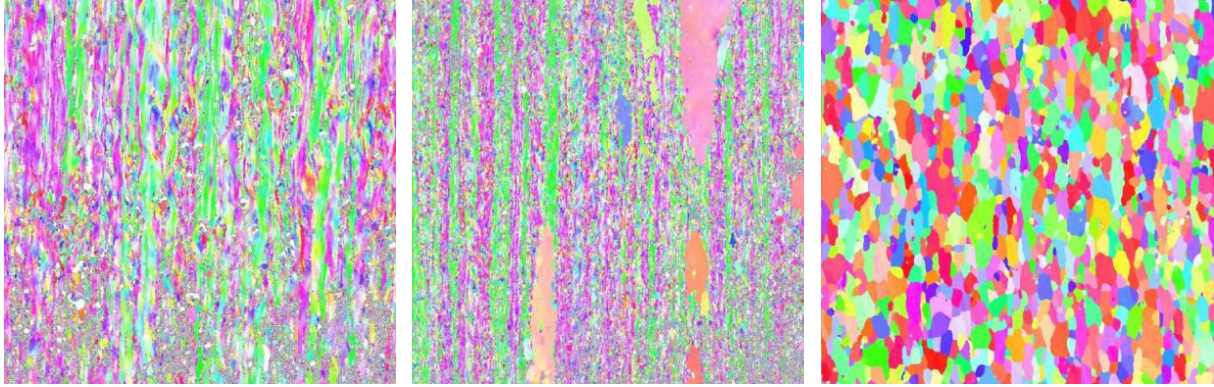
(a)   (b)   (c)

Figure 12: Schematic EBSD images of (a) As-deformed grain structure, (b) Grain structure after recovery, (c) Grain structure after recrystallization

In general, high stacking fault materials like aluminum exhibit a strong dynamic recovery process, DRV, to occur during hot forming. As a result, dynamic recrystallization, DRX, is not expected to occur during hot deformation for most aluminum alloys. Depending on the aluminum alloy and amount of dynamic recovery, recrystallization after deformation, static recrystallization, can occur.

Growth rate of the recrystallized grain depends on the mobility of the grain, M, and effective driving force as shown in Equation 3. P_D is the stored energy which is the driving force of the recrystallization and P_Z is the Zener drag pressure which is the retarding pressure of the recrystallization.

$$G = M(P_D - P_Z)$$

Equation 3

The mobility can be calculated with Equation 5 where M_0 is constant; U_{GB} is the activation energy for grain boundary, R is gas constant and T is temperature.

18

$$M = \frac{M_0}{RT} \exp(-\frac{U_{GB}}{RT})$$

During the annealing process, temperature also determines the recrystallization time. Recrystallization kinetic curves for 3004 samples deformed in torsion test and annealed at the indicated temperature are shown in Figure 13. Sample 1 was deformed at 250℃ at a strain rate of $1s^{-1}$ and annealed at 280℃. Samples 4,7 and 5,8 deformed at 400℃, strain rate of 1 and $10s^{-1}$ but 7,8 stopped at $\varepsilon=3$ while 4,5 deformed to strains of 8 and 4.5 respectively. All of the samples 4,5,7 and 8 were then annealed at 450℃. This shows that higher strain rate shift the 'S-shape" curve of the recrystallization kinetics to the left side in fraction recrystallized versus time at annealing temperature. In the constant strain rate, increasing the strain leads the shift of the curves to the right side. These are for the case that the deformed temperature is 400℃ and annealing temperature is 450℃. Schematic EBSD images of the grain orientation are shown for as-deformed grains structure, Figure 12 (a), and after recovery grain structure, Figure 12(b), and recrystallized grains, Figure 12 (c).
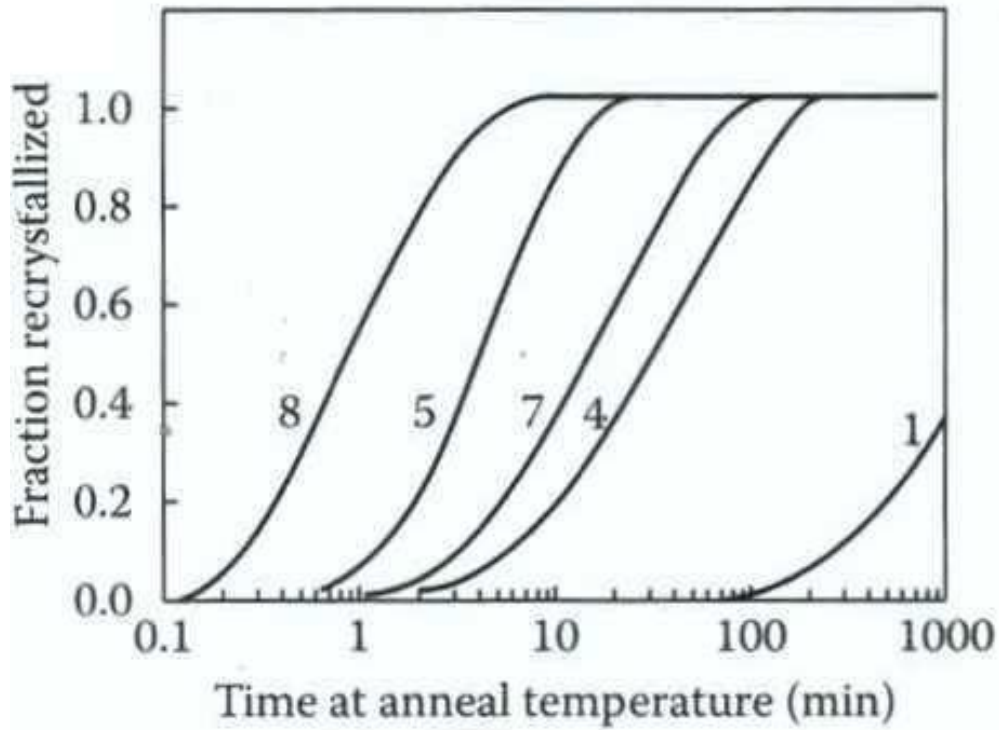
Figure 13: Recrystallization kinetic curves for 3004 samples deformed in torsion test [26].

2.2.2.3 Zener drag pressure

If the grain boundary touches the small particle, part of the grain boundary replaces by particle and respective energy of grain boundary is reduced. In order to separate from the particle again, this area should be regenerated, and as a result a back force is applied on the grain boundary referred to as a Zener force or Zener pinning pressure which is shown in Equation 5, where F_v is volume fraction of the particle, r is radius of the particle and γ is grain boundary energy [27].

$$P_z = \frac{3F_V\gamma}{2r}$$

Equation 5

20

2.2.3 Microstructure modeling

Hot deformation process modeling at both a macro level and micro level are shown in Figure 14.
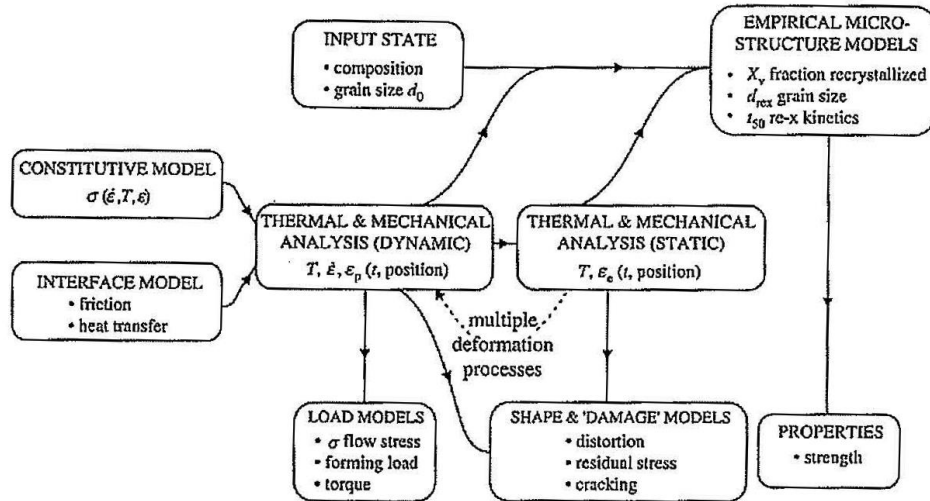
Figure 14: Thermo mechanical Process modeling at macro level
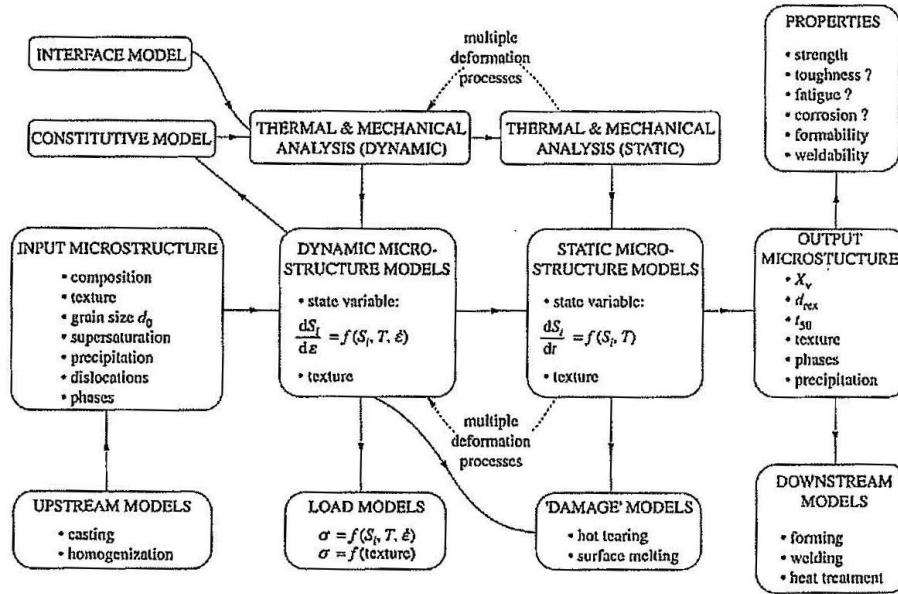
Figure 15: Thermo mechanical Process modeling at micro level

Shercliff [28] classifies major approaches for microstructure evolution modeling in hot deformation.

2.2.3.1 Empirical Method

Models based on empirical methods using empirical equations with some material constant which need experimental measurements in order to calculate or determine these constants and it does not require knowledge of certain characteristics of the physical processes involved in the evolution microstructure [28].

One example of empirical type equations to describe recrystallization is provided in Equations 15 to 17. These equations calculate: time at which 50% of the structure is recrystallized, t_{50}, recrystallized grain size, Drex, and grain size after grain growth. In these equations, p, q, r, u, p', q', r', u', v and y are empirical constants. The relationship for volume fraction recrystallization X_v and holding time is presented using the well-known Johnson-

Mehl-Avrami-Kolmogorov equation (JMAK), Equation 9. Another way to show the JMAK equation is shown in

$$t_{50} = pD_i^q Z^{-r} \varepsilon^{-u} exp\left(\frac{Q_{SRX}}{RT_A}\right)$$

Equation 6

$$D_{SRX} = p'D_i^{q'} Z^{-r'} \varepsilon^{-u'}$$

Equation 7

$$D_{GG} = D_{SRX}\left[1 + vtexp\left(\frac{Q_{GG}}{RT_A}\right)^y\right]$$

Equation 8

$$X_v = 1 - exp\left\{-0.693\left(\frac{t}{t_{0.5}}\right)^n\right\}$$

Equation 9

$$X_v = 1 - exp(-Kt^n)$$

Equation 10

2.2.3.2 Physically based state variable model

Physically based state variable models mostly involve explicit incremental calculation of state variables of which the initial values can be measured experimentally [29]. Parameters such as dislocation density, subgrain size and misorientation to predict flow stress and subsequent recrystallization can be calculated with these physical based models. The general form of differential state variable equation for hot deformation is:

$$\frac{dS_i}{dt} = f_1(S_1, S_2, \dots, T, \dot{\varepsilon})$$

Equation 11

where S_i represents the state variables. Flow stress is described by a function of the state variables:

$$\sigma = g_1(S_1, S_2, \dots)$$

Equation 12

Sellars and Zhu [30] developed a model to predict the internal state variable evolution during hot working and subsequent recrystallization parameters of a 5xxx aluminum alloy under both transient and steady state deformation conditions.

$$d\rho_r = d\rho_r^+ + d\rho_r^- = \left(C_1 \rho_r^{0.5} - C_2 \frac{\sigma_f}{Z} \rho_r \right) d\varepsilon$$

Equation 13

Where ρ_r, δ and θ are density of random dislocations, subgrain size and misorientation, respectively. The evolution of subgrain size and misorientation between the subgrains are shown in Equation 14 and Equation 15and ε_δ and ε_θ are characteristic strains influencing the subgrain size and misorientation, respectively. δ_{ss} and θ_{ss} are subgrain size and misorientation during steady state deformation.

$$d\delta = \frac{\delta}{\varepsilon_\delta \delta_{ss}} (\delta_{ss} - \delta) d\varepsilon$$

Equation 14

$$d\theta = \frac{1}{\varepsilon_\theta} (\theta_{ss} - \theta) d\varepsilon$$

Equation 15

Steady-state subgrain size has been characterized as a function of Zener-Holloman parameter and can be calculated via Equation 16:

$$\delta_{ss} = A + B \ln Z$$ <div align="right">Equation 16</div>

where A and B are constants.

Sellers assumes the recrystallization nucleation occurs mainly along the grain boundaries and hence the nucleation density, N_v, is a function of subgrain size, δ, and S_v which is the grain boundary area per unit volume.

$$N_v = \left(\frac{C_3}{\delta^2}\right) S_v$$ <div align="right">Equation 17</div>

The recrystallized grain size can be calculated from the nucleation density for the case of site-saturation nucleation as shown in Equation 18.

$$D_{rex} = A N_V^{-1/3}$$ <div align="right">Equation 18</div>

Time to fifty percent recrystallization can then be calculated according to Equation 19.

$$t_{50} = C_4 P_D^{-1} N_V^{-1/3}$$ <div align="right">Equation 19</div>

2.2.3.2.1 Stored energy

Formation of dislocations and their interaction with each other yields higher strength in deformed metals. An indirect way of estimating dislocation density is through the measured flow stress of the material. Mcelory et al. [31] shows the relationship between dislocation density and flow stress using Equation 20 where C1 is assumed 0.5 and μ is shear modulus and b is the Burgers vector.

$$\sigma = c_1 \mu b \rho^{1/2}$$ <div align="right">Equation 20</div>

The stored energy, the driving force for recovery and recrystallization, can be calculated by consideration of the dislocation density of the material and energy per unit length of the dislocation and it is shown in Equation 21 .The value of constant C2 is also in the order of 0.5 [32]. Due to simplicity of the Equation 21, many researchers use this equation to find the stored energy [33, 34, 35].

$$P_D = c_2 \rho \mu b^2 \hspace{4cm} \text{Equation 21}$$

Vatne et al. [25] presented more complex calculation in order to find stored energy for hot deformed materials. In steady state condition, subgrains contain well deformed dislocation network as boundaries and there are scattered dislocations inside subgrains. The stored energy of this structure can be calculated from Equation 22 where γ_{SB} is the average subgrain boundary energy, δ is average subgrain size after deformation, ρ dislocation density inside the subgrain, Γ is dislocation line tension and α is geometric constant on the order of 3.The first term in Equation 22 is due to dislocations forming the subgrain wall and second term is due to dislocations inside the subgrains. The relationship between dislocation density and subgrain size during steady state condition is shown in Equation 23 where C_p is a constant of the order of 5.

$$P_D = \alpha \frac{\gamma_{SB}}{\delta} + \rho \Gamma \hspace{4cm} \text{Equation 22}$$

$$\rho^{0.5} = C_p \frac{1}{\delta} \hspace{4cm} \text{Equation 23}$$

The Read-Schockley relation is used to calculate the subgrain boundary energy in Equation 24 where μ is shear modulus, ν is Poisson ration, b is burgers vector, θ is the average subgrain disorientation, around 5° after hot deformation, and θ_c is critical misorientation for

a high angle boundary of the order 15°. Equation 25 shows the dislocation line tension. As a summary, the recrystallization driving force can be calculated with Equation 26.

$$\gamma_{SB} = \frac{\mu b \theta}{4\pi(1-\upsilon)} ln\left(\frac{e\theta_c}{\theta}\right) \qquad \text{Equation 24}$$

$$\Gamma = 0.5\mu b^2 \qquad \text{Equation 25}$$

$$P_D = \frac{\mu b}{\delta}\left[\frac{\alpha\theta}{4\pi(1-\upsilon)} ln\left(\frac{e\theta_c}{\theta}\right) + 0.5 C_p^2 \frac{b}{\delta}\right] \qquad \text{Equation 26}$$

During non-steady state condition, Engle et al. [36] used Equation 26 and P_D, δ and ρ are function of time. The significance of the first term in stored energy in Equation 26 is much more than the second term which is related to the dislocations inside subgrains. As a result, some researchers like Eivani [37] have applied Equation 27, and the first term of Equation 22, in order to calculate the stored energy during annealing after hot deformation.

$$P_D = 3\frac{\gamma_{SB}}{\delta} \qquad \text{Equation 27}$$

Sellers [30] applied another equation in order to find stored energy. Random dislocation density, ρ_r, and geometrically necessary dislocation density, ρ_g, are under the term of internal dislocation density, ρ_i. θ is misorientation, δ is space of dislocation wall. θ_c Critical value of misorientation angle that distinguish LAGB from HAGB (approximately 15°)

$$P_D = \frac{\mu b^2}{10}\left[\rho_i\left(1 - ln(10b\rho_i^{0.5})\right) + \frac{2\theta}{b\delta}\left(1 + ln\left(\frac{\theta_c}{\theta}\right)\right)\right] \qquad \text{Equation 28}$$

2.2.3.1 Advanced statistical methods

Statistical methods, although useful in process control and final prediction of the microstructure after hot deformation, provide very little physical insight into the details of the relationships between the metallurgical evolutions, final material properties and hot deformation conditions as all correlations tend to be completely empirical in nature, and Artificial neural network (ANN) and Gaussian process models are examples of this method.

Recently, Jenab et al. [38] applied a statistical method model to predict flow behavior of AA7075 at low strain rates hot deformation and they compare the root mean square error (RMSE) calculated from the difference of measured and calculated values from the different models of ANN, Hyperbolic-sine and power law. It is shown that the ANN model has the best prediction compare other methods. Liu et al. [39] derived a constitutive model for 2A70 Aluminum by using of ANN method.

2.3 Annealing Process

Recovery and recrystallization can also happen during annealing of the hot deformed metal after the hot deformation process.

2.3.1 Recovery model during annealing process

Modified static recrystallization model is presented by Verdier et al. [40], see Equation 29.

$$\frac{d\tilde{\sigma}}{dt} = -E\frac{\tilde{\sigma}^2}{M_{Taylor}^3\alpha^2\eta^2}\nu_D\exp(-\frac{U_0}{K_BT})Sinh(\frac{\tilde{\sigma}\nu}{K_BT})$$

Equation 29

Where E is Young's modulus, M_{Taylor} is Taylor factor , α is 0.3, μ is shear modulus , ν_D is Debye frequency, K_B is Boltzmann constant , U_0 is activation energy and ν is activation volume. $\tilde{\sigma}$ is the dislocation frost contribution to the flow stress and it is related to dislocation density and the relation between them is shown in Equation 30.

$$\tilde{\sigma} = M_{Taylor}\alpha\mu b\sqrt{\rho}$$

Equation 30

Lens et al. [41] measured variation of the stored energy by recovery during annealing temperatures between 220 ℃ to 330 ℃ for Al-0.1% Mn alloy and between 350 ℃ and 390 ℃ for Al-0.3% Mn , see Figure 16.
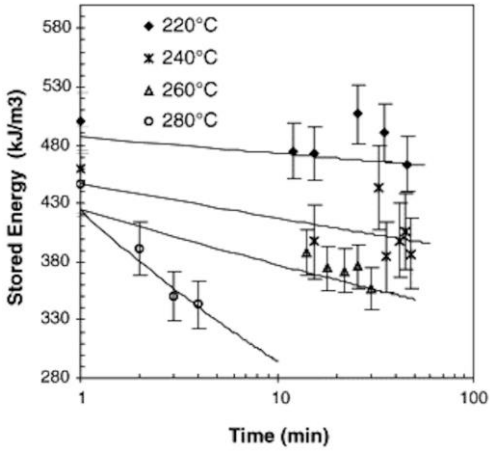
(a)
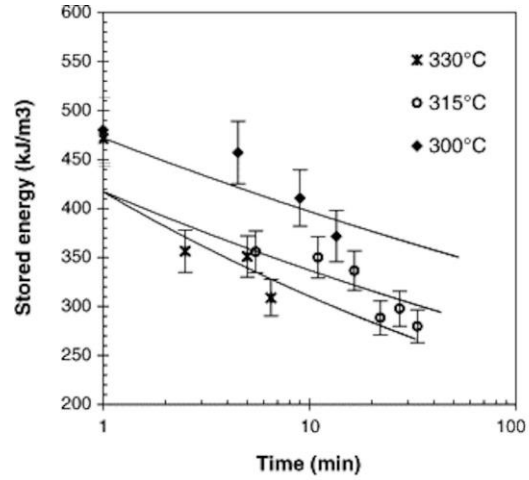
(b)
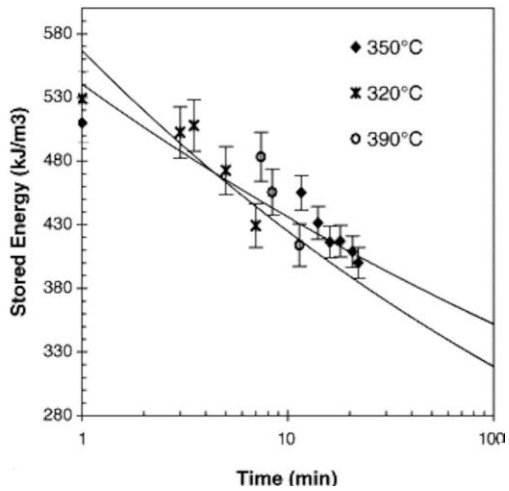
(c)

Figure 16: (a) Stored energy variation by recovery during annealing between 220 ℃ and 280 ℃ for Al-0.1% Mn, (b) Stored energy variation by recovery during annealing between 300 ℃ and 330 ℃ for Al-0.1% Mn, (c) Stored energy variation by recovery during annealing between 350 ℃ and 390 ℃ for Al-0.3% Mn [42].

2.3.2 Recrystallization model during annealing process

Vatne et al. [25] presented the recrystallization model for hot deformation of the aluminum based on the different nucleation sites for recrystallized grains including: particle stimulated nucleation (PSN), nucleation from cube bands and nucleation from grain boundaries. Here are some of the assumptions in his model:

- Steady state is reached during hot deformation. This condition is achieved for cases of strain higher than 0.5 and $Z < 10^{17}$,

- The final recrystallized structure is the result of growing grains which originate from different nucleation sites,

- Site saturation nucleation kinetics applies, and

- The nucleation sites are distributed randomly in the matrix

For PSN, it is assumed the random recrystallization nuclei form around non deformed particles during deformation. Equation 31, Gibbs-Thompson equation, shows the critical minimum particle size necessary for nucleation to occur, where η* is the critical particle size and γ_{GB} is the specific grain boundary energy between the nucleus and deformed matrix which is in the order of 0.3 J/m^2 [25]

$$\eta^* = \frac{4\gamma_{GB}}{P_D - P_Z}$$

Equation 31

Vatne shows the density of PSN nuclei (N_{PSN}) in Equation 32 where C_{PSN} is an empirical model constant provides the average number of nuclei generated from each particle, N_0 and L are derived from the frequency distribution of the particles.

$$N_{PSN} = C_{PSN} N_0 \left(-\frac{4L\gamma_{GB}}{(P_D - P_Z)} \right)$$

<div align="right">Equation 32</div>

In the case of the cube recrystallization, old cube grains which originally existed in the primary material remain in a metastable condition after hot deformation and can form a band-like shape, thereby providing nucleation sites for recrystallization. The calculation for the number of cube nuclei are givne in Equation 30 where C_C is an empirical model parameter of the order of 1, $\bar{\delta}_c$ is the average cube subgrain size, $\bar{D}$ is initial average grain size, R_S is the fraction of the cube bands surrounding by the S deformation texture component and S_c^* in density of the subgrains inside the cube regions with diameter larger than a critical value.

$$N_c = \frac{2C_c \bar{\delta}_c R_c (1 - R_c) R_s S_c^*}{\bar{D}} [\exp(\varepsilon) + \exp(-\varepsilon) + 1]$$

<div align="right">Equation 33</div>

The grain boundary nucleation site density can be calculated using Equation 34 were C_{GB} is an empirical modeling constant.

$$N_{GB} = \frac{C_{GB} \bar{\delta} (1 - R_c) S_{GB}^*}{\bar{D}} [\exp(\varepsilon) + \exp(-\varepsilon) + 1]$$

<div align="right">Equation 34</div>

The total number of nucleation sites is the summation of all above three described nucleation densities. Relationships between subgrain size and the Zener Hollomon parameter during steady state hot deformation are given in Equation 35 and Equation 36. Both Equations show approximately similar subgrain size for $Z > 10^{12}$ but Equation 36 gives a reasonable subgrain size for lower Z values and this equation is used in the Vatne model.

$$\frac{1}{\delta} = A \ln Z - B$$

<div align="right">Equation 35</div>

$$\frac{1}{\delta} = \frac{RT}{A^*} \ln\left(\frac{Z\delta^2}{B^*}\right)$$

<div align="right">Equation 36</div>

Finally, the well-known Johnsen-Mehl-Arvarmi-Kolmogorov, JMAK, equation is used to determine the kinetics of recrystallization and it is shown in Equation 37. X(t) shows how much of the structure is recrystallized after an annealing time of t and $X_{ext}(t)$ shows the extended volume which is a function of grain growth and total number of nuclei and time given in Equation 38.

$$X(t) = 1 - \exp[-X_{ext}(t)]$$

<div align="right">Equation 37</div>

$$X_{ext}(t) = \frac{4}{3}\pi N_{TOT}(Gt)^3$$

<div align="right">Equation 38</div>

Vatne assumes that any kind of three nucleation sites present to the recrystallization texture according to their relative strength.

$$R_i = \frac{N_i}{N_{TOT}}$$

<div align="right">Equation 39</div>

Subgrain size changes during annealing time and temperature and subsequently influence of the stored energy. Equation 40 shows how subgrain size changes during annealing [43]. δ_0 is initial subgrain size at the start of annealing, α_s is a shape factor in the order of 1.5 and M_s is the mobility of low angle grain boundary.

$$\delta = \delta_0 + \left(\frac{P_Z\delta_0 - 2\alpha_s\gamma_s}{2\alpha_s\gamma_s}\right)\left(\delta_0 - \sqrt{\delta_0^2 + 8\alpha_s\gamma_s M_s t}\right)$$

<div align="right">Equation 40</div>

Eivani used the PSN [37], Equation 41, and grain boundary nucleation, Equation 42, in this model for AA7020 aluminum alloy. d_G is average grain size.

$$N_{PSN} = Hexp\left(-L\left(\left(\frac{K_d}{\dot{\varepsilon}T_{HW}}\right)exp\left(\frac{-Q_{HW}}{RT_{HW}}\right)\right)^{0.5}\right)$$

<div align="right">Equation 41</div>

$$N_{GB} = \frac{1}{\delta^2}\frac{2}{d_G}[\exp(\varepsilon) + \exp(-\varepsilon) + 1]$$

<div align="right">Equation 42</div>

Nucleation is thermally activated process shown with Equation 43 [37]. Q_N is activation energy for nucleation.

$$\dot{N} = (C_{GB}N_{PSN} + C_{PSN}N_{PSN})\left(\frac{P_D - P_z}{P_D}\right)exp\left(-\frac{Q_N}{RT}\right)$$

<div align="right">Equation 43</div>

Zener drag pressure can be calculated with Equation 44 where γ is the surface energy of grain boundry which the dispersoid pin and N_{V_i} is the number of dispersoids per unit volume with a radius of r_i.

$$P_Z = 2\pi\gamma\sum_i N_{V_i}r_i^2$$

<div align="right">Equation 44</div>

Hersent et al. [44] coupled the precipitation model for dispersoid formation during annealing with the recrystallization model together during annealing process subsequent to the cold rolling of AA3xxx aluminum alloy. It has been shown that recrystallization is retarded with concurrent precipitation of new phases. At low temperatures, the recrystallization can even stop since formation of new precipitates leads to an increase of Zener drag pressure and becomes even larger than driving pressure of recrystallization.
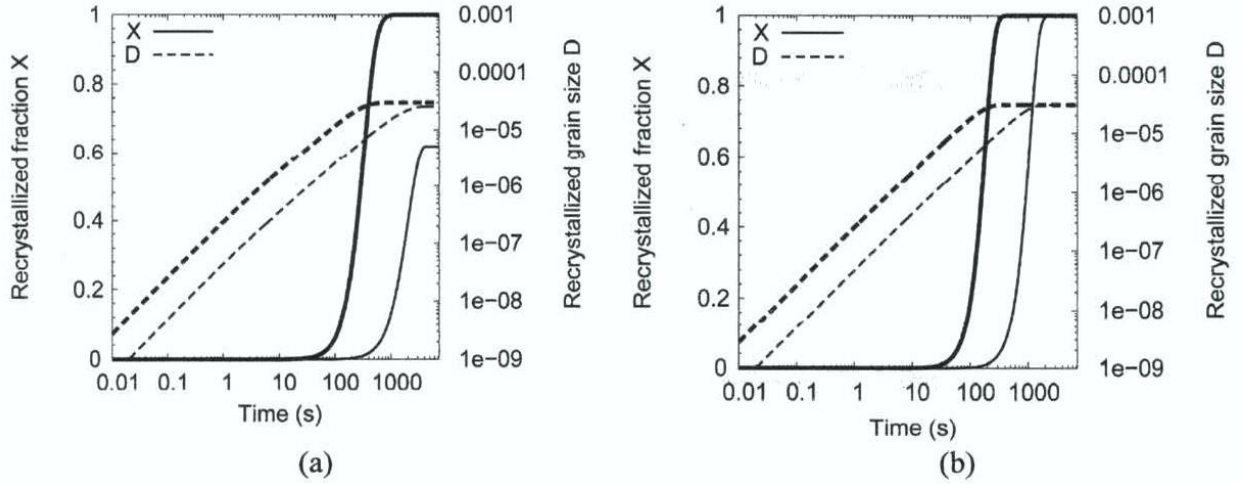
Figure 17: Rex fraction and grain size annealed at 300 ℃ (thin lines) and 325 ℃ thick lines. a) When the two models are coupled and b) when the Rex model is run alone with the same initial conditions for AlMnFeSi alloy [44].

Another new approach to find the kinetic of the recrystallization during annealing is presented by Marthinsen et al. [45]. Time-dependent nucleation of recrystallization, Equation 45, and the JMAK approach for recrystallization kinetic are merged and the results are compared with the site saturation approach, Figure 18.

According to this model, only a small fraction of potential nucleation sites in Equation 31, η^* in Gibb's Thomson equation, start to recrystallize. It this condition, the nucleation rates at different nucleation sites are calculated by corresponding nucleation frequency $v_s(t)$ times the number of potential but not yet activated sites, $N_s^{pot} - N_s(t)$:

$$\dot{N}_s(t) = v_s(t)\left[N_s^{pot} - N_s(t)\right], \qquad S = GB, Cube, PSN$$ Equation 45

2.3.2.1.1 Effect of particles on REX

Existing of the second phase can promote or hinder recrystallization. Hard constitutive particles usually cannot deform and geometrically deformed dislocations around that particle can encourage formation of the nucleation by PSN for instance in the case of the

35

large particle like constituent particles. In the case of the fine particles, like dispersoids, it can hinder the motion of the dislocations and subsequently hinder or completely suppress the recrystallization process [27].
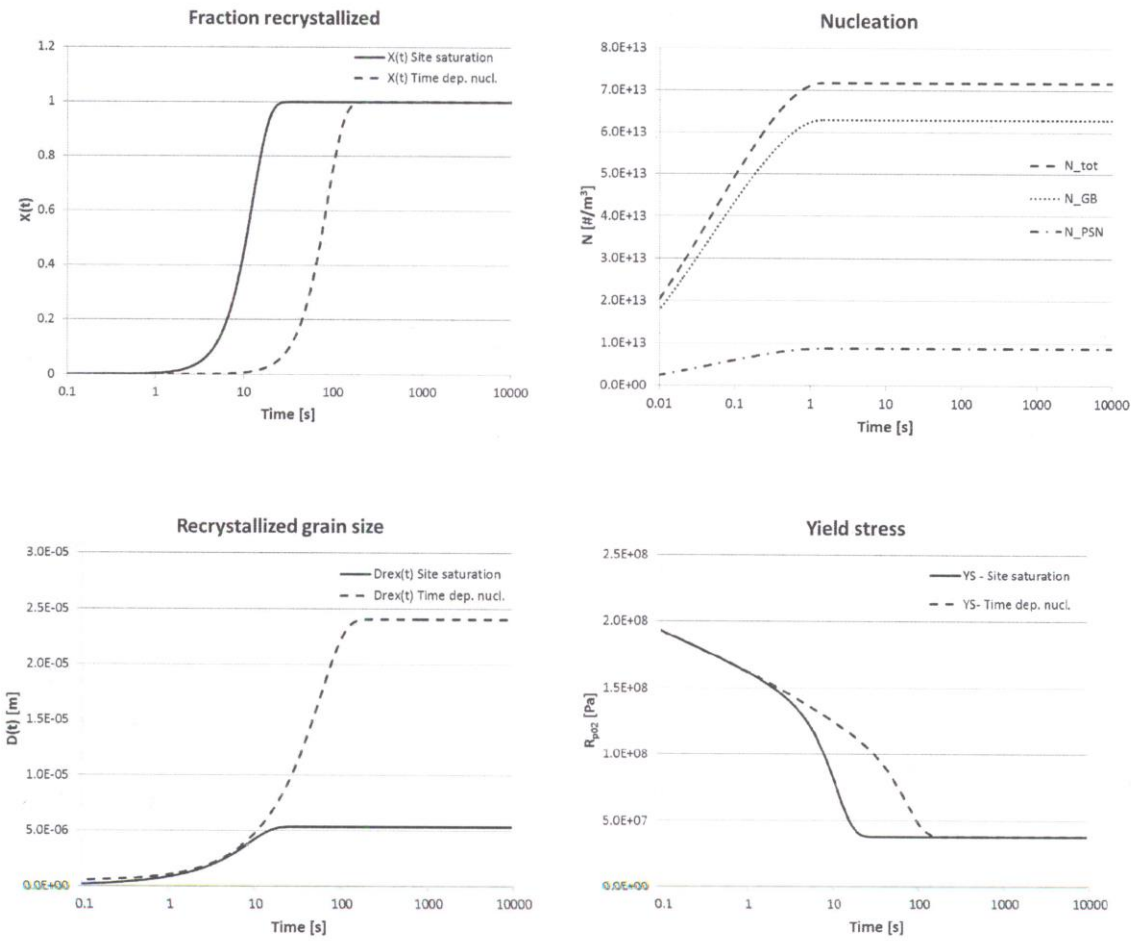
Figure 18: Modeling prediction, comparing to site saturation and time-dependent nucleation .a)Fraction recrystallized, b) Nucleation site densities, c) Recrystallized grain size, d) Yield stress [45].

Chapter 3 Scope and Objectives

Novelis, the largest fabricator of aluminum sheet, has been interested in knowledge based through process models of its sheet manufacturing operations. An important product they produce is the AA3xxx aluminum alloys which are subsequently used in can body stock applications. In order to satisfy the costumers with their requests for specific properties and microstructure, there need to be a good understanding of effects of process parameters and alloy composition on the final product. A research project has been defined between Novelis, McMaster University, Manchester University and the University of Waterloo to develop a through-process model of the sheet manufacturing process that includes casting, homogenization of the cast ingots, hot deformation and finally cold deformation and heat treatment. The whole project is a collaborative effort in which each stage of the process is being simulated individually and finally all the sub-models will be linked together to achieve a through-process model for the process.

In this work the main objective is to develop a basic quantitative model of recovery and experimental characterization of hot rolled microstructure to study the effects of initial microstructure and process parameters on microstructure of hot rolled material. The initial microstructure is mainly affected by alloy composition and homogenization conditions. The process parameters of interest are strain, strain rate, and temperature. The main contribution of this work is to elucidate the effects of Mn level and starting microstructure on the final microstructure evolution during and after hot deformation. Validation of model predictions will be performed via microstructural validation by microscopic observation of specimens prepared from hot deformed samples.

The detailed objectives of this work can be summarized as below:

- To determine the effect of homogenization conditions (time and temperature) on recrystallization in hot deformation

- To correlate hot deformation parameters (temperature, strain rate and strain) with microstructure of the hot deformed sample.

- To conduct microstructural measurements: microscopic observation of specimens prepared from hot deformed samples

- To analyze the constituents shape and distribution after hot deformation

Chapter 4 Methodology

4.1 Material

Three different chemical compositions of AA3xxx aluminum alloys, Table 1 , were cast into three ingots with dimensions of 432x 229x 76 mm, Figure 19. The face with the dimension of 17" x 9" is parallel to the casting direction which will be the same with rolling direction in the hot rolling process.
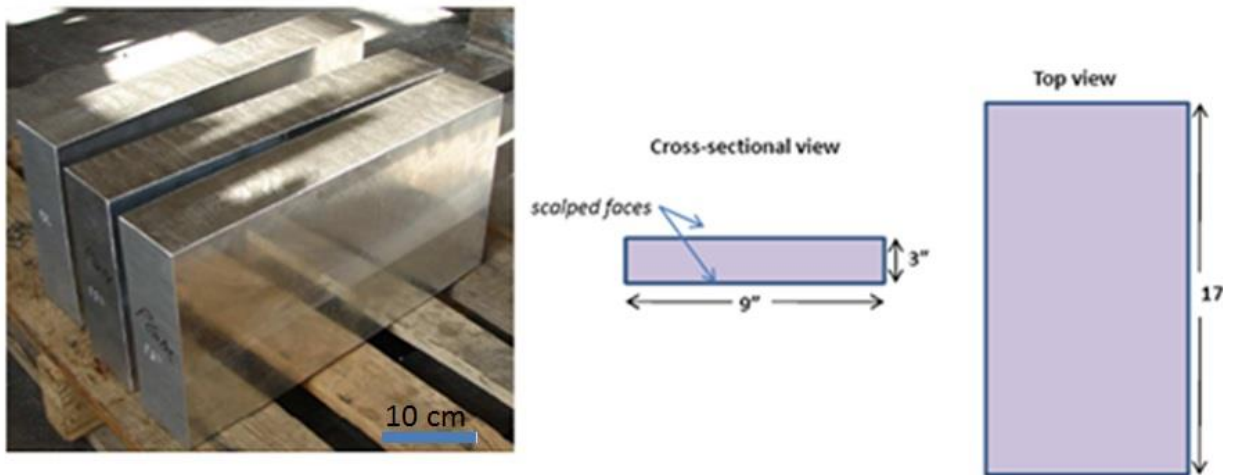
Figure 19: Three different AA3xxx aluminum alloy blocks

Table 1: Chemical composition of PGL, PGM and PGN ingots in wt%.

Ingot	Fe	Mn	Si	Ti	Al
PGL	0.36	0.05	0.15	0.009	Bal.
PGM	0.37	0.29	0.15	0.008	Bal.
PGN	0.37	1.04	0.15	0.008	Bal.

While commercial AA3103 usually contains 1 wt% Mn, 0.5% Fe and 0.05-0.20 wt% Si [46] and the maximum chemical composition limit for 3003 and 3004 aluminum alloy is 1.0-1.5 and 1.0-1.15 wt% Mn respectively, 0.6 and 0.3 wt% Si respectively and up to 0.7% Fe in both alloys [47], it is clear that the amount of Fe in these three ingots is less that typical AA3xxx aluminum alloys. Three different levels of Mn were provided in order to evaluate the effect the Mn containing dispersoids in microstructure after hot rolling of AA3xxx aluminum alloys.

4.2 Homogenization

Three different heat treatments, homogenization treatments, were applied to all three ingots. Homogenization #1, H1, is suggested by industry in which ingots are heated up from room temperature to 500℃ in 12 hours and held for 8 hours, see Figure 20. Homogenization #2, H2, is suggested by Manchester University in which ingots are heated up from room temperature to 550℃ in 12 hours and then cooled to 450℃ in the furnace which takes around 50minutes and then soaked 4 hours at 450℃, see Figure 21.
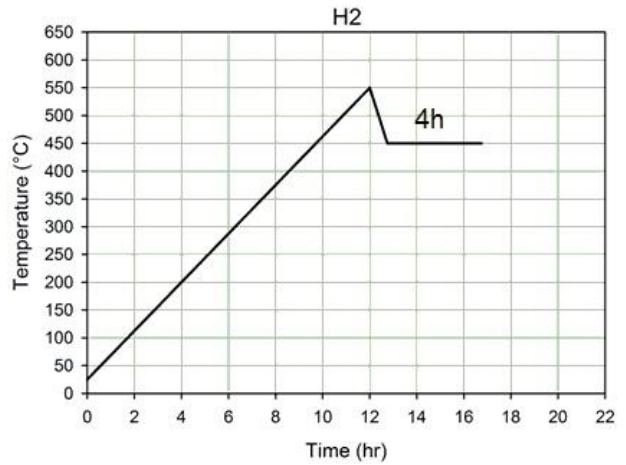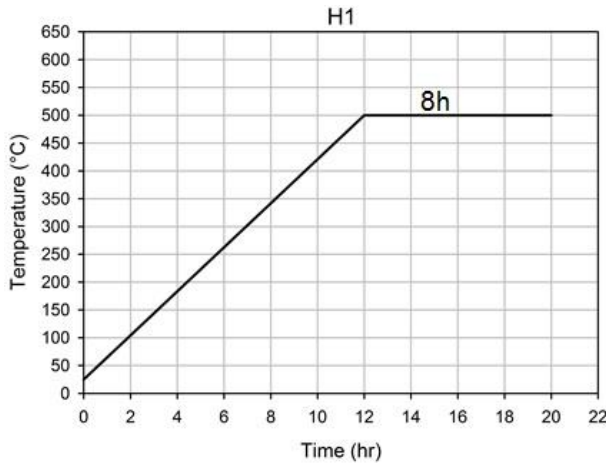
Figure 20: Time temperature curve for heat treatment 1.

Figure 21: Time temperature curve for heat treatment 2.

Homogenization #3, H3, is also suggested by Manchester University in which ingots are heated up from room temperature to 600°C in 12.8 hours and 30 minutes soak and then drop temperature to 500°C in the furnace which takes around 50 minutes and then soaked for 2 hours at 500°C, Figure 22.
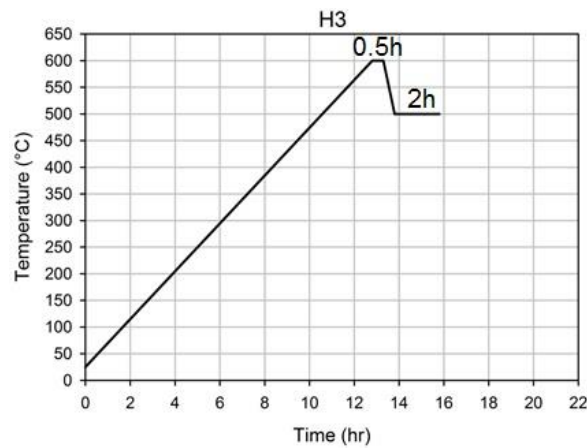
Figure 22: Time temperature curve for heat treatment 3.

4.3 Plane strain compression tests

In order to simulate the hot rolling process, PSC is applied by using the Gleeble 3500 thermo-mechanical machine at the University of Waterloo, Figure 23. The arrow indicates the plane perpendicular to the transverse direction used for metallography in order to investigate elongated grains in the direction of rolling. The sample dimensions for PSC test is 5x 10x 20 mm which are cut from heat treated ingots.

The advantage of using a Gleeble machine is its capability to heat up the sample temperature to elevated temperatures very fast and quench the sample with water or air or a mixture of these after plain strain compression deformation.
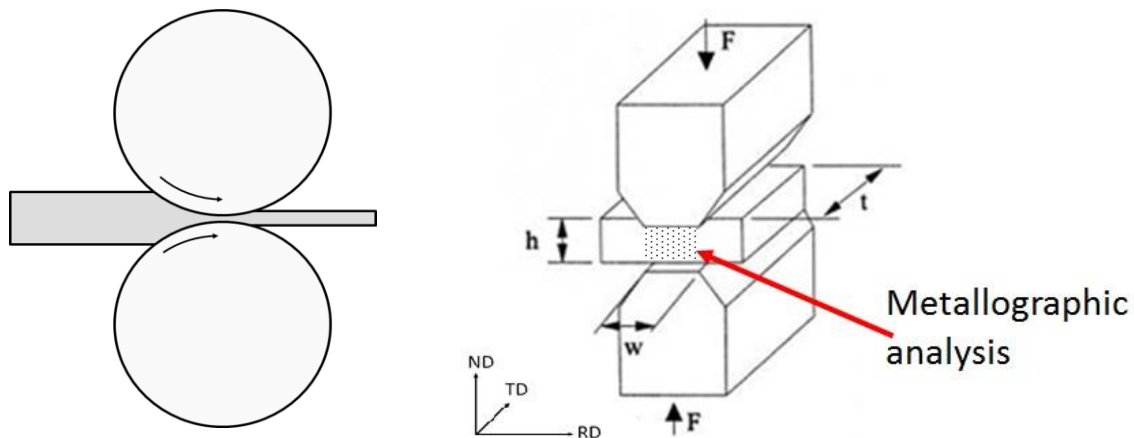
Figure 23: Rolling process and PSC test analogue to rolling

Typical time –temperature curve and time strain curve during PSC test is shown in Figure 24. The machine is set to reach desired test temperature in 80 seconds and hold the sample temperature for almost 10 seconds in order to avoid any over-shooting especially when the test temperature is high before running the PSC test. Water quenching is applied in order to

quench the sample to room temperature in order to investigate the microstructure of the sample immediately after the deformation before possible static recrystallization.

Both room temperature water and mixture of ice water have been used in order to check the quenching condition of the sample. Result shows that in both conditions the samples cool down with the same slope from 300 ℃ to 125℃ which takes around 1.5 second. After that the sample quenched with ice water cools faster than the sample quenched with room temperature water and since there is no changes in the microstructure for temperatures less than 125℃, using the room temperature water as a quench media is acceptable.

The Gleeble machine does not apply strain rate constantly during the deformation. Figure 25shows typical strain rate curve versus strain in case the strain rate is adjusted to be 0.1 for a sample heat treated with H1 and deformed at 400℃.
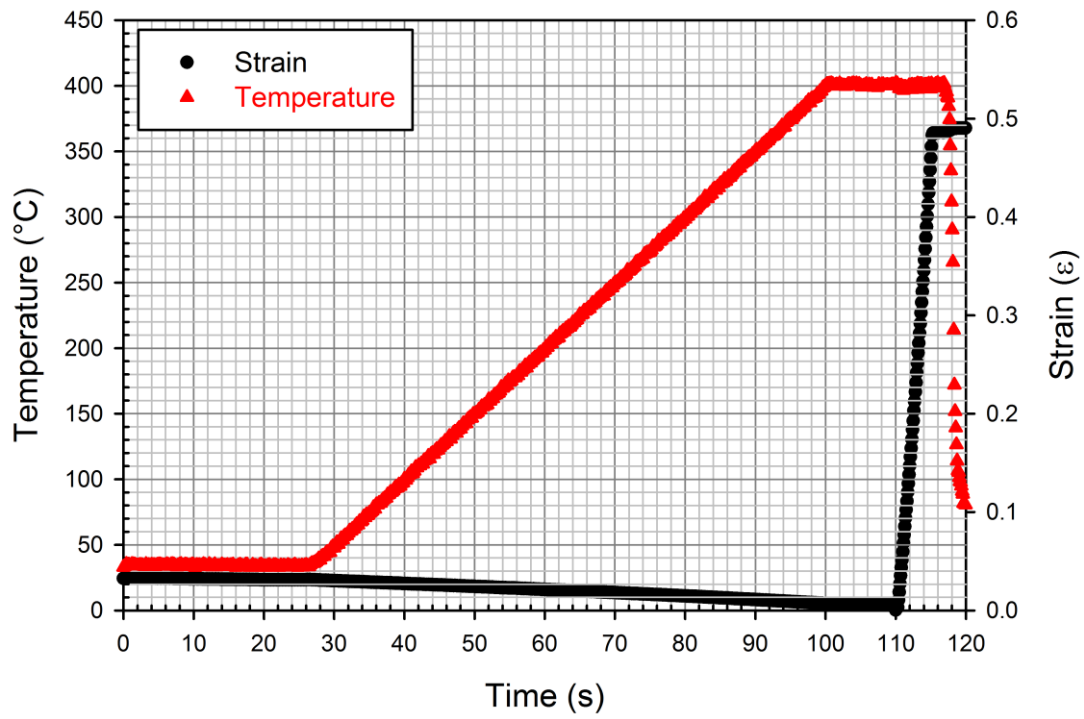
Figure 24: Time temperature curve and strain time curve before and during PSC test for PGN H3sample deformed at 400 ℃ and strain rate of 0.1.
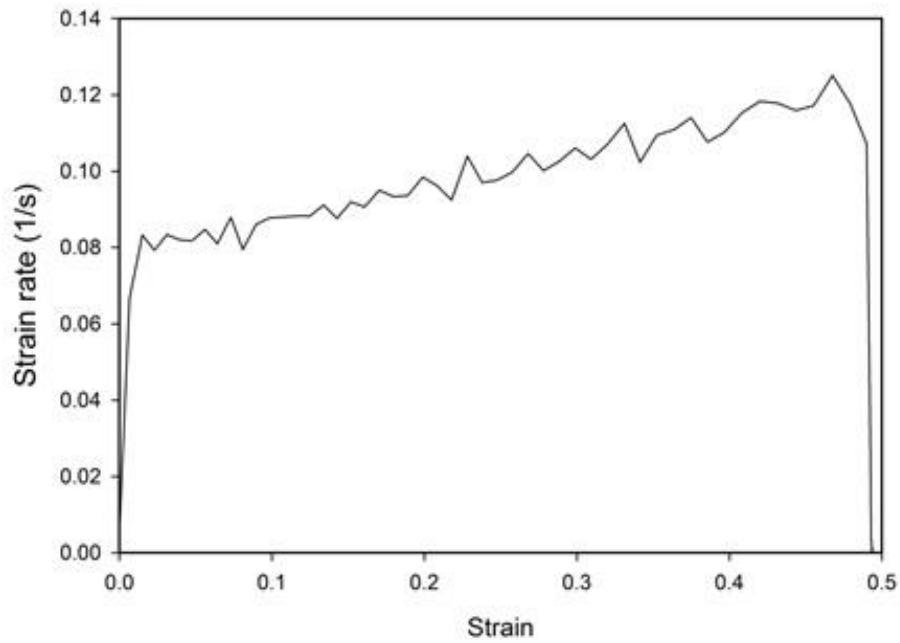
Figure 25: Strain rate versus strain curve for PGM H1 sample deformed at 400 ℃ with strain rate of $0.1s^{-1}$.

Equation 46 is used to define the average strain rate and for example the amount of average strain rate for sample in Figure 25 is $0.09909s^{-1}$ instead of $0.1s^{-1}$ however this is close enough to neglect the error.

$$\bar{\dot{\varepsilon}} = \frac{\int_{\varepsilon_1}^{\varepsilon_2} \dot{\varepsilon} \, d\varepsilon}{\varepsilon_2 - \varepsilon_1}$$

Equation 46

In order to find a flow stress from the stress strain curve of Gleeble machine, the average flow stress between a strain of 0.20 and 0.45 is calculated
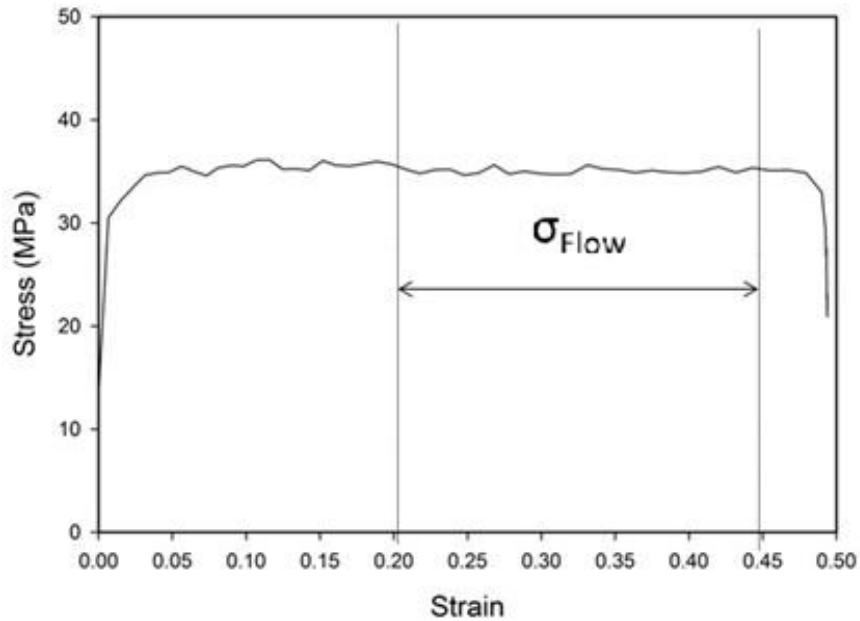
Figure 26: Calculating average flow stress from the stress-strain curve.

In order to be sure regarding the repeatability of the stress strain curves, each test condition was repeated three times and the average of three flow stress results is presented in result section.

4.4 Hot deformation constitutive model

Sellars-Tegart flow stress model is applied in which α=0.052 MPa [24] and Q= 165(KJ/Mol^{-1}).

$$\dot{\varepsilon} \exp\left(\frac{Q}{RT}\right) = A\left[\sinh(\alpha\sigma)\right]^n \qquad \text{Equation 47}$$

The A and n values are unknown values.

4.5 Stored energy and dislocation density after deformation

Two simple equations are used to calculate the stored energy E_d and dislocation density ρ immediately after deformation. C_1 and C_2 are assumed content and equal to 0.5.

$$\rho = \left(\frac{\sigma}{C_1 \mu b}\right)^2$$

Equation 48

$$P_D = c_2 \rho \mu b^2$$

Equation 49

4.6 Electrical conductivity

Electrical conductivity is reciprocal of electrical resistivity and it is commonly represented by К (kappa). Matthiessen's law shows the relationship between the chemical composition of the alloy and electrical resistivity:

$$\rho = \rho_{pure}(T) + \sum \rho_i C_i$$

Equation 50

Where $\rho_{pure}(T)$ is the electrical resistivity of pure matrix metal which is a function of temperature, ρ_i is the specific electrical resistivity of component i in solid solution and C_i is the concentration of the component i in solid solution [48, 49].

Table 2 shows the amount of the specific electrical resistivity of the solute in aluminum alloys [50].

Table 2: electrical resistivity of pure alloying elements present in material.

Solute	Mg	Si	Cu	Zn	Fe	Mn	Zr	Ti
$\Delta\rho$(nΩm/wt pct)	6.11	6.68	3.32	1.01	38.00	31.43	18.48	31.92

It is clear that the amount of Fe and Mn in solid solution have the strongest effect on the electrical resistivity compare other alloying elements. Fe has very low solid solubility in Al, so most of Fe forms constitute particles during solidification and Mn forms supersaturated solid solution. Tracking of the electrical resistivity during process chain, the formation of Mn containing dispersoids or dissolution of these dispersoids can be evaluated.

Altenpohl and Tromberg used another formula which has lots of similarity with the values in Table 2.

$$\rho = 0.0267 + 0.032Fe_{ss}\% + 0.033Mn_{ss}\% + 0.0068si_{ss}\% + 0.0032Cu_{ss} \qquad \text{Equation 51}$$

Chapter 5 Results and Discussion

5.1 Metallography

5.1.1 As-cast and homogenized metallography

As cast metallography of three PGL, PGM and PGN alloy are shown in Figure 27, Figure 28, and Figure 29 on a plane perpendicular to transverse direction, Figure 23.

Increasing Mn content from 0.05 to 0.29 and finally 10.4 wt% leads the formation of higher constituent particles from 4.75 to 7.64 to 11.14 area fraction, which are the dark lines in micrographs. In order to observe constituents particles, samples should be ground with 400 and 600 grit SiC papers; in addition, polishing of the samples with 15µm diamond spray for 5 minutes and 8µm diamond spray for 3 minutes are applied. Final stage is polishing the sample with colloidal silica in a vibratory polisher for almost 2hours.
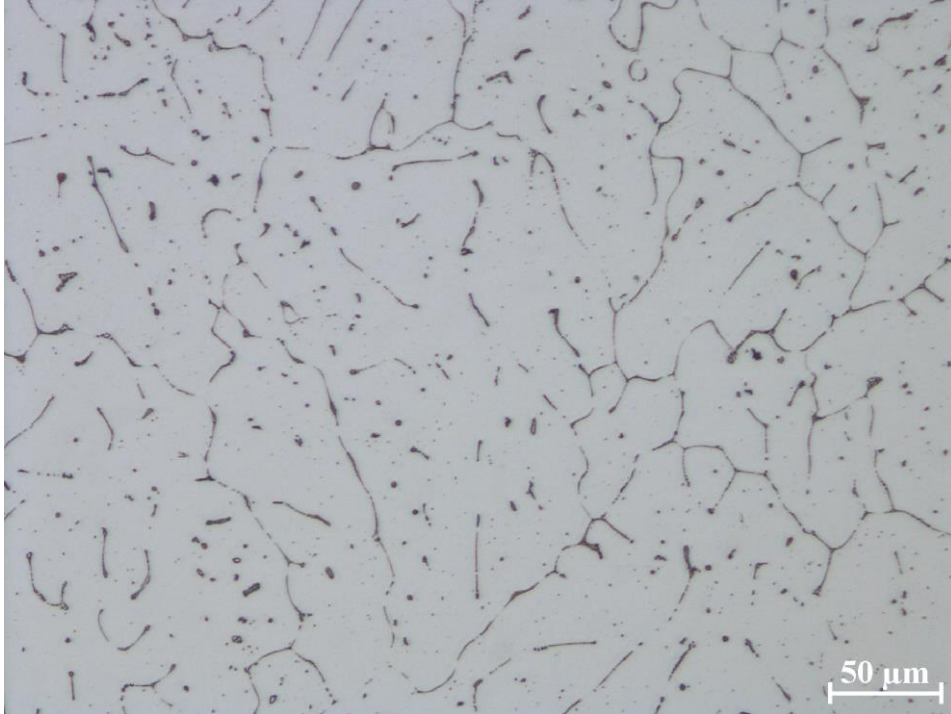
Figure 27: As cast metallography of PGL alloy
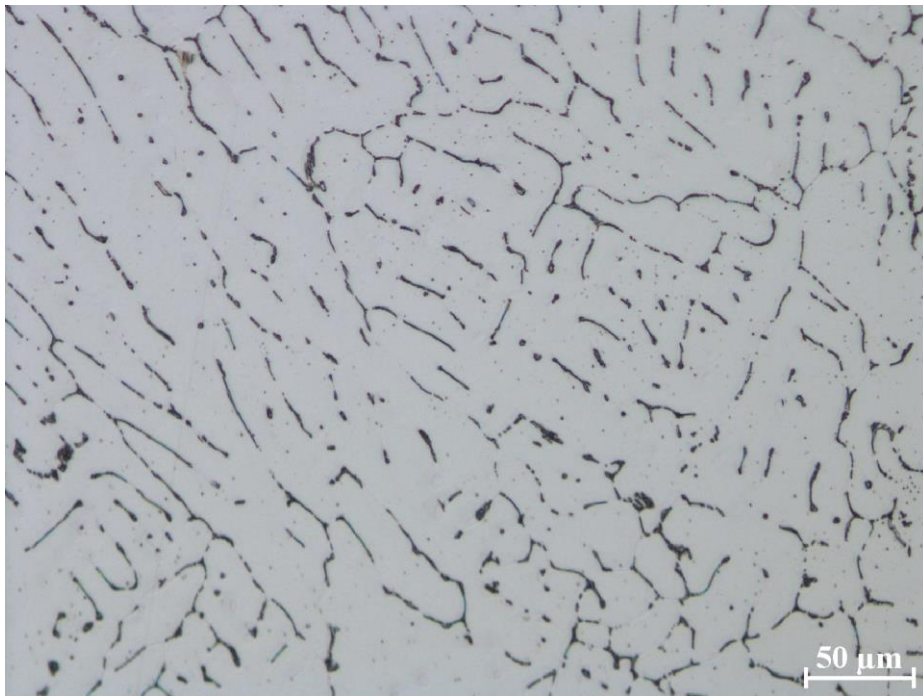
Figure 28: As cast metallography of PGM alloy
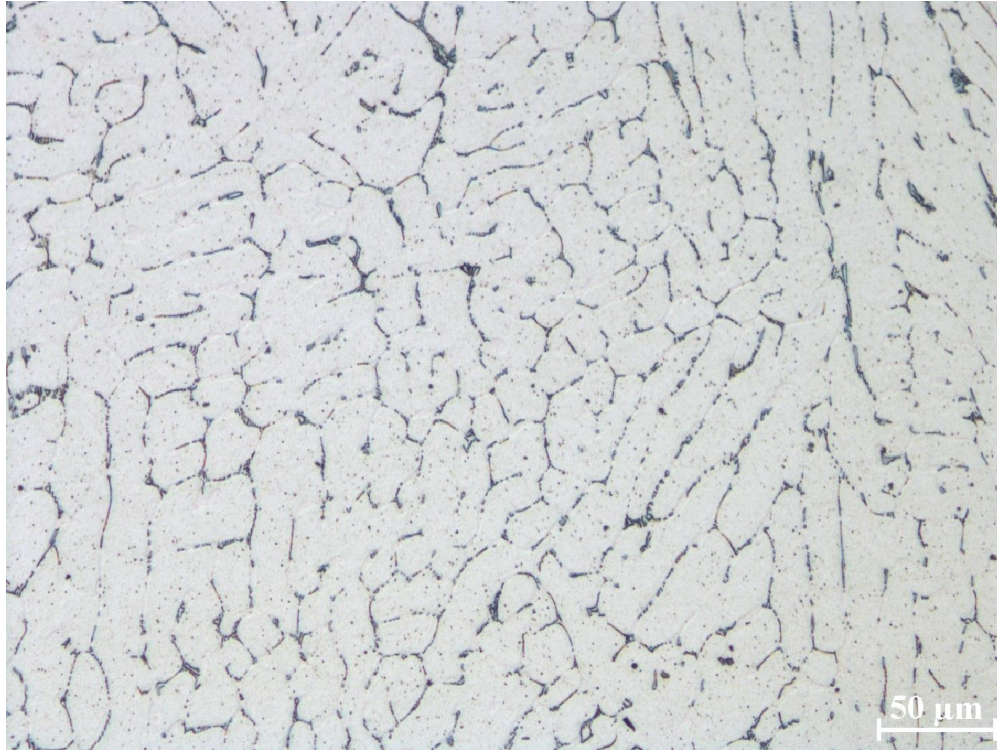
Figure 29: As cast metallography of PGN alloy

Different homogenization treatments leads segmentation of these particles, Figure 30 and Figure 31, due to higher thermal expansion of the aluminum matrix compare to constitution particles which apply a tensile strength on these particles.

Figure 30: As-polished PGN sample after homogenization schedule H3
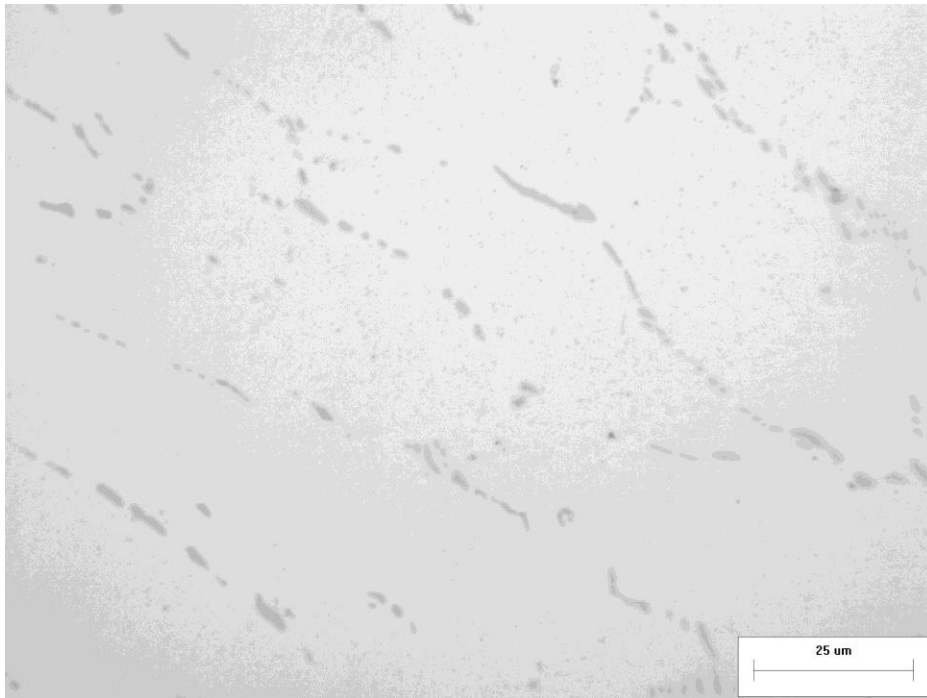
Figure 31: As-polished PGN sample after homogenization schedule H3at higher magnification

In order to observe dispersoid particles in microstructure, the as-polished sample sinks in 2.5 %HBF4 for 60 seconds. After rinsing properly for some seconds, 50% HNO3 is

used for 10 seconds and sample is rinsed properly. Fine dispersed particles are obvious in micrographs, see Figure 32 and Figure 33.
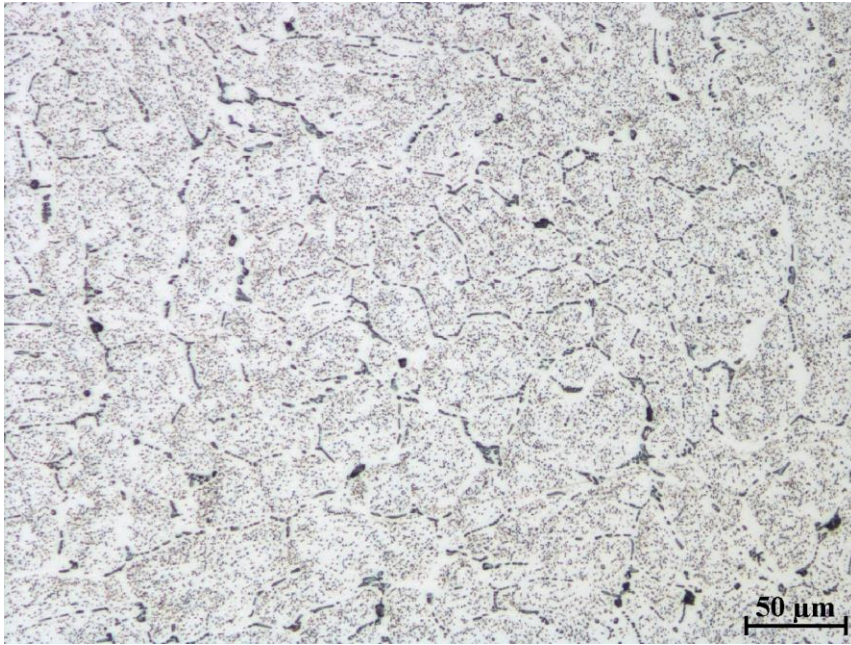
Figure 32: Etched PGN sample after H3
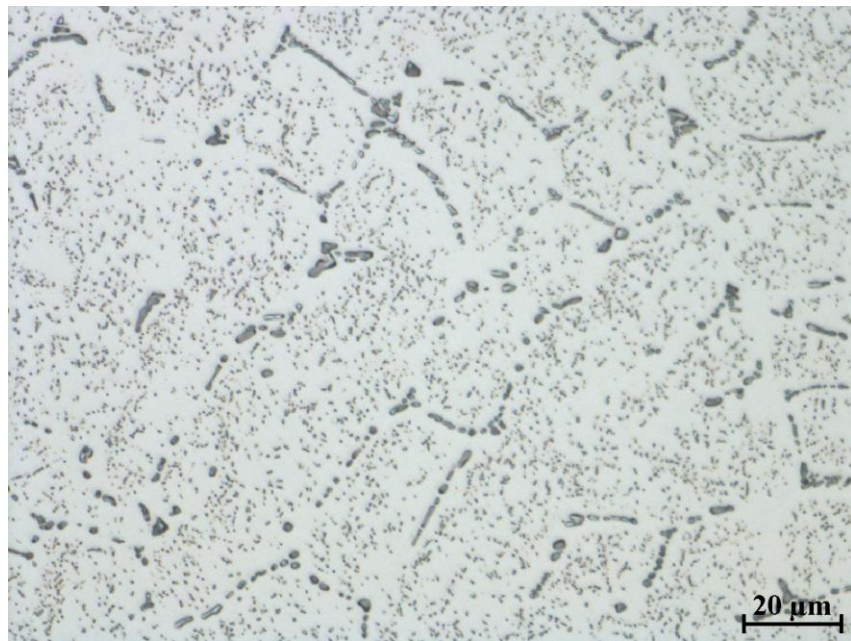
Figure 33: Etched PGN sample after H3with higher magnification.

5.1.1 Hot deformed metallography

Constituent particles tend to align with rolling direction after hot deformation. Figure 34 and Figure 35 show this alignment for the same PGM sample deformed at 300 ℃ with a strain rate of $10s^{-1}$ to a strain of 0.5 at two different magnifications while the rolling direction oriented horizontally.
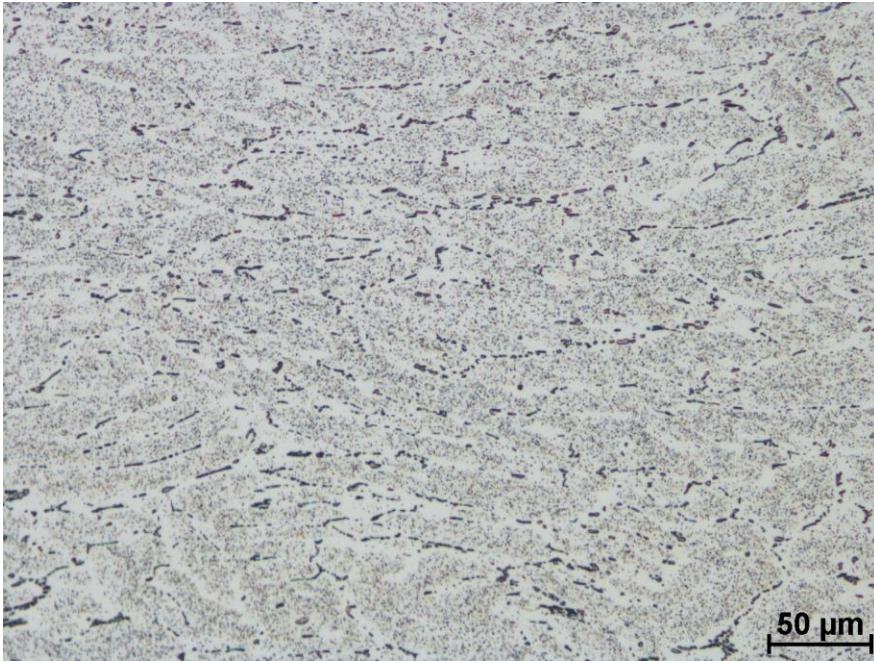
Figure 34: Etched PGM sample deformed at 300 ℃ and strain rate of 10 up to strain 0.5 heat treated with H3.

54
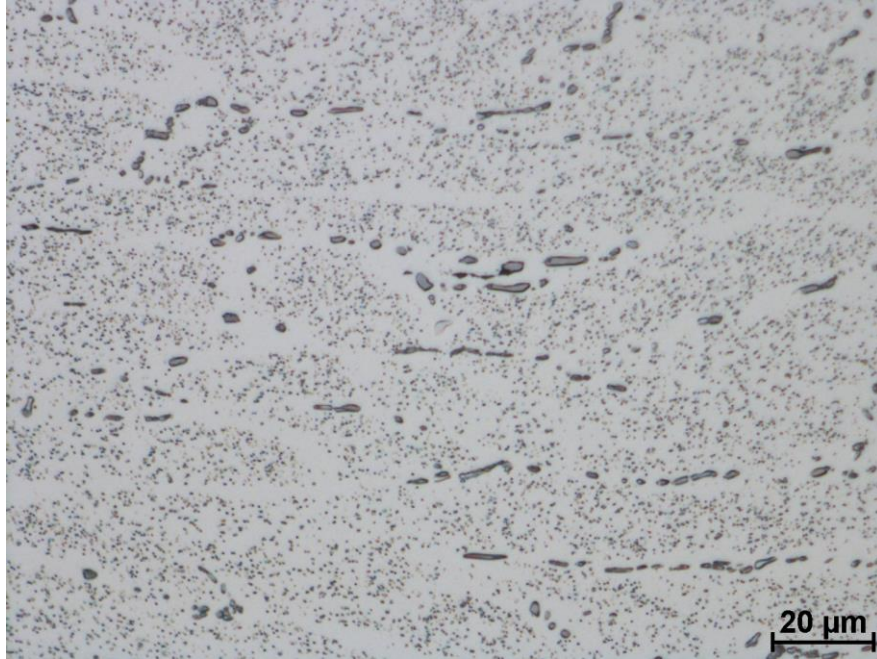
Figure 35: Etched PGM sample deformed at 300 ℃ and strain rate of 10 up to strain 0.5 heat treated with H3 with higher magnification.

In order to reveal the grain structure, etched sample is polished again for 5 minutes with colloidal silica. Barker etch is used to reveal grain structure, Figure 36. In order to avoid error due to friction between anvils and sample, dead zone of the deformation, and temperature gradients within thickness of the sample, only centerline of sample with the approximate thickness of 1 mm is used for like metallography. The dead zone area is relatively large since no lubrication is used between the PSC sample and anvil. The grains in the right or left side of the Figure 36 shows the PGM sample grains which are homogenized with H1. The average grain size is approximately 200 µm.
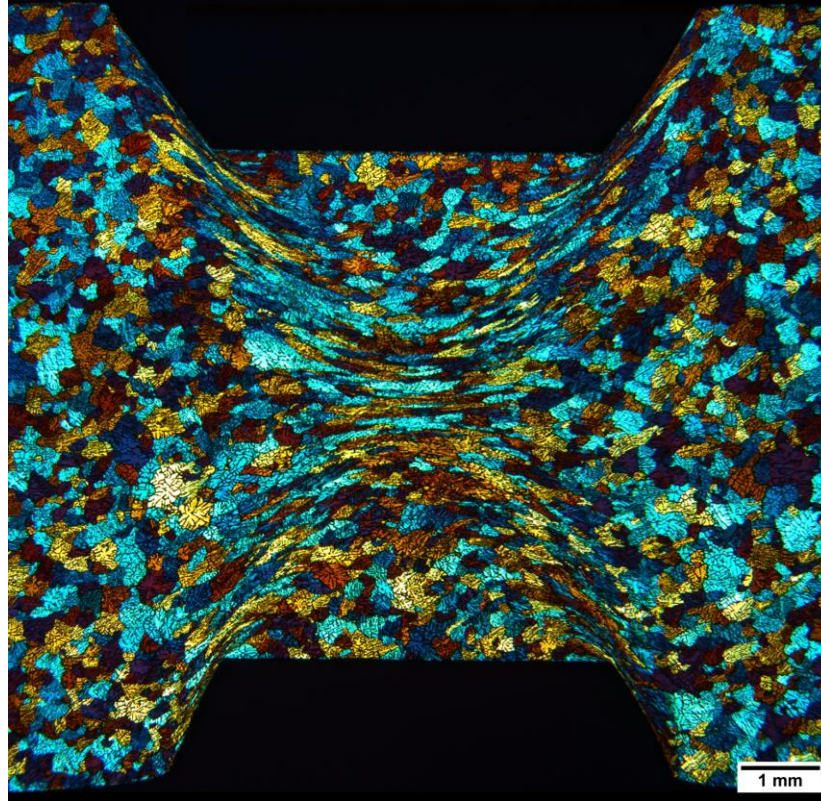
Figure 36: PSC sample grain orientation for a sample deformed at 500 ℃ and strain rate of 0.1 up to strain 0.5 heat treated with H1 and water quenched immediately after deformation for PGM alloy.
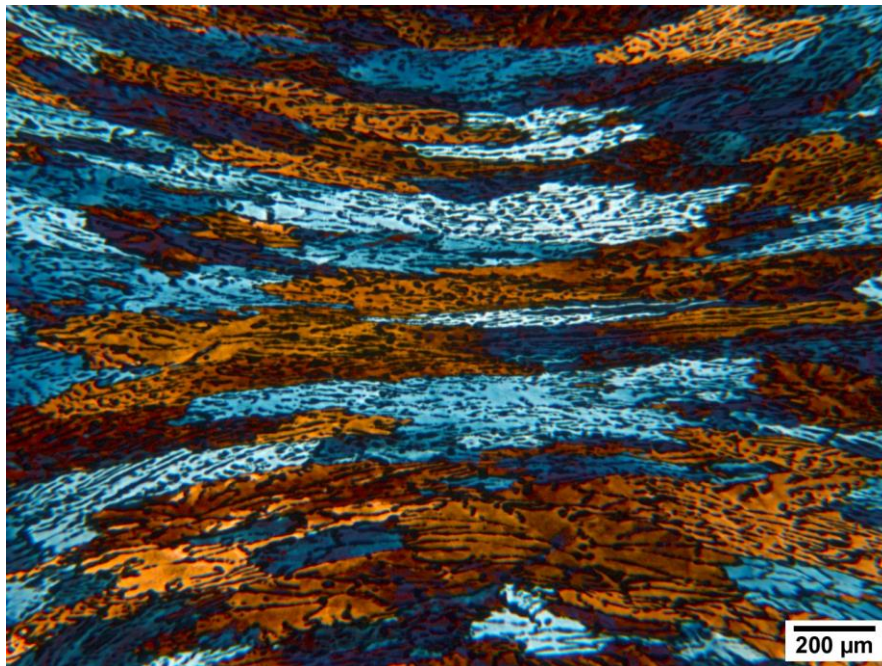
Figure 37: center section for the sample shown in Figure 36 heat treated with H1.

Since higher stored energy formed in case of strain rate of 10 and lower PSC temperature of the 300 ℃, It was predicted that it is probable that stored energy be sufficient to have a static recrystallization during annealing in this condition. Homogenization treatments of H1 and deformed condition described above and annealing temperatures at 500 ℃ and 550 ℃ are the most desired and potential conditions to form recrystallized grains. Higher annealing temperature of 500 ℃ was selected and samples annealed for 6 hours for PGL. Figure 38 shows the PGL sample grain structure is recrystallized after 6 hours and no pancake grains can be observed anymore. Obviously, in the case of the sample homogenized with schedule H3 more formation of dispersoids is predictable than H1. Micrograph in Figure 39 shows in case of the applying H3 heat treatment, still the PGL sample recrystallized in described hot deformation and annealing temperature.
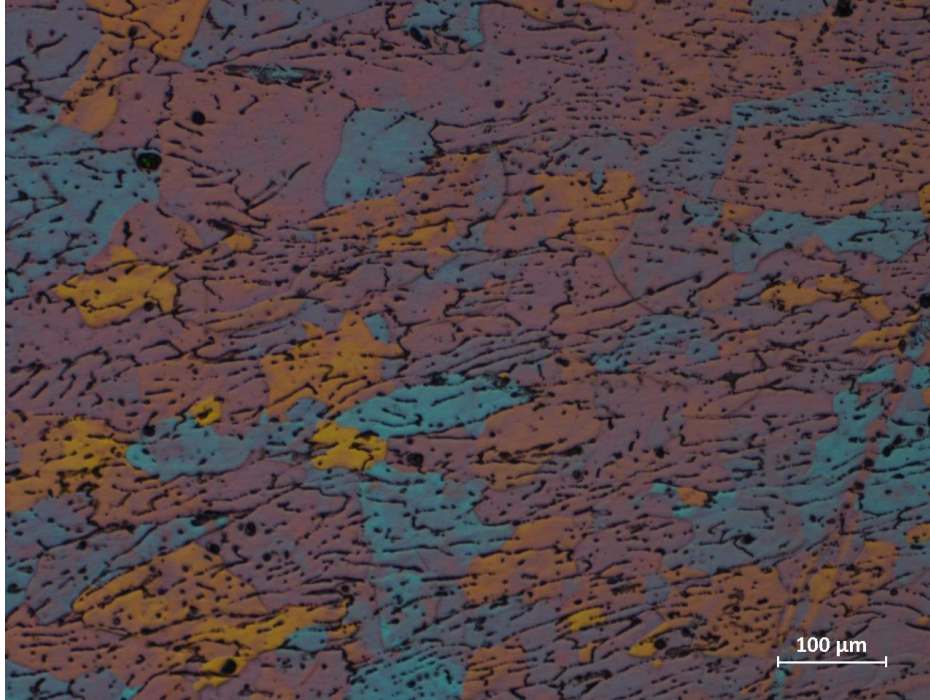
Figure 38: PSC sample grain structure for a PGL sample deformed at 300 ℃ and strain rate of 10 up to a strain of 0.5, heat treated with schedule H1 and annealed at 500 ℃ for 6 hours.
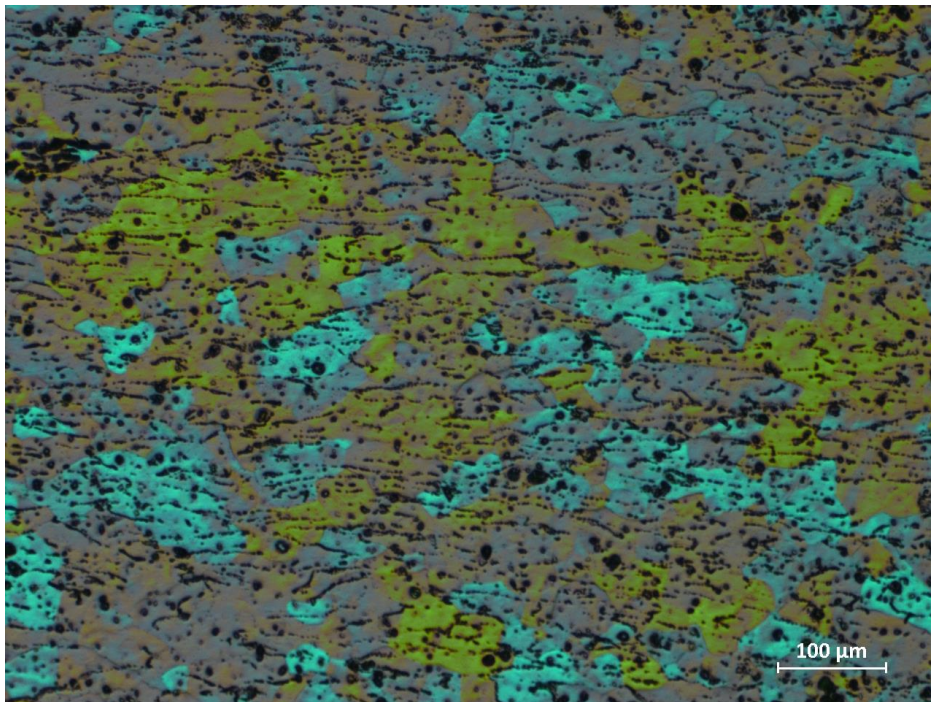
Figure 39: PSC sample grain structure for a PGL sample deformed at 300 ℃ and strain rate of 10 up to a strain of 0.5, heat treated with schedule H3 and annealed at 500℃ for 6 hours.

Figure 41 shows that even holding the PGN sample for 12 hours at an annealing temperature of 500 ℃ does not reveal any recrystallized grains, and pancake grains resulting from the PSC test are still visible. Figure 40 reveals that no recrystallized grains are observed even after increasing the annealing temperature to 550 ℃ for an annealing time of 2 hours for the same deformation condition with sample shown in Figure 41. If the same PSC hot deformation condition is applied for H3 heat treated sample, no recrystallized grains should be observed, Figure 43.

According to micrographs in Figure 41 and Figure 42, it can be concluded that no recrystallization grains are possible in any hot deformations and annealing conditions for PGN samples.
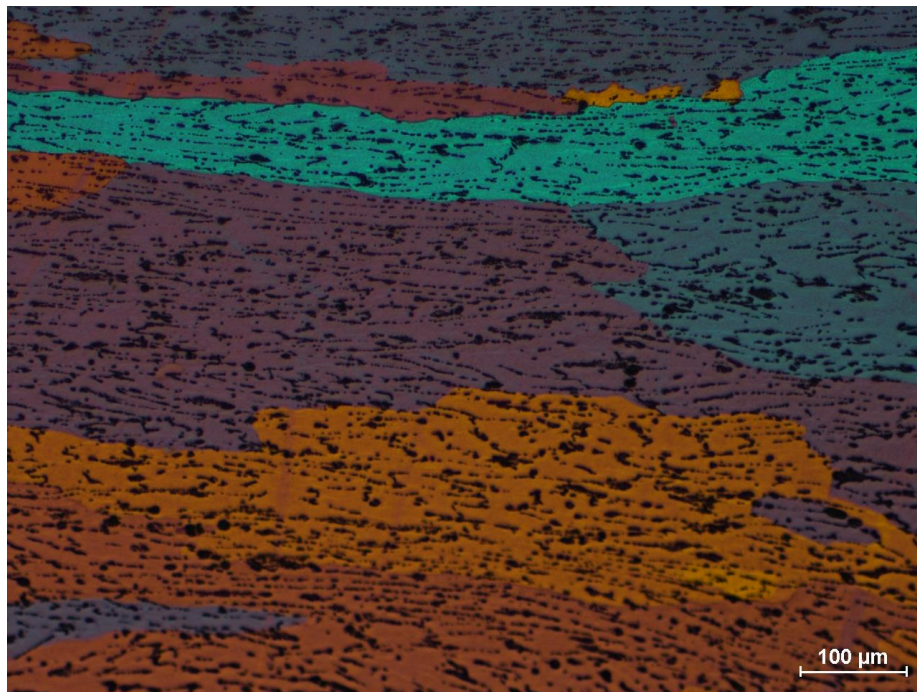
Figure 41: PSC sample grain structure for a PGN sample deformed at 300 ℃ and strain rate of 10 up to a strain of 0.5, heat treated with schedule H1 and annealed at 500 ℃ for 12 hours.
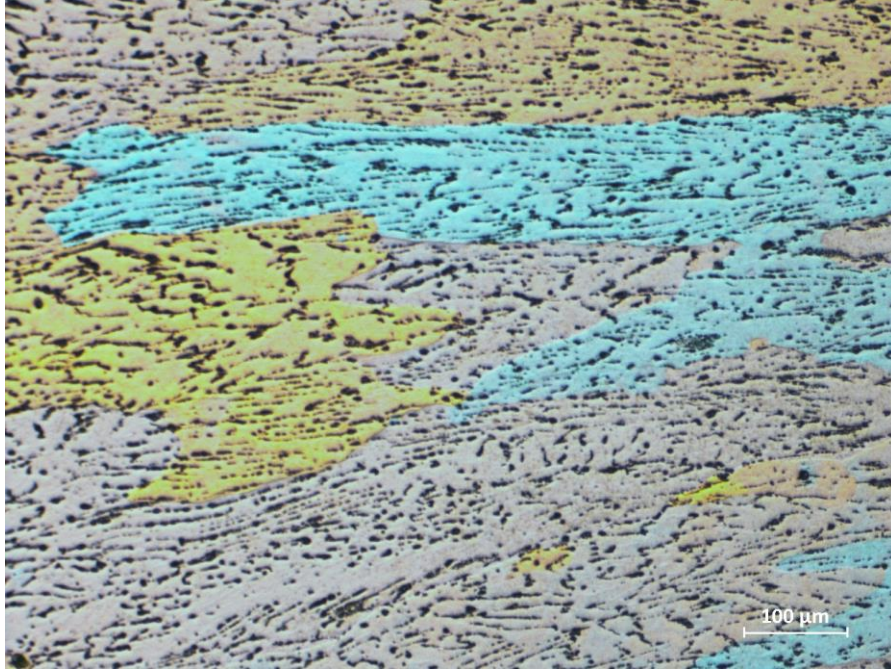
Figure 42: PSC sample grain structure for a PGN sample deformed at 300 ℃ and strain rate of 10 up to a strain of 0.5, heat treated with schedule H1 and annealed at 550 ℃ for 2 hours.
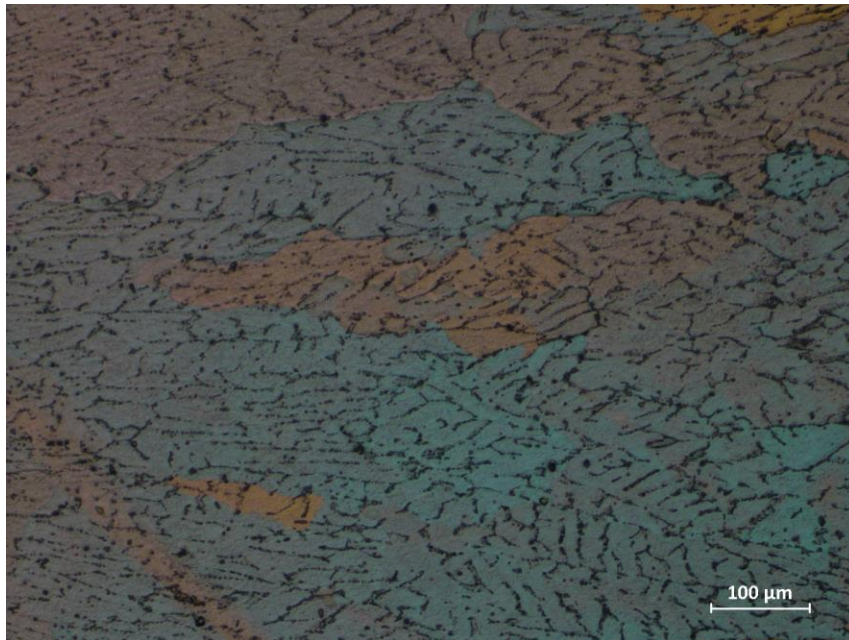
Figure 43: PSC sample grain structure for a PGN sample deformed at 300 ℃ and strain rate of 10 up to a strain of 0.5, heat treated with schedule H3 and annealed at 550 ℃ for 2 hours.

Extensive metallography for various deformation conditions and annealing temperatures and annealing times has been done. A summary of the results are listed in Table 3 and Table 4. An example micrograph of each condition is given in Appendix A.

Table 3: Metallography investigations for different hot deformation conditions for PGL alloy.

	SR	Deformation Temp	Heat treatment	Annealing Temp	Annealing time (hr)	Formation of REX grains	Comment
PGL	10	300	H1	500	6	Confirmed	
PGL	10	300	H1	500	12		Over etched
PGL	10	300	H3	500	6	Confirmed	
PGL	10	300	H3	500	12	Confirmed	
PGL	10	500	H1	500	6	Minor	
PGL	10	500	H1	500	12	More significant	
PGL	10	500	H3	500	6	None	
PGL	10	500	H3	500	12	Confirmed	

Table 4: Metallography investigations for different hot deformation conditions for PGN alloy.

	SR	Deformation Temp	Heat treatment	Annealing Temp	Annealing time (hr)	Formation of REX grains	Comment
PGN	10	300	H1	550	2	None	
PGN	10	300	H1	550	6	None	
PGN	10	300	H3	550	2	None	
PGN	10	300	H3	550	6		Over etched
PGN	10	300	H1	500	6		Over etched
PGN	10	300	H1	500	12	None	
PGN	10	500	H1	500	6	None	
PGN	10	500	H1	500	12		Over etched
PGN	10	300	H3	500	6	None	
PGN	10	300	H3	500	12	None	
PGN	10	500	H3	500	6	None	
PGN	10	500	H3	500	12	None	

5.1 Electrical conductivity measurements

Electrical conductivity, the reciprocal of electrical resistivity, was determined for 5 samples and the average values for as-cast and homogenized samples are summarized in Table 5. According to Equation 51 and Table 1 in which the amount of Fe is almost constant in the all three alloys, any deviation in electrical conductivity is the result of amount of Mn in solid solution. By comparison of the electrical conductivity in as-cast conditions for PGL, PGM, and PGN alloys, lower electrical conductivity in the PGN as-cast condition shows higher Mn in the aluminum matrix in case of a solid solution. Vice versa, PGL as-cast alloy has the lowest Mn content in solid solution.

Any homogenization treatment leads the formation of the dispersoids by migration of the Mn from solid solution to form dispersoid particles. Consequently, in all three alloys, the electrical conductivity increases after any homogenization treatment. Due to existence of the high super saturated Mn in solid solution in case of the PGN as-cast, applying a homogenization treatment in this alloy promotes a large amount of dispersoid formation and leads an increase in electrical conductivity by almost 30 percent. The difference between electrical conductivity with different homogenizations for a specific alloy is not remarkable.

Table 5: Electrical conductivity for PGL, PGM, and PGN alloys in as-cast and homogenized conditions %IACS

Alloy	Sample 1 %IACS	Sample 2 %IACS	Sample 3 %IACS	Sample 4 %IACS	Sample 5 %IACS	Average %IACS
PGL- As cast	55.36	55.52	55.14	55.71	55.55	55.46
PGL-H1	58.02	58.07	57.84	57.64	57.94	57.90
PGL-H2	58.41	58.16	58.34	58.15	58.27	58.27
PGL-H3	58.28	58.23	58.08	58.12	58.39	58.22
PGM- As cast	45.25	45.38	45.06	45.41	45.4	45.30
PGM-H1	50.17	50.53	50.29	50.15	50.21	50.27
PGM-H2	50.53	50.64	50.52	50.91	50.81	50.68
PGM-H3	X	X	X	X	X	X
PGN- As cast	30.07	30.1	29.94	29.97	29.84	29.98
PGN-H1	40.94	40.65	40.69	40.49	40.88	40.73
PGN-H2	42.09	42.09	41.22	41.85	41.58	41.77
PGN-H3	40.51	40.25	40.65	40.56	40.26	40.45

5.2 Flow stress experiment results

The method described in Figure 26 is used to calculate the flow stress for PGN alloy for strain rates of 0.1 and 10 for all three heat treatments of H1, H2, H3 and temperatures of 300, 400, 500 ℃, Table 6. Flow stress for PGM alloy is also calculated for H1and H2 and for the same temperatures and strain rates of 0.1and 10, Table 7.

For PGN and PGM alloys, flow stress for the same temperature and strain rate is almost the same or slightly lower for PSC samples heat treated in H2 comparing to H1.The PSC sample heat treated in H3 shows minimum flow stress in PGN alloy among all heat treatments.

In each heat treatment, flow stress decreases with increasing of temperature. Moreover, if the temperature is constant, increasing of the strain rate leads to an increase in the flow stress.

Table 6: σ_{flow} (MPa) at strain rate of 0.1and 10 for PGN alloy

			H1	H2	H3
	Strain rate (s^{-1})	Temperature (℃)	σ_{flow} (MPa)	σ_{flow} (MPa)	σ_{flow} (MPa)
PGN	0.1	300	75.49	74.26	70.06
		400	45.53	45.61	39.51
		500	29.77	30.95	24.50
	10	300	101.59	101.40	97.00
		400	72.84	69.94	66.96
		500	47.97	47.13	42.93

PGN alloy PSC sample, containing more Mn content, shows higher flow stress value for the same temperature and strain rate and heat treatment than PGM alloy PSC sample, containing lower Mn content.

Table 7: σ_{flow} (MPa) at strain rate of 0.1and 10 for PGM alloy

			H1	H2
	Strain rate (s^{-1})	Temperature (℃)	σ_{flow} (MPa)	σ_{flow} (MPa)
PGM	0.1	300	60.65	57.84
		400	34.90	33.68
		500	21.69	20.58
	10	300	87.09	84.42
		400	59.69	57.19
		500	37.76	36.69

5.3 Hot deformation constitutive model results

The values of unknown parameters of A and n for PGN and PGM alloy are calculated and shown in Table 8. The results of the experiments heat treated in H1 and H3 and strain rates of 0.1 and 10 and three different temperatures of 300,400,500 ℃ have been used in this calculation. In case of the PGM alloy, the results of the experiments with the same strain rates and temperatures heat treated in H1 and H2 are used to calculate of the A and n value.

Table 8: Sellers-Tegrat Model constants for PGN and PGM alloy

PGN			PGM		
	n	A		n	A
H1	3.47	1.54×10^9	H1	3.77	7.89×10^9
H3	3.42	4.70×10^9	H2	3.88	9.59×10^9

Comparison of the flow stress between Sellars-Tegart model and experiment for PGN alloy and PGM alloy are shown in Figure 44 and Figure 45 and respectively. Dash lines show the deviation of 10% between the measured value from experiment and calculated value from model.

The highest deviation of about 10% was found between the prediction flow stress value of the model and flow stress obtained from the PSC test for samples with a strain rates of 0.1 and temperature of 500 ℃ when comparing PGN and PGM alloys.
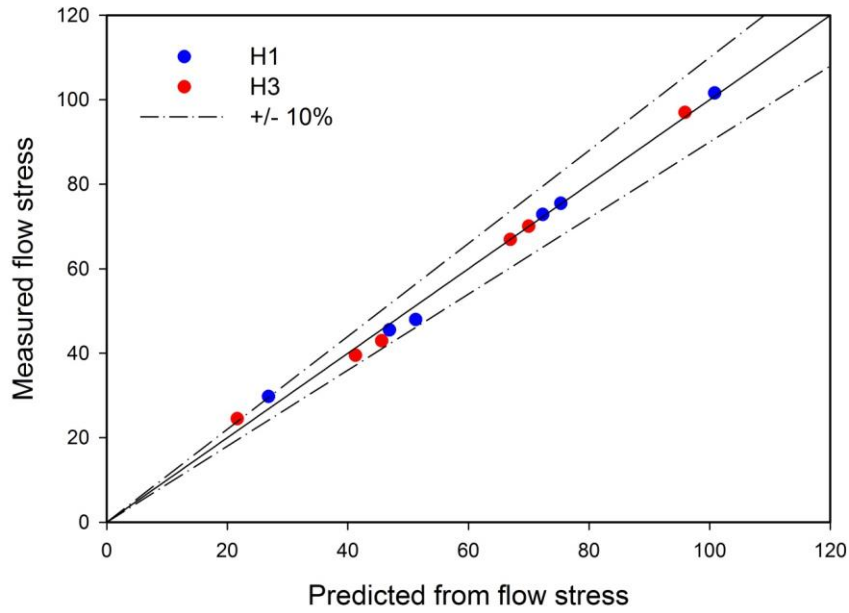
Figure 44: Comparison of the flow stress between Sellars-Tegart model and experiment for PGN alloy
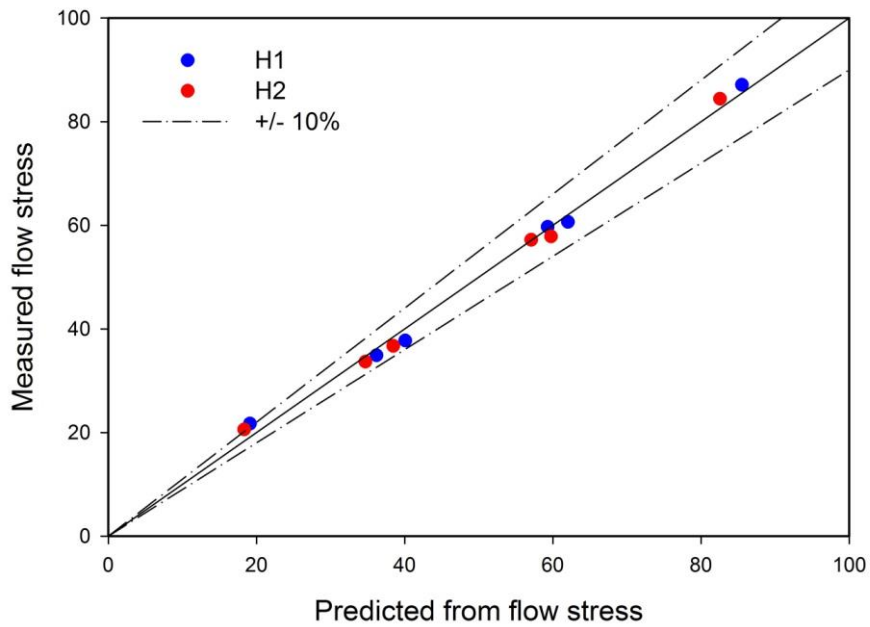
Figure 45: Comparison of the flow stress between Sellars-Tegart model PGM alloy

5.4 Stored Energy and Dislocation density after deformation

The result of stored energy E_d and dislocation density ρ after deformation is shown in Table 9 and Table 10 for PGN and PGM alloy.

Table 9: Stored energy and dislocation density for PGN alloy in different experiments conditions

			H1		H2		H3	
	Strain rate (s^{-1})	Temperature (°C)	ρ $\times 10^{14}$	E_D (MJm^{-3})	ρ	E_D (MJm^{-3})	ρ $\times 10^{14}$	E_D (MJm^{-3})
PGN	0.1	300	5.73	0.53	5.54E+14	0.51	4.93	0.45
		400	2.36	0.20	2.36E+14	0.20	1.77	0.15
		500	1.15	0.09	1.24E+14	0.10	0.78	0.06
	10	300	10.40	0.95	1.03E+15	0.95	9.46	0.87
		400	6.03	0.52	5.56E+14	0.48	5.09	0.44
		500	2.98	0.24	2.88E+14	0.23	2.39	0.19

Table 10: Stored energy and dislocation density for PGM alloy in different experiments conditions

	Strain rate (s^{-1})	Temperature (°C)	H1		H2	
			ρ x10^{14}	E_D (MJm^{-3})	ρ x10^{14}	E_D (MJm^{-3})
PGM	0.1	300	3.70	0.34	3.36	0.31
		400	1.38	0.12	1.29	0.11
		500	0.61	0.05	0.54	0.04
	10	300	7.62	0.70	7.16	0.66
		400	4.05	0.35	3.72	0.32
		500	1.85	0.15	2.04	0.17

In the case of PGN alloy, when strain rate is constant, increasing of the temperature leads decreasing of the dislocation density, Figure 46 (a), and stored energy, Figure 46 (a), For all H1 and H2 and H3. Increasing the strain rate in the same test temperature significantly increases the dislocation density and stored energy. Due to the fact that different heat treat treatments influence the microstructure differently, in the case of the same PSC test conditions, H1 exhibits the highest dislocation density and stored energy after deformation and H3 shows the lowest values. PGM alloy follow the same trend already described for PGN alloy and the results for dislocation density and stored energy are shown in Figure 46 (b) and Figure 46 (d) respectively.

By comparing the dislocation density or stored energy for PSC sample with PGN chemical composition and PSC sample with PGM chemical composition, it is obvious that the PGN sample shows higher dislocation density and stored energy than PGM sample.
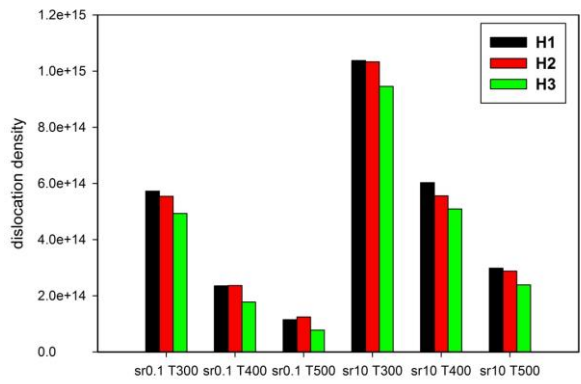
(a)
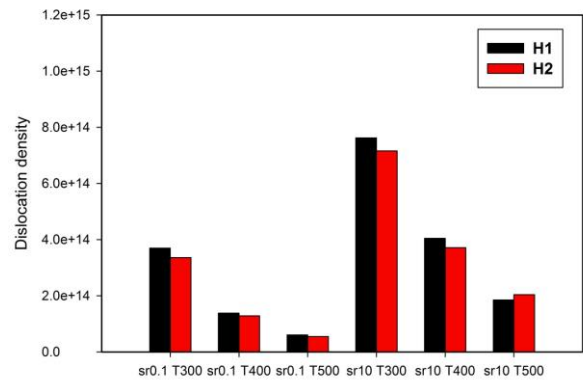
(b)
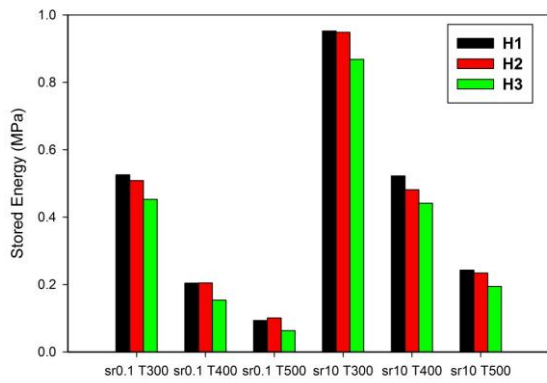
(c)
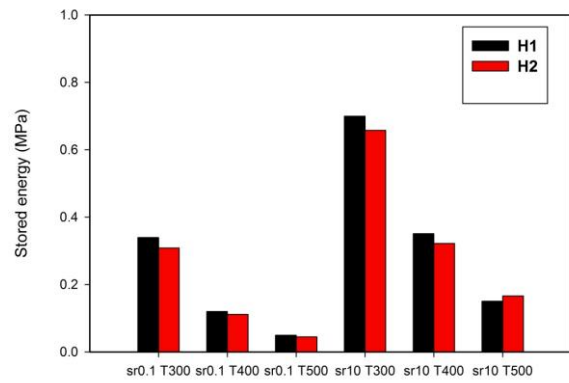
(d)

Figure 46: (a) Predicted dislocation density after deformation for PGN in different experiments conditions, (b) Predicted dislocation density after deformation for PGM in different experiments conditions, (c): Stored energy after deformation for PGN in different experiments conditions, (d) Stored energy after deformation for PGM in different experiments conditions.

5.5 Recovery model during annealing process

Metallography proved that there was no recrystallization happened during annealing in PGN alloy. In contrast, PGL alloy shows recrystallized grains in some deformation conditions and some annealing temperatures and annealing times.

Experimental results from Lens. et al., shown in Figure 16, helped to identify recovery modeling parameters for Al-1% Mn which is close to chemical composition of PGL alloy. U_0 is activation energy and v is activation volumes are only two unknowns that can find by fitting the Equation 29 to experimental data. M_{Taylor} is equal to 3.1 for isotropic FCC materials [51] and α is 0.24 [42].

$$\frac{d\tilde{\sigma}}{dt} = -E\frac{\tilde{\sigma}^2}{M_{Taylor}^3\alpha^2\eta^2}v_D\exp(-\frac{U_0}{K_BT})Sinh(\frac{\tilde{\sigma}v}{K_BT})$$

Equation 52

Activation energy of 142 KJ/mole and activation volume of 22 b^3 shows a good fit to recovery model while b is the Burger's vector. This activation volume is within the range of physically accepted values of 20-50 b^3 [52]. Good fitting between the experimental data and recovery model are shown in Figure 47. for strain up to 1.3 and annealed at 220 ℃ for Al-1% Mn. Appendix B shows the comparison between model prediction and experimental data for other temperatures.
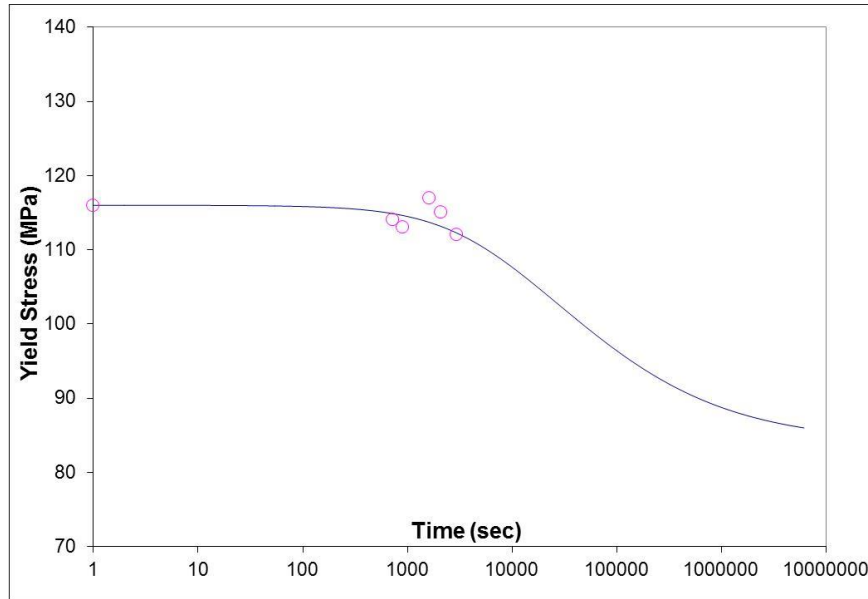
Figure 47: Comparison between experimental data and recovery model prediction for strain up to 1.3 and annealed at 220℃ for Al-1% Mn

5.1 Image analysis

Micrograph from the centerline of two homogenization conditions of H1 and H3 are shown in Figure 49 and Figure 50. Since the Image analysis software cannot distinguish between constituent particles and dispersoid particles, constituent particles of each micrograph is drawn on transparent paper manually, see Figure 48. Image analysis software in applied to five of modified micrographs for each condition in order to obtain better statistical condition and area distribution and shape factor for each condition is measured. The same approach is applied for PGN samples heat treated with H3 and deformed in two different temperatures of 300℃ and 500℃ for strain rates of 0.1 and 10. The number of particles for each condition is shown in Table 11and Table 12.

Figure 48: Modified micrograph in transparent paper for PGN sample heat treated in H1

Number of constituent particles after heat treatment H3 is 1226 and it is much more than the case of H1 which is 724. After hot deformation in different temperatures and strain rates when samples were heat treated with H3, number of the particles does not change significantly. Micrographs show that the sizes of the constituent particles are bigger in case of heat treated in H1 compare to H3 and area distribution histograms confirm it, see Figure 49 and Figure 50.

Figure 49: Optical micrograph of PGN alloy after homogenization of H1
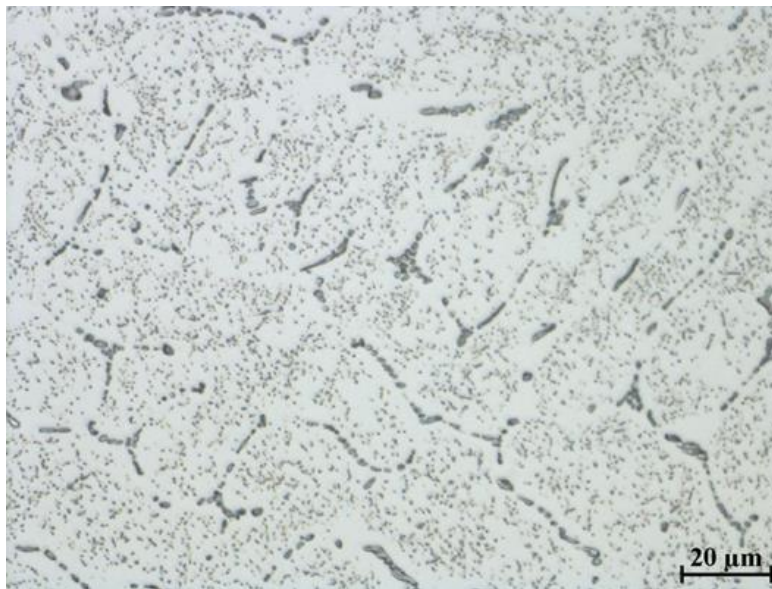
Figure 50: Optical micrograph of PGN alloy after homogenization of H3

Figure 51: Modified micrograph in transparent paper for PGN sample heat treated in H1

Table 11: Image analyzing results for PGN alloy after homogenizations H1 and H3

	Heat treatment type	Number of particles
PGN	H1	724
	H3	1226

Table 12: Image analyzing results for PGN alloy after homogenization H3 and different PSC conditions

		Deformation Temperature °C	Strain rate (s⁻¹)	Strain	Number of particles
PGN	H3	300	0.1	0.5	1205
			10	0.5	1274
		500	0.1	0.5	1356
			10	0.5	1186
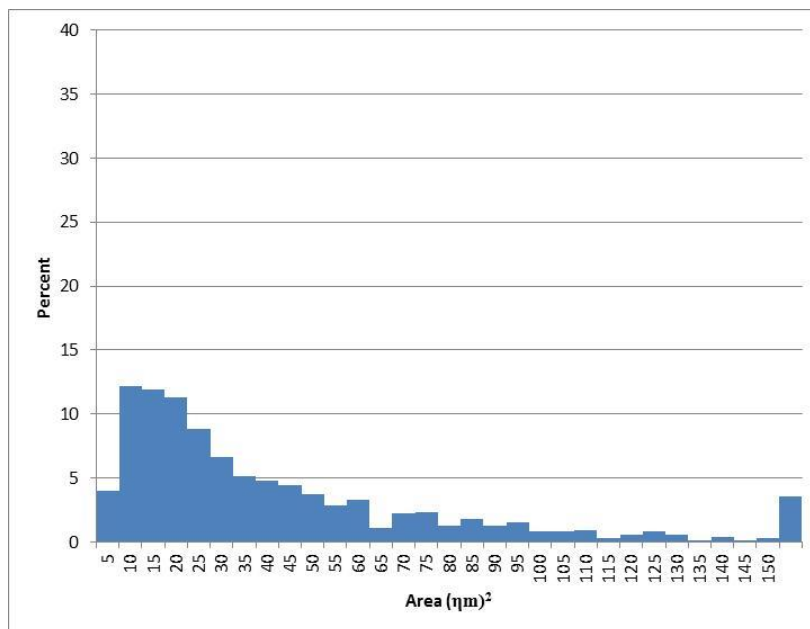
Figure 52: Area distribution of constituent particles for PGN sample heat treated with H1.
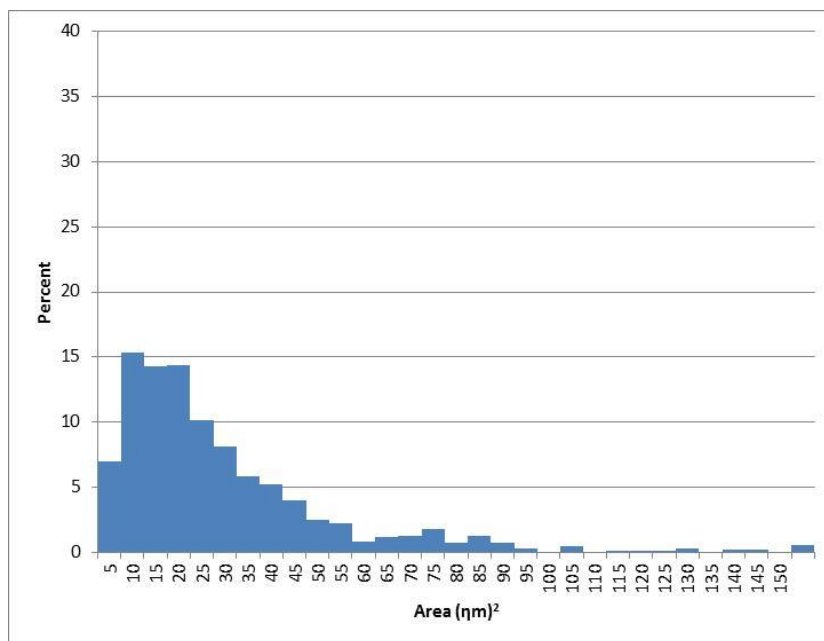
Figure 53: Area distribution of constituent particles for PGN sample heat treated with H3.

By comparing the area distributions for PGN alloy after heat treatment H3 and after PSC test in various conditions, it can be concluded that percentage of small constituent particles increase and percentage of the large particles decreases.

Aspect ratio defines as a ratio of the length over width of the constituent particles is shown in Figure 54. Shape factors of other hot deformation conditions are available in Appendix C. At low deformation temperature of the 300℃ the aspect ratio tends to higher values while at high deformation temperate of the 500℃ , it does not change significantly.
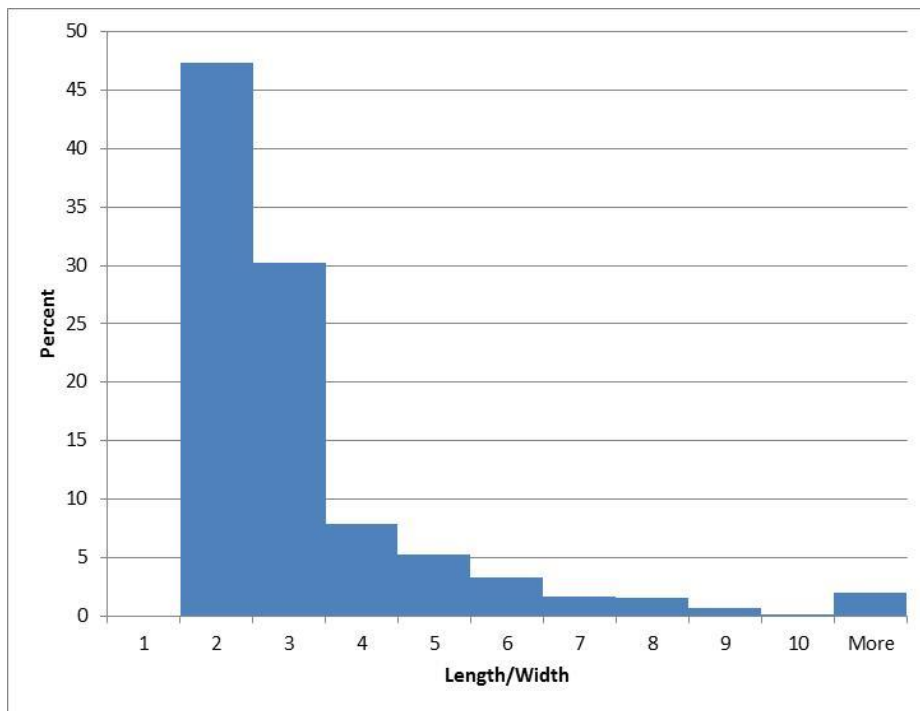
Figure 54: Aspect ratio for PGN alloy after homogenization H3

Chapter 6 Summary and Conclusions

In the current study the effect of Mn content and homogenization heat treatment on the hot deformation behavior of AA3XXX aluminum alloy was investigated. Three Mn contents of 0.05, 0.29 and 1.04 wt.% were considered and the alloys were designated as PGL, PGM, and PGN, respectively. These alloys were subjected to three different homogenization heat treatment cycles. In the single-step heat treatment (H1), the alloys were heated up to 500°C in 12 h and held for 8h followed by water quenching. In addition and in order to form more dispersoid particles compare to single-step heat treatment, two other two-steps heat treatments were also conducted. In the first one (H2), the alloys were heated up to 500°C in 12h, cooled down to 450°C in the furnace, held for 4h at that temperature followed by water quenching. In the second one (H3), the alloys were heated up to 600°C in 12h, then cooled down in furnace to 500°C and held for 2h, followed by water quenching.

Electrical conductivity measurements were applied on as-cast alloys and after three homogenization treatments. The lowest electrical conductivity of 29.98% IACS in case of the alloy with 1.04 wt% Mn showed the highest amount of Mn in solid solution. By decreasing the amount of Mn to 0.29 and 0.05 %wt, the electrical conductivity increased to 45.30, and 55.46 %IACS, respectively. The highest difference in electrical conductivity between as-cast condition and homogenized samples was in case of alloy with 1.04% Mn showing the formation of more dispersoids by increase of the Mn content in the AA3XXX aluminum alloy.

Hot deformation of the alloys was conducted using Gleeble 3500 machine, under plane strain conditions up to a final strain of 0.5. The deformation strain rate was selected as 0.1, 1.0 and 10 s^{-1}, and deformation temperature was ranged between 300-500°C with 100°C

temperature steps. Using the flow curves obtained from the Gleeble tests, the constitutive behavior of the materials was developed. Fitting parameters of the Sellars-Tegart model were calculated for PGM and PGN alloys. The highest deviation of about 10% was found between the prediction flow stress value of the model and flow stress obtained from the PSC (plain strain compression) test for samples with strain rate of 0.1 and temperature of 500 ℃. In addition, dislocation density and stored energy after hot deformation of AA3XXX aluminum alloys were calculated. Increasing of the Mn content of the alloy, decreasing hot deformation temperature, and increasing deformation strain rate led to formation of higher dislocation density and higher stored energy. The highest stored energy of 0.95 MJm^{-3} was calculated for the alloy for 1.04 wt% Mn, homogenized with heat treatment H1, deformed at temperature of 300°C and strain rate of 10 up to the strain of 0.5. Despite this high stored energy, due to existence of lots of dispersoids and back driving force due to Zener pinning effect, no static recrystallization after hot deformation is observed in an alloy with 1.04 wt% Mn content samples. In low Mn content alloy of PGL, 0.05 %wt, back driving force due to existence of dispersoids are not large enough to compensate the driving force in extreme cases of low deformation temperature and high strain rate. Consequently, existence of static recrystallization was confirmed in the microstructure after annealing in PGL alloy.

The deformed materials were characterized using optical microscopy and image analyzing software to measure as-cast area fraction of the constituent particles and the size and aspect ratio of the constituent particles before and after hot deformation. Increasing of the Mn content in AA3xxx aluminum alloys led to formation of the more constituent particles after casting. Area fraction of the constituent particles was measured 4.75, 7.64, and 11.14% for PGL, PGM and PGN alloy, respectively. In PGN alloy, the number of constituent

particles is much more in case of homogenized sample in H3 than H1. Hot deformation did not change the number of constituent particles significantly in case of PGN alloys samples homogenized with H3 heat treatment. At low deformation temperature of the 300℃ the aspect ratio, a ratio of the length over width of the constituent particles, tends to higher values while at high deformation temperate of the 500℃ , it does not change significantly.

Recovery model is able to capture the softening behavior of the Al-1%Mn alloy that has a close chemical composition to PGL alloy. A basic quantitative model of recovery was developed. Activation energy of 142 KJ/mole and activation volume of 22 b^3 showed a good fit to recovery model while b is the Burger's vector.

Conclusions from this research work can be listed below:

- Increasing Mn content in AA3XXX aluminum alloys leads the increasing of the hot flow strength

- Changing a homogenization heat treatment from H1,to H2 or H3, leads the decrease of the hot flow stress

- Constituent particles fracture depends strongly on the homogenization heat treatment. In case of the homogenization heat treatment H3, particle fragmentation is much more than the case of H1.

- Higher Mn content for PGN alloy forms more dispersoids after homogenization heat treatments. As a result, No statistic recrystallization is observed in any annealing treatment after PSC samples for PGN alloy with 1.04 wt% Mn.

- Existence of lower Mn content in PGL alloy combined with lower dispersoids formation in homogenization heat treatment of H1 compared to other heat

treatments leads the formation of static recrystallized grains after annealing heat treatment.

For future work, the microstructure modeling is suggested to be done by implementing physically based state variable microstructure models to simulate dynamic and static microstructure evolution during hot deformation and to predict the final microstructure parameters such as grain size and fraction recrystallized.

By obtaining the information regarding the dispersoids volume fraction and size from TEM image analyzing during homogenization treatment and subsequent hot deformation, the final goal would be to model the coupling between precipitation, recovery and recrystallization during hot extrusion of AA3xxx aluminum alloys. Such a model has been proposed by Vatne et al. or Zurob et. al. for modeling of recrystallization kinetics in micro-alloyed austenitic steels [53]. Application of the model or sensitivity analysis to understand role Mn on hot deformation and recrystallization is final goal [25].

References

[1]   D. G.Altenpohl, Aluminum: Technology, Applications and Environment, The aluminum association and the minerals, metals & materials society, 1998.

[2]   Iris De Graeve,Jürgen Hirsch, "Alumatter," 1 2 2013. [Online]. Available: http://aluminium.matter.org.uk/content/html/eng/default.asp?catid=214&pageid=21 44417044.

[3]   Y.J. Li, L. Arnberg, "Quantitative study on the precipitation behaviour of dispersoids in DC cast AA3003 alloy during heating and homogenization", *Acta Materialia 51 (2003) 3415-3428.*

[4]   H.R. Shercliff, M.F. Ashby, "A process model for age-hardening aluminium alloys: Part I:the model", *Acta Metall. Matter.38 (1990) 1789-1802.*

[5]   H.R. Shercliff ,M.F. Ashby, "A process model for age hardening of aluminium alloys—II. Applications of the model", *Acta Metall. Mater.38(10) (1990) 1803-1812.*

[6]   M.F. Ashby, "Physical modelling of materials problems", *Materials Science and Technology 8 (1992) 102-111.*

[7]   O. Richmond, "Microstructure-based modeling of deformation processes", *The Journal of The Minerals, Metals & Materials Society 38 (1986) 16-18.*

[8]   O. Grong, H. R. Shercliff, "Microstructural modelling in metals processing", *Progress in Materials Science 47 (2) (2002) 163-282.*

[9]   J. Hirsch, Virtual Fabrication of Aluminium products, Weinheim, Germany, 2006.

[10]   T.M. Pollock, Integrated computational materials engineering, National Academy of Engineering, 2008.

[11]   S.C. Weakley-Bollin, W. Donlon, C. Wolverton, J.W. Jones, and J.E. Allison, "Modeling the age-hardening behavior of Al-Si-Cu alloys", *Metallurgical and Materials Transactions A 35 (2004) 2407-2418.*

[12]   Integrated Computational Materials Engineering (ICME) - Unlocking the Potential and

Realizing the Vision: A Study on ICME Implementation, 2013: The Minerals, Metals and Materials Society.

[13] A.L. Dons, Y. Li, S. Benum, C.J. Simensen, A. Johansen ,E.K. Jensen, "Homogenisation of AA3103 and AA3003. PartI: the inistial structure of AA3003", *Aluminium 80 (2004) 583-587.*

[14] H.E. Vatne, O. Engle,and E. Nes, "Influence of particles on recrystallization textures and microstructre of aluminuim alloy 3103", *Material Science and Technology 13 (1997) 93-102.*

[15] Leslie, Iron and its dilute solid solutions, New York: Interscience, 1963.

[16] D.T.A Alexander, A.L Greer, "Solid-state intermetallic phase transformation in 3XXX aluminium alloys", *Acta materialia 50 (2002) 2571-2583.*

[17] R.G. Hamerton, H. Cama, M.W. Meredith, "Development of the coarse intermetallic particle population in wrought aluminium alloys during ingot casting and thermo-mechanical processing", *Materials Science Forum 331 (2000) 143-154.*

[18] A.L. Greer, D.T.L. Alexander , "Particle break up during heat treatment of 3000 series aluminuim alloy", *Material Science and Technology 21 (2005) 988-960.*

[19] N. Moulin , "Constituent particle break up during hot rolling of AA5182", *Advane Engineering Materials 12 (2012) 20-29.*

[20] H.W. Huang, B.L. Ou, "Evolution of precipitation during dofferent homogenization treatments in a 3003 aluminum alloy", *Materials and Design 30 (2009) 2685-2692.*

[21] J.P. Suni, R.T Shuey, R.D. Doherty, "dispersoid modeling in 3xxx Alloy", *Aluminum Alloys for Packaging (1996) 145-159.*

[22] H. Zhang, E.V. Konopleva , H.J. Mcqueen, "The strength of materials", *Material science and engineering 319 (2002) 711-715.*

[23] E. Nes, R. Orsund, "Recovery recrystallization ang grain growth", *Annealing Processes (1986) 475-480.*

[24] H.J. Mcqueen, S. Spigarelli, M. E. Kassner, E. Evangelista, Hot deformation and processing of Aliminium alloy, New York: CRC press, 2011.

[25] H.E. Vatne, T. Furu, R. Orsund, and E. Nes, "Modelling recrystallization after hot

deformation of aluminium", *Acta Materialia 44 (1966) 4463-4473.*

[26] J. Belling, H.J. McQueen, and A.S. Malin, "Static Recrystallization of Al-Mn-Mg alloys after ht torsion", *Intnl. Conf. Recrystallization in Metallic Materials (1990) 655-660.*

[27] G. Gottstein, Physical foundations of materials science, Heidelberg: Springer-Verlag Berlin Heiderberg, 2004.

[28] H.R. Shercliff, A.M. Lovatt, "Modelling of microstructure evolution in hot deformation", *Philosophical transactions of the royal society 357 (1999) 1621-1643.*

[29] H. R. Shercliff, A. M. Lovatt, "Modelling of microstructure evolution in hot deformation", *The Royal Society 357 (1999) 1621-1643.*

[30] C. M. Sellars, Q. Zhu, "Microstructural modelling of aluminium alloys during thermomechanical processing", *Materials Science and Engineering A280 (2000) 1-7.*

[31] R.J. McElroy, Z.C. Szkopiak, "Dislocation-substructure-strengthening and mechanical-thermal treatment of metals", *International Metallurgical Reviews 17 (1972) 175-202.*

[32] F.J. Humphreys, M. Hatherly, Recrystallization and related annealing phenomena, Pergamon, 1966.

[33] J.W.C. Dunlop, Y.J.M. Brechet, L. Legras, H.S. Zurob, "Modelling isothermal and non-isothermal recrystallisation kinetics: application to Zircaloy-4", *Journal of Nuclear Materials 366 (2007) 178-186.*

[34] MD.K. Rehman, H.S. Zurob, "A novel approach to model static recrystallization f austenite during hot rolling of Nb microalloyed steel. Part1:precipitation-free case", *Metallurgical and Materials Transactions 44A (2013) 1862-1871.*

[35] MD.K. Rehman, H.S. Zurob, "Novel approach to model static recrystallization of austenite during hot-rolling of Nb microalloyed steel: effect of precipitates", *Material Science Forum 753 (2013) 417-422.*

[36] O. Engler, L. Loechte, J. Hirsch, "Through-process simulation of texture and properties during the thermomechanical processing of aluminuim sheets", *Science Direct 55*

(2007) 5449-5463.

[37] A. R. Eivani, J. Zhou, J. Duszczyk, "A new approach to incorporating the effect of nano-sized dispersoids on recrystallization inhibition into Monte Carlo simulation", *Computational Material Science 54 (2012) 370-377.*

[38] A. Jenab, A. Karimi Taheri, and K. Jenab, "The use of ANN to predict the hotdeformation behavior of AA7075 at low strain rates", *Materials Engineering and Performance 22 (2013) 903-910.*

[39] F. Liu, D.B. Shan, Y. Lu,Y.Y. Yang, "Artificial neural network model of constitutive relationship for 2A70 aluminum alloy", *Acta Metallurgica Sinica 18 (2005) 719-723.*

[40] M. Verdier, Y. Brechet, P. Guyot, "Recovery of AlMg alloys: flow stress and strain-hardening properties", *Acta Materialia 47 (1999) 127-134.*

[41] A. Lens, C. Maurice, J. H. Driver, "Grain boundry mobility during recrystallization of Al-Mn alloys as measired by in situ annealing experiments", *Materials Science and Engineering 403 (2005) 144-153.*

[42] A. Lens, C. Maurice,J.H. Driver, "Grain boundry mobilities during recrystallization of AL-Mn alloys as measured by in situ annealing experiances", *Materials Science & Engineering 403 (2005) 144-153.*

[43] A.R. Eivani, "PhD thesis", Delft, The netherlands, 2010.

[44] E. Hersent, K. Huang, J. Friis and K. Marthinsen, "Modelling the evolution microchemistry and its effects on the softening behavior of cold rolled AlFeMnSi alloys during annealing", *Materials Science Forum 753 (2013) 143-146.*

[45] K. Marthinsen, J. Friis and O. Engler, "Modelling time dependent nucleation of recrystallization in alumium alloys", *Materials Science Forum 753 (2013) 147-152.*

[46] J. Zacharis , Microchemistry in aluminium sheet production, Delft, 2005.

[47] D.G. Altenpohl, Aluminuim: Technology, Application, and enviroment, Washengton: TMS, 1998.

[48] B. Raeisinia, W.J. Poole, D. J. Lioyd, "Examination of precipitation in the aluminium alloy AA6111 using electrical resistivity measurement", *Material Science*

Engineering 420 (2006) 245-249.

[49] P.L. Rossiter, The electrical resistivity of metals and alloys, Cambridge: Cambridge university press, 1987.

[50] K. Matsumoto, S. Komatsu, M. Ikeda, B. Verlinden,and P. Ratchev, "Quantification of volume fraction of precipitates in an aged al-1.0 mass% mg2si alloy", *Materials Transactions 41 (2000) 1275-1281.*

[51] C. Zheng, N. Xiao, D. Li, and Y. Li, "Microstructure prediction of the austenite recrystallization during multi-pass steel strip hot rolling: A cellular automaton modeling", *Computer Material Science 44 (2008) 507-514.*

[52] N. Rupa, "Effect de l'hydrogene et des hydrures sur le comportment viscoplastoque du Zircaloy-4 Recristallise", 2000.

[53] Zurob, H. S.; Hutchinson, C. R.; Brechet, Y.; Purdy, G., "Modeling recrystallization of microalloyed austenite: effect of coupling recovery, precipitation and recrystallization", *Acta Materialia 50 (2002) 3075-3092.*

[54] T.Sheppard, X. Duan, "Modelling of static recrystallisation by the combination of empirical models with the finite element method", *Journal of Materials Science 38 (2003) 1747-1754.*

[55] H.S. Zurob, C.R. Hutchinson, Y. Brechet, G. Purdy, "Modeling recrystallization of microalloyed austenite: effect of coupling recovery, precipitation and recrystallization", *Acta Materialia 50 (2002) 3075-3092.*

[1] D. G.Altenpohl, Aluminum: Technology, Applications and Environment, The aluminum association and the minerals, metals & materials society, 1998.

[2] Iris De Graeve,Jürgen Hirsch, "Alumatter," 1 2 2013. [Online]. Available: http://aluminium.matter.org.uk/content/html/eng/default.asp?catid=214&pageid=2144417044.

[3] Y.J. Li, L. Arnberg, "Quantitative study on the precipitation behaviour of dispersoids in DC cast AA3003 alloy during heating and homogenization," *Acta Materialia 51 (2003) 3415-3428.*

[4] H.R. Shercliff, M.F. Ashby, "A process model for age-hardening aluminium alloys:

Part I:the model," *Acta Metall. Matter.38 (1990) 1789-1802.*

[5] H.R. Shercliff ,M.F. Ashby, "A process model for age hardening of aluminium alloys—II. Applications of the model," *Acta Metall. Mater.38(10) (1990) 1803-1812.*

[6] M.F. Ashby, "Physical modelling of materials problems," *Materials Science and Technology 8 (1992) 102-111.*

[7] O. Richmond, "Microstructure-based modeling of deformation processes," *The Journal of The Minerals, Metals & Materials Society 38 (1986) 16-18.*

[8] O. Grong, H. R. Schercliff, "Microstructural modelling in metals processing," *Progress in Materials Science 47 (2) (2002) 163-282.*

[9] J. Hirsch, Virtual Fabrication of Aluminium products, Weinheim, Germany, 2006.

[10] T.M. Pollock, Integrated computational materials engineering, National Academy of Engineering, 2008.

[11] S.C. Weakley-Bollin, W. Donlon, C. Wolverton, J.W. Jones, and J.E. Allison, "Modeling the age-hardening behavior of Al-Si-Cu alloys," *Metallurgical and Materials Transactions A 35 (2004) 2407-2418.*

[12] Integrated Computational Materials Engineering (ICME) - Unlocking the Potential and Realizing the Vision: A Study on ICME Implementation, 2013: The Minerals, Metals and Materials Society.

[13] A.L. Dons, Y. Li, S. Benum, C.J. Simensen, A. Johansen ,E.K. Jensen, "Homogenisation of AA3103 and AA3003. PartI: the inistial structure of AA3003," *Aluminium 80 (2004) 583-587.*

[14] H.E. Vatne, O. Engle,and E. Nes, "Influence of particles on recrystallization textures and microstructre of aluminuim alloy 3103," *Material Science and Technology 13 (1997) 93-102.*

[15] Leslie, Iron and its dilute solid solutions, New York: Interscience, 1963.

[16] D.T.A Alexander, A.L Greer, "Solid-state intermetallic phase transformation in 3XXX aluminium alloys," *Acta materialia 50 (2002) 2571-2583.*

[17] R.G. Hamerton, H. Cama, M.W. Meredith, "Development of the coarse intermetallic

particle population in wrought aluminium alloys during ingot casting and thermo-mechanical processing," *Materials Science Forum 331 (2000) 143-154.*

[18] A.L. Greer, D.T.L. Alexander , "Particle break up during heat treatment of 3000 series aluminuim alloy," *Material Science and Technology 21 (2005) 988-960.*

[19] N. Moulin , "Constituent particle break up during hot rolling of AA5182," *Advane Engineering Materials 12 (2012) 20-29.*

[20] H.W. Huang, B.L. Ou, "Evolution of precipitation during dofferent homogenization treatments in a 3003 aluminum alloy," *Materials and Design 30 (2009) 2685-2692.*

[21] J.P. Suni, R.T Shuey, R.D. Doherty, "dispersoid modeling in 3xxx Alloy," *Aluminum Alloys for Packaging (1996) 145-159.*

[22] H. Zhang, E.V. Konopleva , H.J. Mcqueen, "The strength of materials," *Material science and engineering 319 (2002) 711-715.*

[23] E. Nes, R. Orsund, "Recovery recrystallization ang grain growth," *Annealing Processes (1986) 475-480.*

[24] H.J. Mcqueen, S. Spigarelli, M. E. Kassner, E. Evangelista, Hot deformation and processing of Aliminium alloy, New York: CRC press, 2011.

[25] H.E. Vatne, T. Furu, R. Orsund, and E. Nes, "Modelling recrystallization after hot deformation of aluminium," *Acta Materialia 44 (1966) 4463-4473.*

[26] J. Belling, H.J. McQueen, and A.S. Malin, "Static Recrystallization of Al-Mn-Mg alloys after ht torsion," *Intnl. Conf. Recrystallization in Metallic Materials (1990) 655-660.*

[27] G. Gottstein, Physical foundations of materials science, Heidelberg: Springer-Verlag Berlin Heiderberg, 2004.

[28] H.R. Shercliff, A.M. Lovatt, "Modelling of microstructure evolution in hot deformation," *Philosophical transactions of the royal society 357 (1999) 1621-1643.*

[29] H. R. Shercliff, A. M. Lovatt, "Modelling of microstructure evolution in hot deformation," *The Royal Society 357 (1999) 1621-1643.*

[30] C. M. Sellars, Q. Zhu, "Microstructural modelling of aluminium alloys during thermomechanical processing," *Materials Science and Engineering A280 (2000) 1-*

7.

[31] R.J. McElroy, Z.C. Szkopiak, "Dislocation-substructure-strengthening and mechanical-thermal treatment of metals," *International Metallurgical Reviews 17 (1972) 175-202.*

[32] F.J. Humphreys, M. Hatherly, Recrystallization and related annealing phenomena, Pergamon, 1966.

[33] J.W.C. Dunlop, Y.J.M. Brechet, L. Legras, H.S. Zurob, "Modelling isothermal and non-isothermal recrystallisation kinetics: application to Zircaloy-4," *Journal of Nuclear Materials 366 (2007) 178-186.*

[34] MD.K. Rehman, H.S. Zurob, "A novel approach to model static recrystallization f austenite during hot rolling of Nb microalloyed steel. Part1:precipitation-free case," *Metallurgical and Materials Transactions 44A (2013) 1862-1871.*

[35] MD.K. Rehman, H.S. Zurob, "Novel approach to model static recrystallization of austenite during hot-rolling of Nb microalloyed steel: effect of precipitates," *Material Science Forum 753 (2013) 417-422.*

[36] O. Engler, L. Loechte, J. Hirsch, "Through-process simulation of texture and properties during the thermomechanical processing of aluminuim sheets," *Science Direct 55 (2007) 5449-5463.*

[37] A. R. Eivani, J. Zhou, J. Duszczyk, "A new approach to incorporating the effect of nano-sized dispersoids on recrystallization inhibition into Monte Carlo simulation," *Computational Material Science 54 (2012) 370-377.*

[38] A. Jenab, A. Karimi Taheri, and K. Jenab, "The use of ANN to predict the hotdeformation behavior of AA7075 at low strain rates," *Materials Engineering and Performance 22 (2013) 903-910.*

[39] F. Liu, D.B. Shan, Y. Lu,Y.Y. Yang, "Artificial neural network model of constitutive relationship for 2A70 aluminum alloy," *Acta Metallurgica Sinica 18 (2005) 719-723.*

[40] M. Verdier, Y. Brechet, P. Guyot, "Recovery of AlMg alloys: flow stress and strain-hardening properties," *Acta Materialia 47 (1999) 127-134.*

[41]   A. Lens, C. Maurice, J. H. Driver, "Grain boundry mobility during recrystallization of Al-Mn alloys as measired by in situ annealing experiments," *Materials Science and Engineering 403 (2005) 144-153.*

[42]   A. Lens, C. Maurice,J.H. Driver, "Grain boundry mobilies during recrystallization of AL-Mn alloys as measured by in situ annealing experiances," *Materials Science & Engineering 403 (2005) 144-153.*

[43]   A.R. Eivani, "PhD thesis," Delft, The netherlands, 2010.

[44]   E. Hersent, K. Huang, J. Friis and K. Marthinsen, "Modelling the evolution microchemistry and its effects on the softening behavior of cold rolled AlFeMnSi alloys during annealing," *Materials Science Forum 753 (2013) 143-146.*

[45]   K. Marthinsen, J. Friis and O. Engler, "Modelling time dependent nucleation of recrystallization in alumium alloys," *Materials Science Forum 753 (2013) 147-152.*

[46]   J. Zacharis , Microchemistry in aluminium sheet production, Delft, 2005.

[47]   D.G. Altenpohl, Aluminuim: Technology, Application, and enviroment, Washengton: TMS, 1998.

[48]   B. Raeisinia, W.J. Poole, D. J. Lioyd, "Examination of precipitation in the aluminium alloy AA6111 using electrical resistivity measurement," *Material Science Engineering 420 (2006) 245-249.*

[49]   P.L. Rossiter, The electrical resistivity of metals and alloys, Cambridge: Cambridge university press, 1987.

[50]   K. Matsumoto, S. Komatsu, M. Ikeda, B. Verlinden,and P. Ratchev, "Quantification of volume fraction of precipitates in an aged al-1.0 mass% mg2si alloy," *Materials Transactions 41 (2000) 1275-1281.*

[51]   C. Zheng, N. Xiao, D. Li, and Y. Li, "Microstructure prediction of the austenite recrystallization during multi-pass steel strip hot rolling: A cellular automaton modeling," *Computer Material Science 44 (2008) 507-514.*

[52]   N. Rupa, "Effect de l'hydrogene et des hydrures sur le comportment viscoplastoque du Zircaloy-4 Recristallise," 2000.

[53]   Zurob, H. S.; Hutchinson, C. R.; Brechet, Y.; Purdy, G., "Modeling recrystallization of

microalloyed austenite: effect of coupling recovery, precipitation and recrystallization," *Acta Materialia 50 (2002) 3075-3092.*

[54] T.Sheppard, X. Duan, "Modelling of static recrystallisation by the combination of empirical models with the finite element method," *Journal of Materials Science 38 (2003) 1747-1754.*

[55] H.S. Zurob, C.R. Hutchinson, Y. Brechet, G. Purdy, "Modeling recrystallization of microalloyed austenite: effect of coupling recovery, precipitation and recrystallization," *Acta Materialia 50 (2002) 3075-3092.*

Appendix A
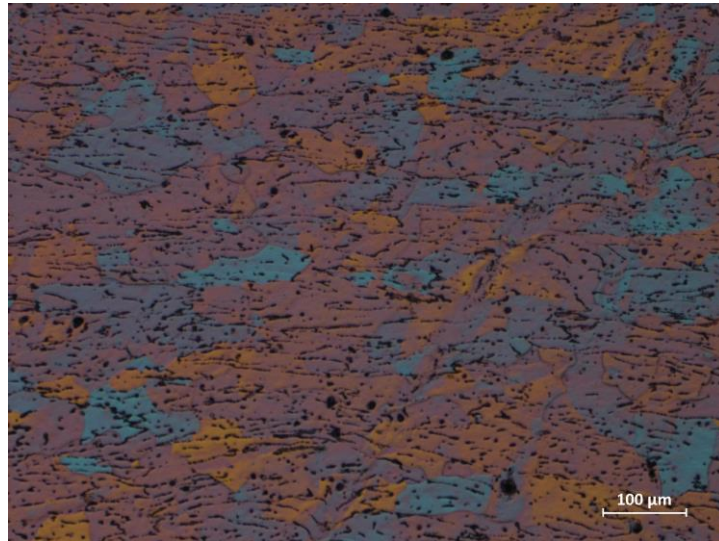
Figure 55: PSC sample grain structure for a PGL sample deformed at 300 ℃ and strain rate of 10 up to a strain of 0.5, heat treated with schedule H1 and annealed at 500 ℃ for 6 hours.
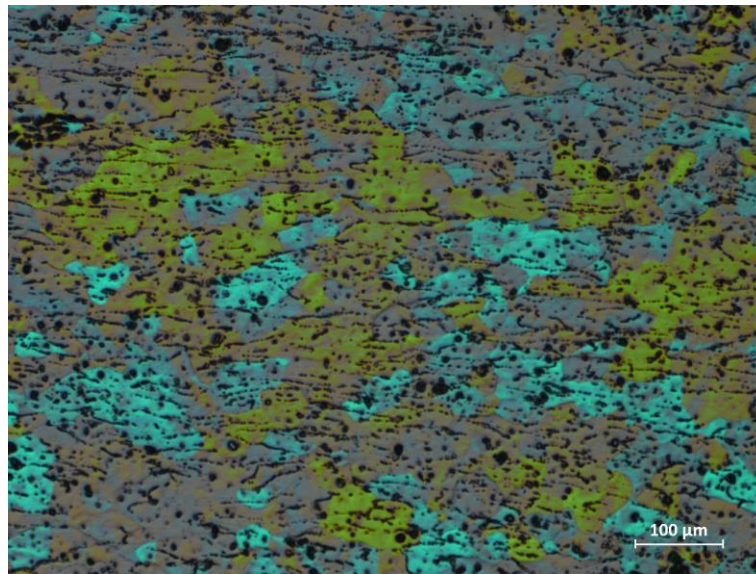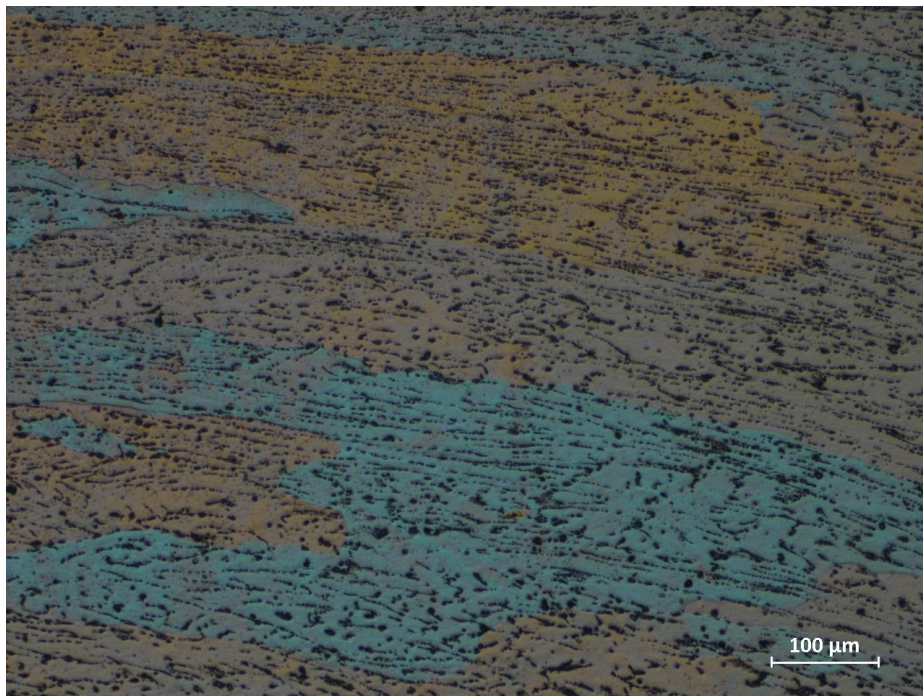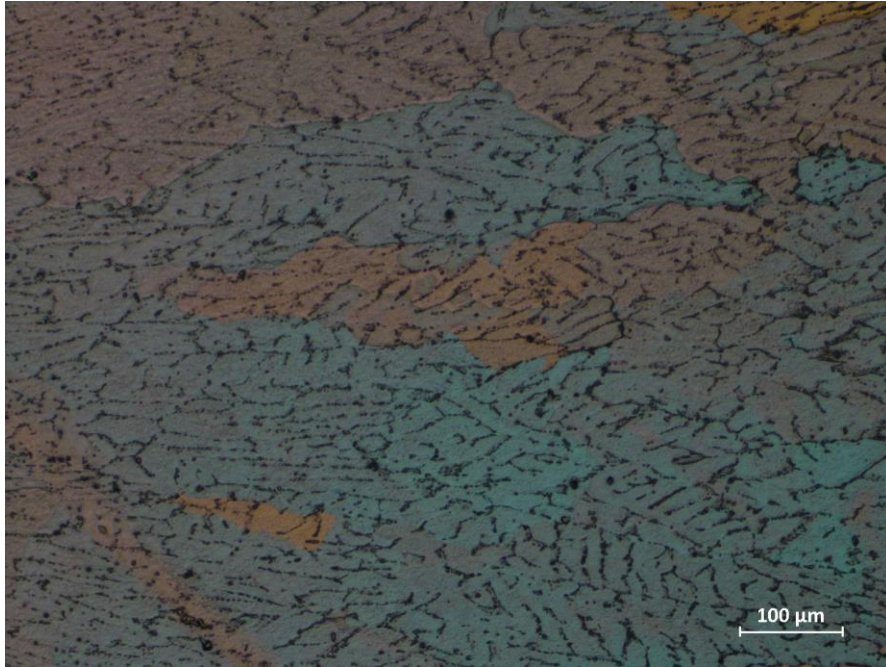

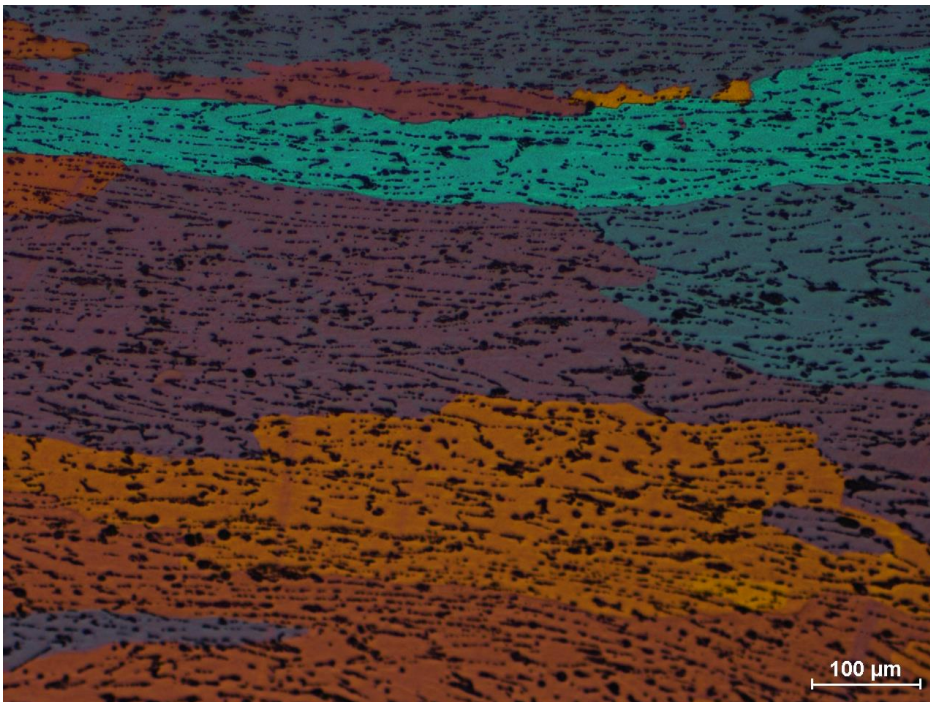
Figure 56: PSC sample grain structure for a PGL sample deformed at 300 ℃ and strain rate of 10 up to a strain of 0.5, heat treated with schedule H3 and annealed at 500 ℃ for 6 hours.
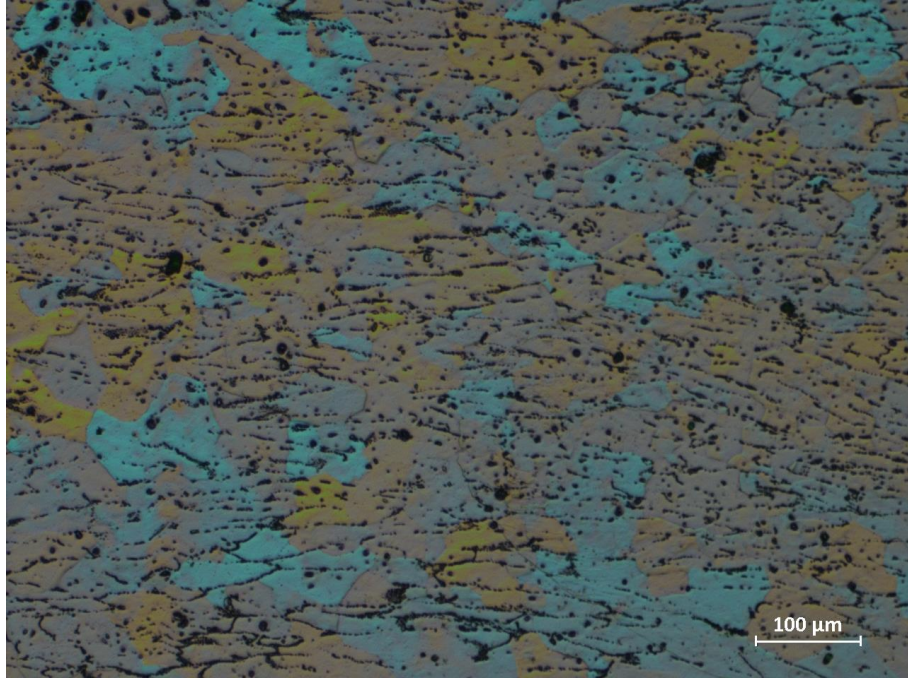
Figure 57: PSC sample grain structure for a PGL sample deformed at 300 ℃ and strain rate of 10 up to a strain of 0.5, heat treated with schedule H3 and annealed at 500 ℃ for 12 hours.
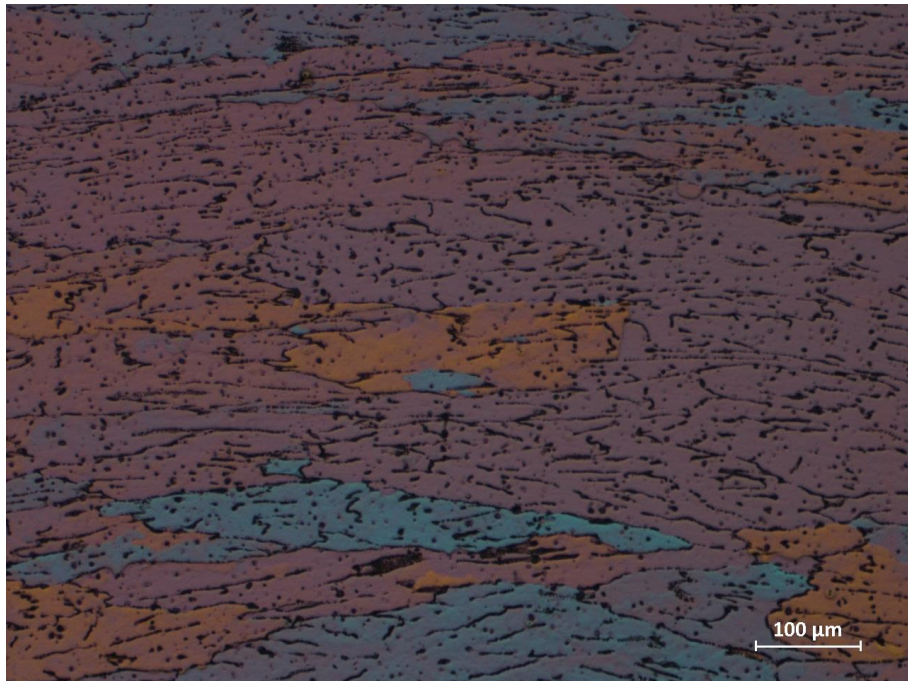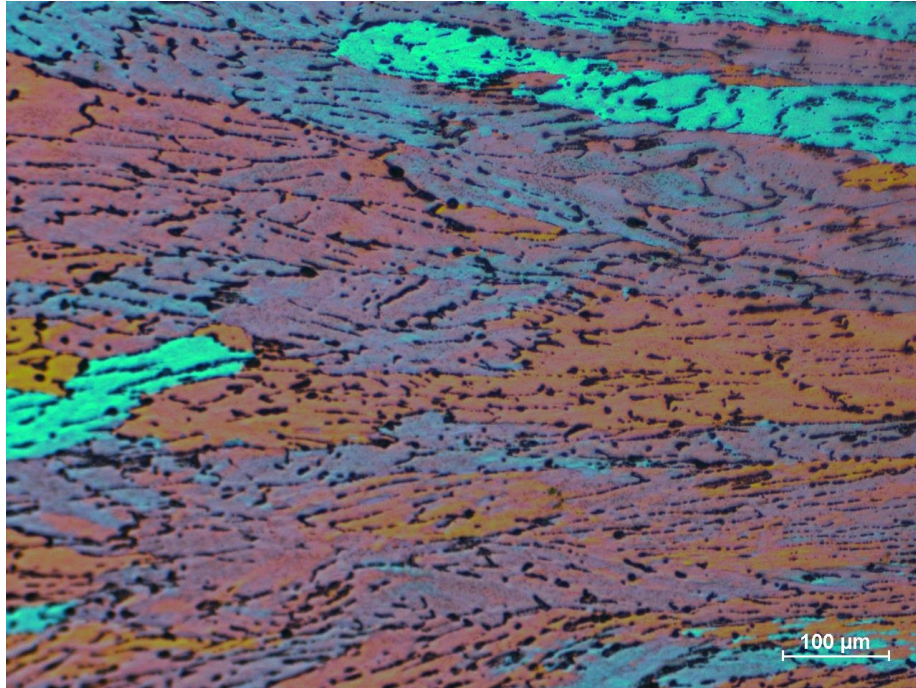

Figure 58: PSC sample grain structure for a PGL sample deformed at 500 ℃ and strain rate of 10 up to a strain of 0.5, heat treated with schedule H1 and annealed at 500 ℃ for 6 hours.
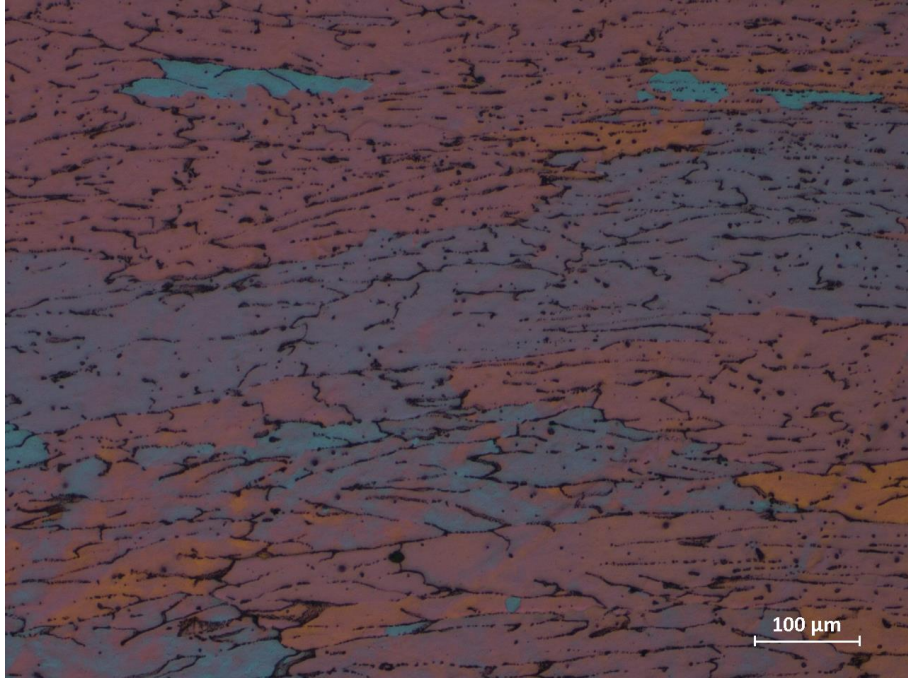
Figure 59: PSC sample grain structure for a PGL sample deformed at 500 ℃ and strain rate of 10 up to a strain of 0.5, heat treated with schedule H1 and annealed at 500 ℃ for 12 hours.
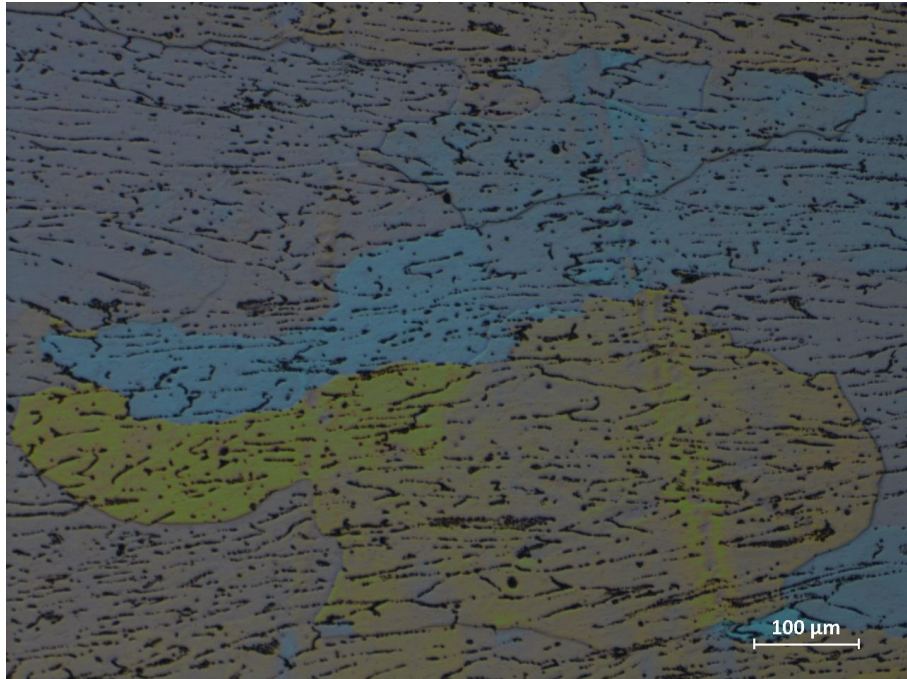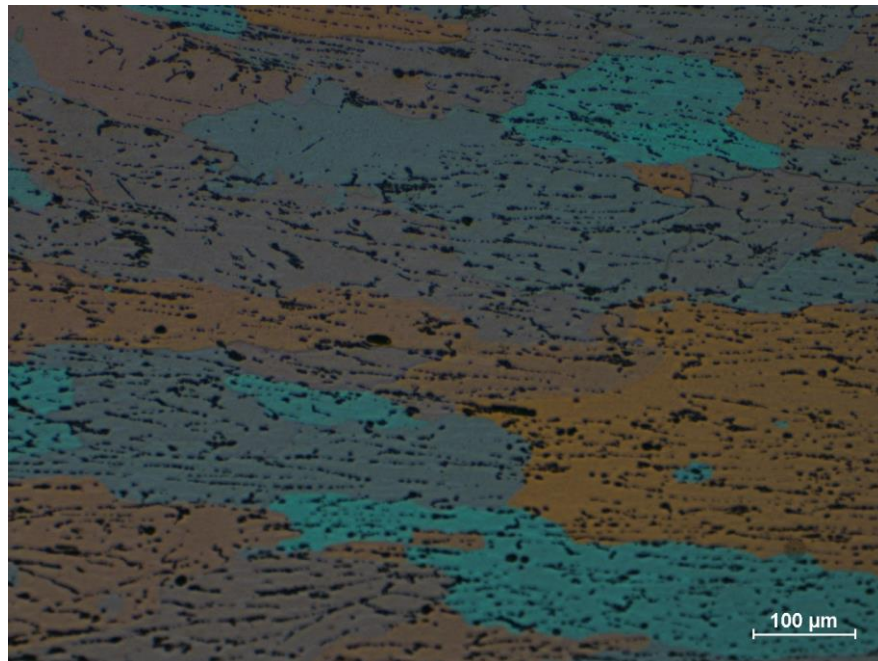

Figure 60: PSC sample grain structure for a PGL sample deformed at 500 ℃ and strain rate of 10 up to a strain of 0.5, heat treated with schedule H3 and annealed at 500 ℃ for 6 hours.
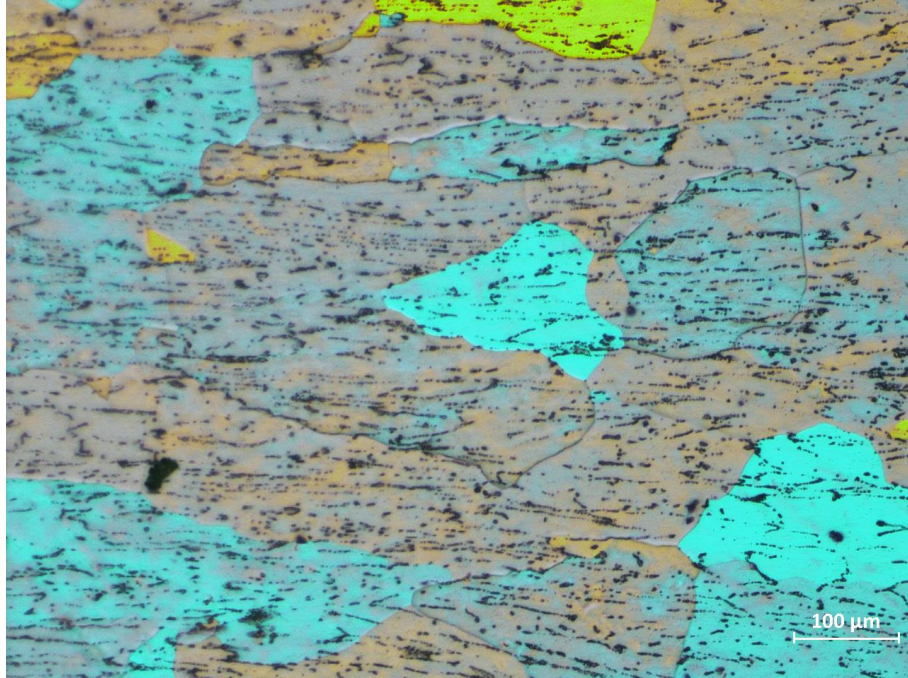
Figure 61: PSC sample grain structure for a PGL sample deformed at 500 ℃ and strain rate of 10 up to a strain of 0.5, heat treated with schedule H3 and annealed at 500 ℃ for 12 hours.
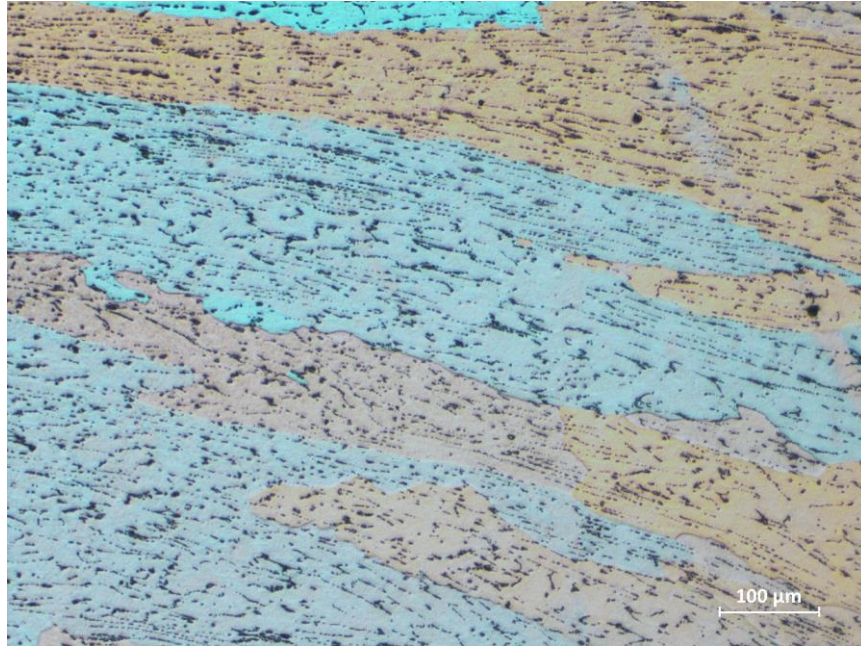
Figure 62: PSC sample grain structure for a PGN sample deformed at 300 ℃ and strain rate of 10 up to a strain of 0.5 heat treated with schedule H1 and annealed at 550 ℃ for 2 hours.
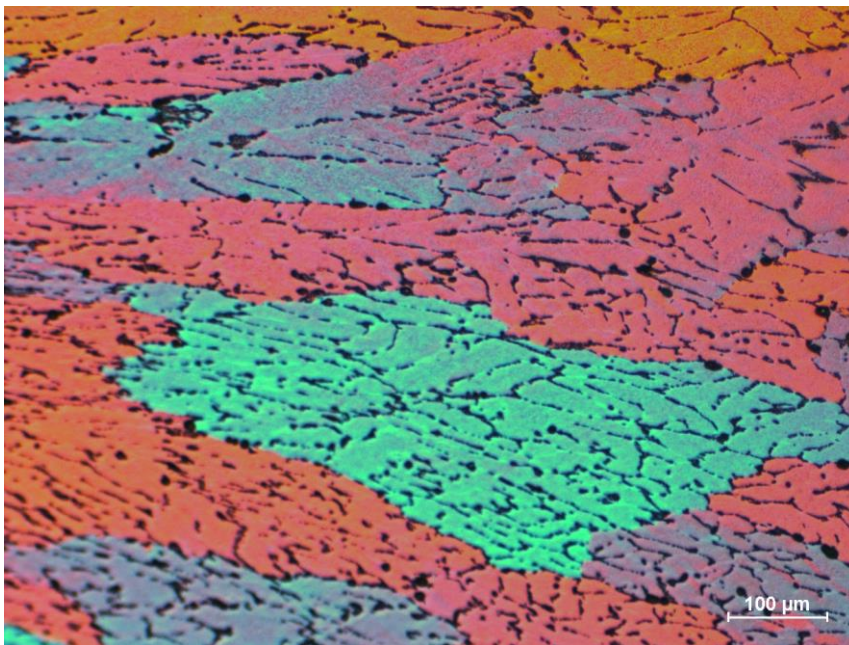

Figure 63: PSC sample grain structure for a PGN sample deformed at 300 ℃ and strain rate of 10 up to a strain of 0.5, heat treated with schedule H1 and annealed at 550 ℃ for 6 hours.
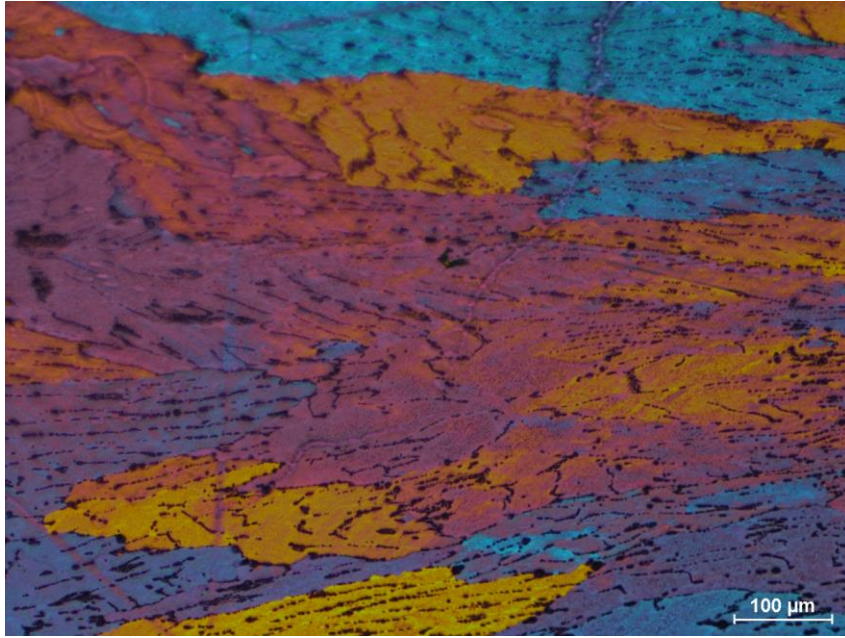
Figure 64: PSC sample grain structure for a PGN sample deformed at 300 ℃ and strain rate of 10 up to a strain of 0.5, heat treated with schedule H3 and annealed at 550 ℃ for 2 hours.

Figure 65: PSC sample grain structure for a PGN sample deformed at 300 ℃ and strain rate of 10 up to a strain of 0.5, heat treated with schedule H1 and annealed at 500 ℃ for 12 hours.

Figure 66: PSC sample grain structure for a PGN sample deformed at 500 ℃ and strain rate of 10 up to a strain of 0.5, heat treated with schedule H1 and annealed at 500 ℃ for 6 hours.

Figure 67: PSC sample grain structure for a PGN sample deformed at 300 ℃ and strain rate of 10 up to a strain of 0.5, heat treated with schedule H3 and annealed at 500 ℃ for 6 hours.

Figure 68: PSC sample grain structure for a PGN sample deformed at 300 ℃ and strain rate of 10 up to a strain of 0.5, heat treated with schedule H3 and annealed at 500 ℃ for 12 hours.

Figure 69: PSC sample grain structure for a PGN sample deformed at 500 ℃ and strain rate of 10 up to a strain of 0.5, heat treated with schedule H3 and annealed at 500 ℃ for 6 hours.

Figure 70: PSC sample grain structure for a PGN sample deformed at 500 ℃ and strain rate of 10 up to a strain of 0.5, heat treated with schedule H3 and annealed at 500 ℃ for 12 hours.

Appendix B
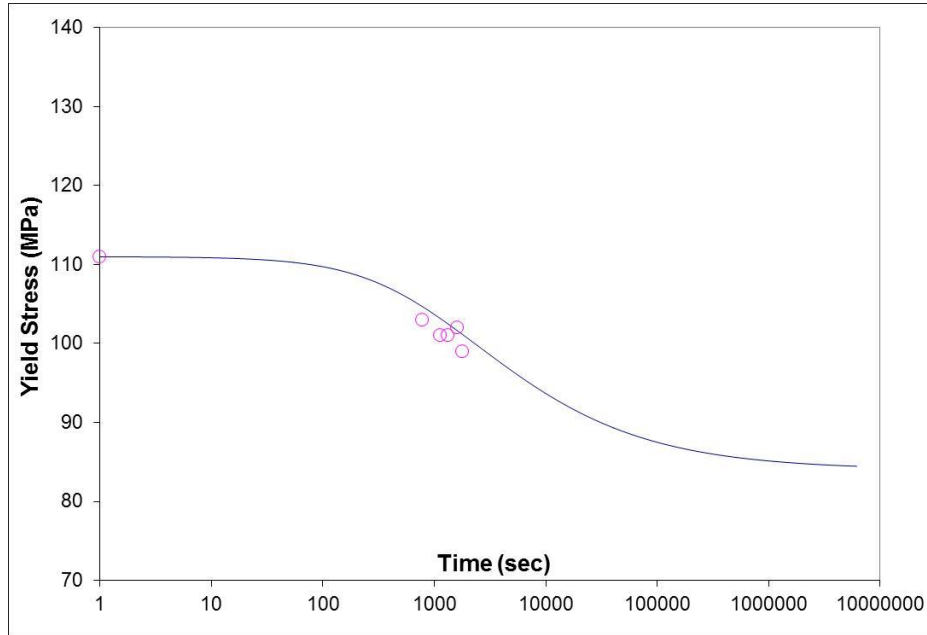
Figure 71: Comparison between experimental data and recovery model prediction for strain up to 1.3 and annealed at 260℃ for AL-1% Mn
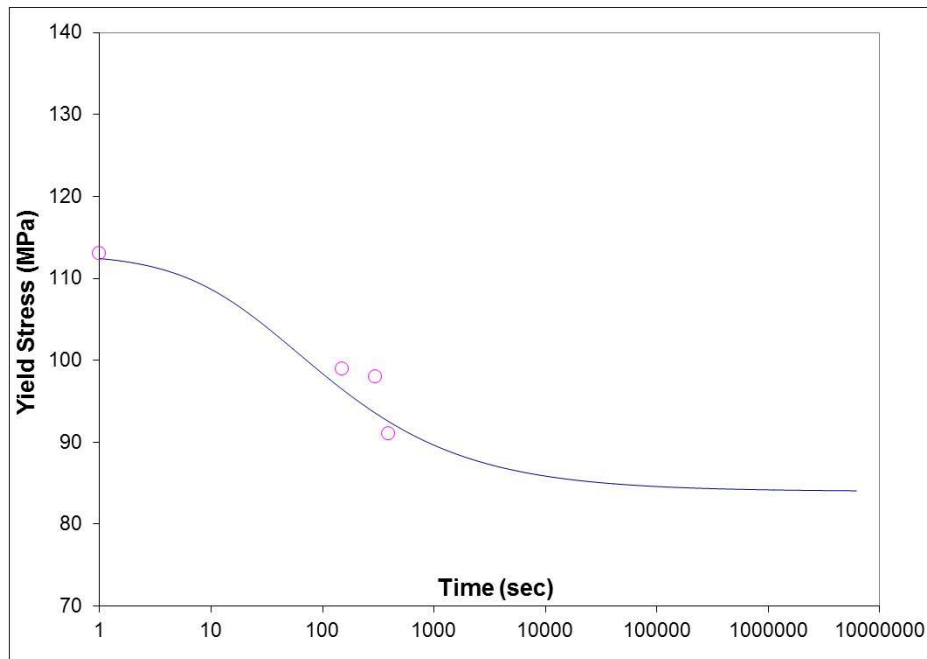
Figure 72: Comparison between experimental data and recovery model prediction for strain up to 1.3 and annealed at 330℃ for AL-1% Mn
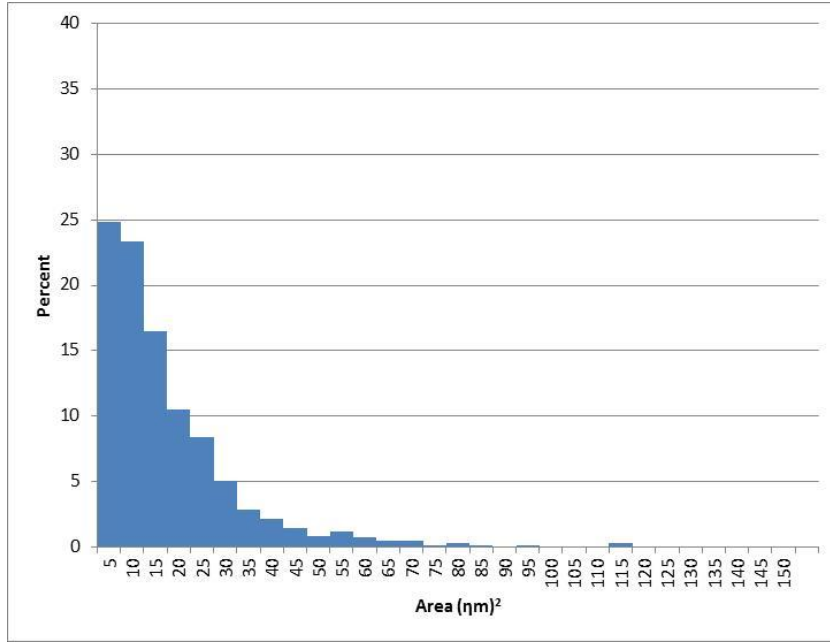
Appendix C
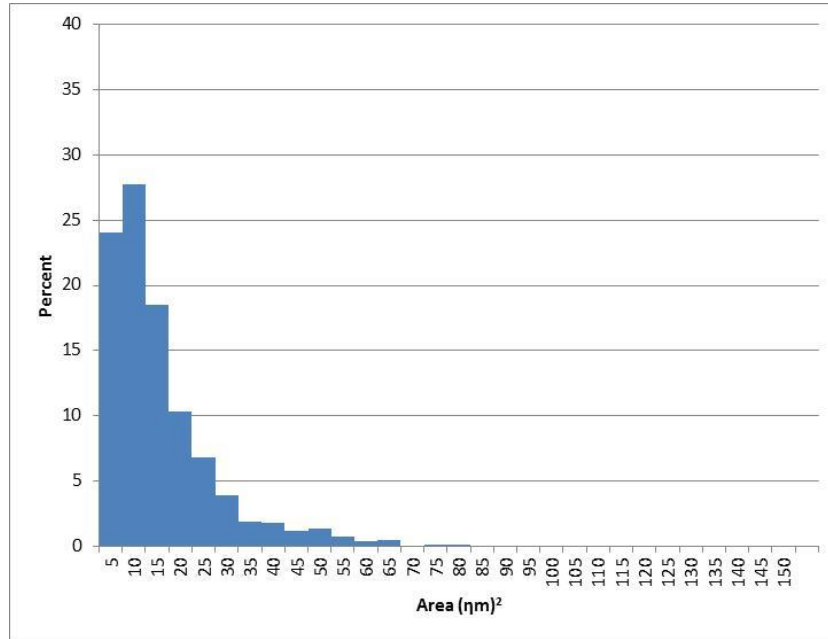
Figure 73: Area distribution of constituent particles for PGN alloy heat treated in H3 deformed at 300℃ up to strain 0.5 with strain rate of 0.1
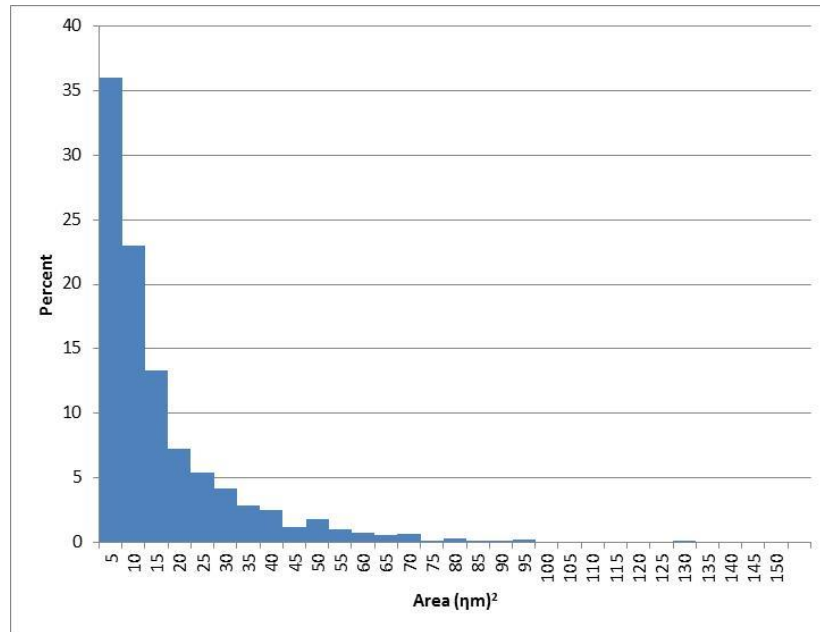
Figure 74: Area distribution of constituent particles for PHN alloy heat treated in H3 deformed at 300℃ up to strain 0.5 with strain rate of 10

Figure 75: Area distribution of constituent particles for PHN alloy heat treated in H3 deformed at 500℃ up to strain 0.5 with strain rate of 0.1
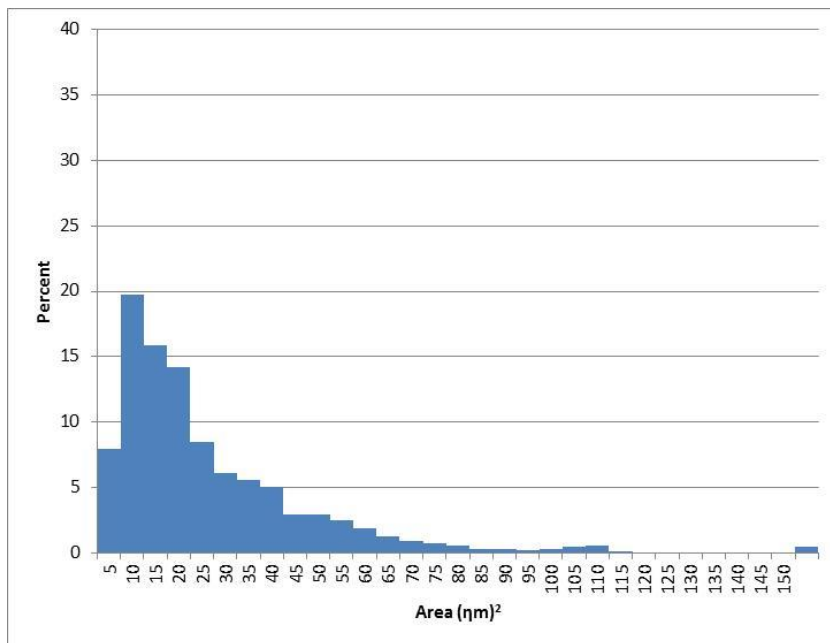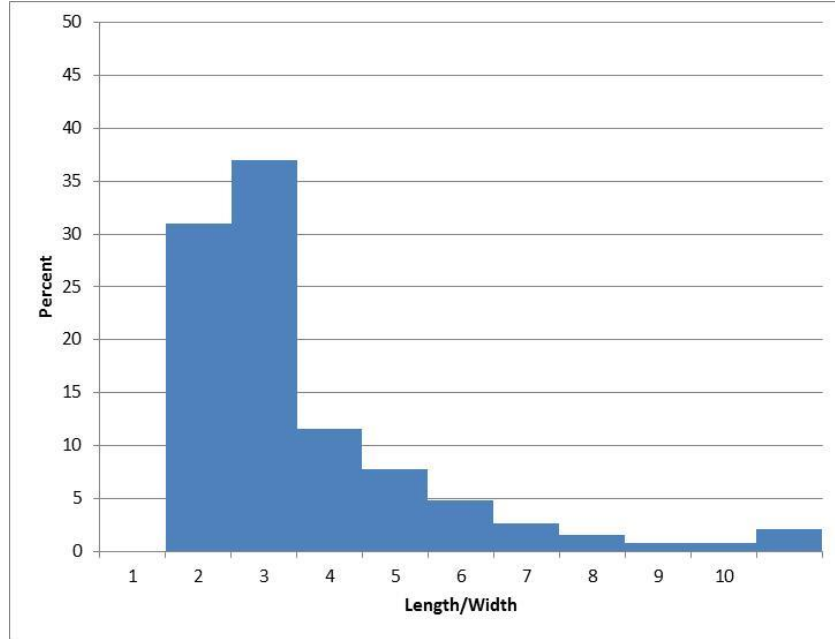

Figure 76: Area distribution of constituent particles for PHN alloy heat treated in H3 deformed at 500℃ up to strain 0.5 with strain rate of 10

Figure 77: Aspect ratio of constituent particles for PGN alloy heat treated with H3 deformed at 300 ℃ up to strain 0.5 with strain rate of 0.1
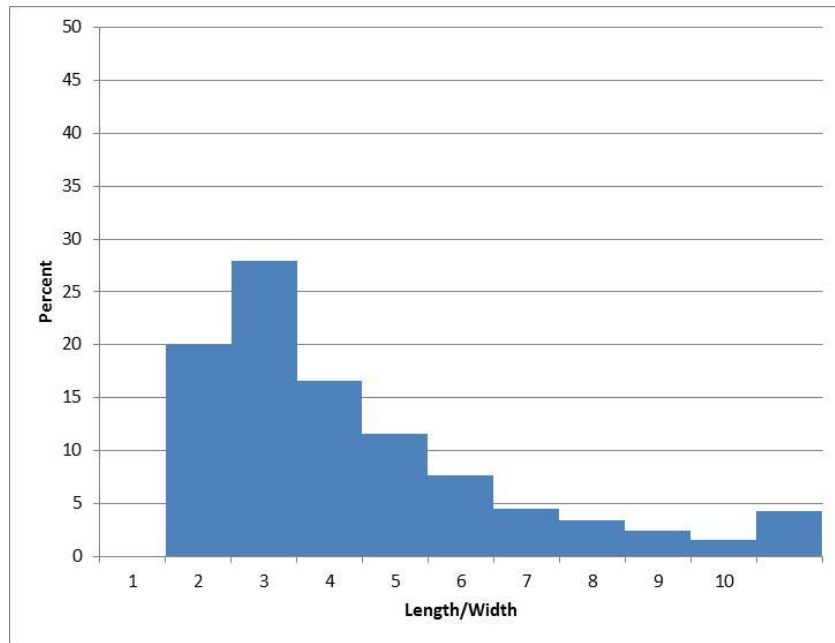

Figure 78: Aspect ratio of constituent particles for PGN alloy heat treated with H3 deformed at 300 ℃ up to strain 0.5 with strain rate of 10
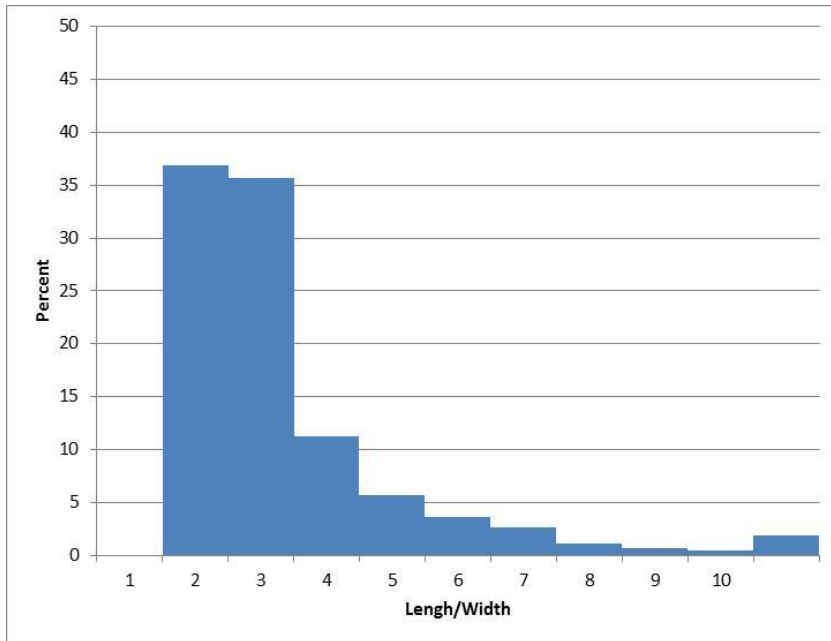
Figure 79: Aspect ratio of constituent particles for PGN alloy heat treated with H3 deformed at 500 ℃ up to strain 0.5 with strain rate of 0.1
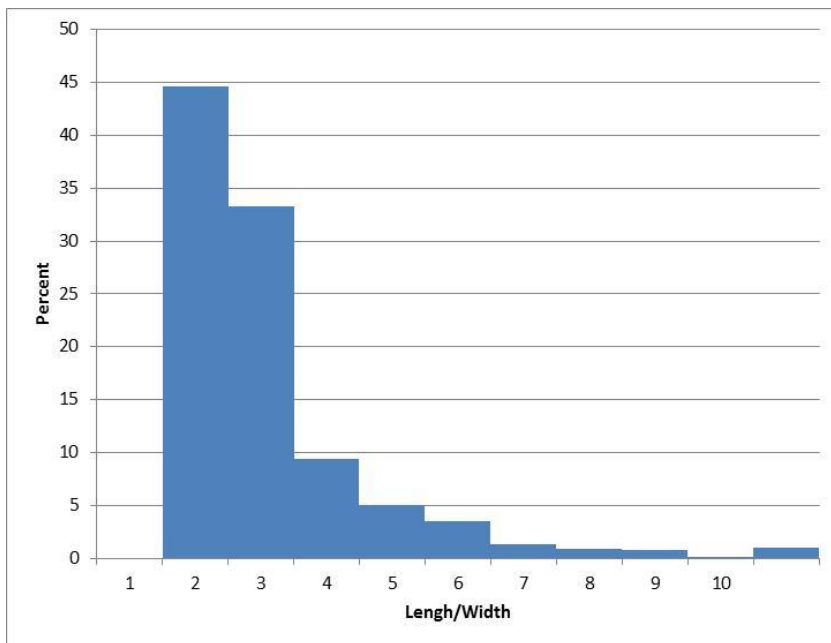

Figure 80: Aspect ratio of constituent particles for PGN alloy heat treated with H3 deformed at 500 ℃ up to strain 0.5 with strain rate of 10